Systèmes d'Imagerie Interferometriques

par

Èttoré Pédrétti

B.Sc. (University of Northumbria) 1997
M.Sc. (University of Manchester) 1999

Une thése présentée pour obtenir le titre de
Docteur en Sciences de l'Université de Provence

Spécialité
Rayonnement et Plasmas

UNIVERSITÉ de PROVENCE
Aix–Marseille I

Ecole Doctorale Physique et Sciences de la Matière

Soutenue à l'Observatoire de Haute-Provence
devant le jury composé de :

M. Farrokh Vakili, Président du Jury et Rapporteur
M. Christopher A. Haniff, Rapporteur
M. Antoine Labeyrie, Directeur de thèse
M. Wesley A. Traub, Directeur de thèse
M. Pierre Kern, Examinateur

17 Octobre 2003

Remerciements

Ces travaux de thèse ont été financés par le Collège de France pendant les deux premières années puis par la Smithsonian Institution pendant le temps restant, grâce à une bourse de thèse dans le cadre du programme “Smithsonian Predoctoral Fellowship”.

Je voudrais commencer par remercier mes enseignants à l’Université de Northumbria, Newcastle, en particulier M. Ben Rudden, pour ses leçons intéressantes sur la physique de l’état solide et pour m’avoir envoyé en France dans le cadre du programme d’échange d’étudiants Erasmus. Je remercie M. Alastair MacGregor, mon superviseur de projet de dernière année, pour ses conseils utiles pendant le démarrage de ma simulation d’interféromètres optiques. A l’Université de Marseille, Mme. Aline Huard m’a présenté à M. Antoine Labeyrie, mon directeur de thèse. Elle fut une très bonne tutrice pendant mon stage à l’Observatoire de Haute Provence.

Cela fut un grand privilège pour moi de travailler avec le Professeur Antoine Labeyrie dont la curiosité naturelle pour la science et le monde naturel sont une inspiration continue. Merci pour m’avoir laisser chevaucher Pulsar. Merci de m’avoir appris la beauté du vol-à-voile. Même si je n’ai pas encore obtenu mon brevet, je sais qu’un jour je serai finalement “laissé” sur une de ces machines merveilleuses.

Pendant mon séjour à l’Observatoire de Haute Provence, Anabela Gonçalvez et Stèphane Darbon, mes chers amis, rendaient la vie sur la montagne plus acceptable, avec de fréquentes sorties au cinéma et à la Crêperie de Forcalquier. Après leur départ l’observatoire n’était plus le même endroit. Merci à Marie-Josée et Alain Vin pour souvent inviter les étudiants (nous) à leur maison de Saint Michel l’ Observatoire et pour les belles ballades organisées sur les montagnes de Provence. (Merci aussi à Marie-Josée pour le bon café à la bibliothèque tous les matins). Merci beaucoup à Remedios, Nathalie, Anne-Marie, Brigitte et tous les filles de la Maison Jean-Perrin. Merci pour tous les bons repas végétariens préparés spécialement pour le premier résident végétarien de long terme. Merci à Luc Arnold pour écouter mes idées folles et pour beaucoup de bonnes suggestions sur l’interférométrie optique. Merci à Farrokh Vakili pour beaucoup de bonnes suggestions et pour nous traiter (moi et les autres étudiants) comme des collègues et amis.

Les personnes avec qui j’ai travaillé à IOTA me manqueront beaucoup. Merci à M. Nat Carleton. Son aide et conseils furent beaucoup appréciés au CFA et plus encore à la montagne où il est resté pour m’aider deux semaines. Entre autres choses il m’apprenait à m’arrêter au coucher du soleil pour contempler le spectacle. Les couchers de soleil en Arizona sont tous spectaculaires et uniques. Merci à Mike Pearlman pour son aide sur les questions financières et de voyages et pour ses bons conseils en général. L’aide de Marc Lacasse était inestimable pendant tous les mois passés à IOTA.

Rafael Millan-Gabet, John Monnier et Jean-Philippe Berger n'ont pas simplement été mes chers amis mais ils agissaient comme directeurs de thèse additionnels. Merci pour courir avec moi, pour les bons plats que nous mangions ensemble et pour les belle ballades au mont Wrightson et le jour de l'an passé ensemble à Cambridge. Merci beaucoup à Sam Ragland pour m'enregistrer des données à IOTA et pour les nuits d'aide pendant la recherche des franges à IOTA.

Je me sens très honoré d'avoir eu Wes Traub comme co-directeur de thèse au Smithsonian Astrophysical Observatory. J'ai vraiment aimé notre relation personnelle et professionnelle. Wes trouve toujours une explication simple pour des concepts très compliqués. Sans son encouragement je ne serais jamais arrivé à la fin de ce travail. Merci Wes.

Merci à Farrokh Vakili et Chris Haniff pour accepter d'être rapporteurs pour ma thèse. Merci aux autres membres du jury, Lise Deharveng et Pierre Kern pour accepter d'être les examinateurs.

Finalement merci à Nathalie pour son amour, support et aide pendant ces longues années, et malgré mes terribles humeurs. Je ne serais jamais arrivé à la fin de ce travail sans son encouragement et support.

Résumé

Je présente dans cette thèse la combinaison de travaux expérimentaux, observationnels, et d'analyse de données achevés en partie à l'Observatoire de Haute Provence (France) et en partie à Smithsonian Astrophysics Observatory (USA).
J'ai développé un algorithme de mise en phase adapté aux interféromètres. Il implique une hiérarchie de triplets d'ouvertures. Des simulations numériques appliquées au cas d'objets résolus et non-résolus montrent qu'une seule itération est généralement suffisante pour obtenir le co-phasage.
J'ai réalisé les premières images obtenues sur le ciel avec un interféromètre à pupille densifiée miniature. La formation de telles images viole la règle d'or des interféromètres imageurs qui semble interdire l'usage d'assemblages interférométriques différents d'un interféromètre de Fizeau.
J'ai développé pour IOTA de nouveaux contrôleurs pour la caméra proche infra-rouge PICNIC ainsi qu'un "suiveur d'étoiles". Le bruit de lecture de la caméra est maintenant réduit à 12.4 électrons par double échantillon corrélé.
J'ai conçu un suiveur de franges maintenant régulièrement utilisé pour égaliser les chemins optiques entre les trois bases d'IOTA. Ceci est achevé au moyen d'un nouvel algorithme basé sur l'interférométrie double Fourier, et sur un algorithme de suivi de retard de groupe pour déterminer la position du paquet de franges.
Une partie de mon travail a impliqué la réduction de données d'observations d'étoiles Mira. Nous avons obtenu les premières mesures simultanées des diamètres dans les bandes J, H et K par interférométrie longue base et détecté les variations des diamètres entre les différentes bandes spectrales.

Table des matières

Chapitre 1

Introduction

1.1 L'Importance de la Haute Résolution Angulaire en Astrophysique.

L'astrophysique est une science qui transforme le cosmos en un laboratoire géant où des phénomènes exotiques, non reproductibles sur Terre, peuvent être observés. Les limitations de cette science reposent sur des conditions expérimentales complètement hors du contrôle des observateurs. Observer des phénomènes naturels est très différent de réaliser une expérience dans l'environnement contrôlé d'un laboratoire, où température, pression, et densité sont des paramètres connus et sous contrôle. Ce n'est pas le cas en astrophysique où les expériences ont été mises en place il y a plusieurs milliards d'années lorsque l'expansion de l'univers commença.

La bonne nouvelle pour l'astrophysique observationnelle est qu'une incroyable quantité d'expériences, à tous les stades de développement possibles, se produisent dans l'univers à ce moment précis. L'observation de ces expériences naturelles permet aux astrophysiciens d'accéder à une description statistique de la structure de l'univers. La mauvaise nouvelle est que la plupart de ces phénomènes sont invisibles pour les observateurs. A l'exception de l'astrophysique des particules, où rayons cosmiques et neutrinos sont détectés par leur interaction avec des fluides, les principales observables en astrophysique sont les photons (lumière), lesquels voyagent pendant des années et parcourent d'énormes distances avant d'atteindre l'observateur. Ces photons portent la signature des phénomènes les ayant générés. Leur longueur d'onde (couleur) et distribution spatiale (image) peuvent apporter des informations sur la composition, la température et la densité de la matière à leur origine et sur les transformations physiques s'y produisant.

L'univers est très vaste. Beaucoup des phénomènes que nous souhaiterions observer se produisent très loin de nous. Cela peut rendre la dimension angulaire des objets observés très petite, leur dimension angulaire sur le ciel étant inversement proportionnelle à leur distance d. Par ailleurs, la quantité de photons collectée est inversement proportionnelle à d^2. Les objets les plus lointains peuvent être très faibles et les pho-

tons très peu nombreux. Les télescopes sont des entonnoirs à photons qui collectent la lumière en provenance des objets célestes. Le diamètre D des télescopes détermine la quantité de photons collectée, laquelle est proportionnelle à D^2. La sensibilité d'un télescope dépend de beaucoup d'autres facteurs tels que la réflectivité du revêtement du miroir, le nombre de réflexions dans son train optique, et l'efficacité quantique du détecteur utilisé.

Une plus grande ouverture, en plus d'améliorer la sensibilité d'un télescope, augmente le degré de détails (ou résolution angulaire) pouvant être détectés dans un objet. La résolution d'une image peut être quantifiée par le "pouvoir de résolution" de l'instrument lequel est déterminé par le rayon du premier minimum de la figure de diffraction, soit $1.22\lambda/D$, où λ est la longueur d'onde de la lumière à laquelle l'observation est réalisée ($\lambda = 550$ nm dans cet chapitre). Pour la classe actuelle de télescopes, D est égal à 8 m, produisant un pouvoir de résolution de $0.018''$. La construction de miroirs monolithiques de diamètres supérieurs à 8 m est extrêmement problématique, du fait, d'une part de leur masse qui cause des flexions de la monture du télescope et d'autre part de leur coût très élevé. Les solutions pour le moment envisagées, pour la construction de la prochaine génération d'instruments astronomiques, est la construction de miroirs segmentés. Cette technologie a été utilisée avec succès pour la construction des télescopes de 10m du Keck, lesquels atteignent une résolution angulaire de $0.014''$.

Cependant, pour les observations astronomiques menées depuis le sol, le facteur limitant n'est pas la diffraction, mais la turbulence atmosphérique. Le front d'onde incident est corrompu pas la turbulence, rendant l'image d'une source ponctuelle (fonction de transfert optique) floue et beaucoup plus étendue qu'une image limitée par la diffraction. Le "flou" de la fonction de transfert optique (FTO) a été quantifié par Fried (1966) lequel introduisit la quantité r_0, diamètre d'une ouverture sur laquelle le moindre carré de la variation de phase est à peu près 1 radian[2]. Par conséquent, la taille effective de la FTO (largeur à mi-hauteur) est λ/r_0. Dans le cas d'un télescope de 10 m, une turbulence atmosphérique caractérisée par r_0 (550nm) = 10cm réduit la résolution angulaire à $1.4''$, soit le pouvoir de résolution d'un télescope amateur.

Plusieurs techniques sont disponibles pour restaurer partiellement la limite de diffraction des images pour les grands télescopes : l'interférométrie des tavelures (Labeyrie 1970), l'utilisation de masques pupillaires (Baldwin et al. 1986), l'optique adaptative (Beckers 1993) et la technique dite de "lucky exposure" (Baldwin et al. 2001). Toutes ces techniques présentent des imperfections telles que : sensibilité limitée, artefacts dans les processus de reconstruction d'image et problèmes de calibration.

Cependant, la dimension des télescopes ne peut être accrue indéfiniment, les raisons principales étant la masse des miroirs, et les spécifications très contraignantes sur l'ensemble de la structure qui peut fléchir sous son propre poids. Les radio-astronomes ont construit des télescopes orientables dont la taille atteint environ 100 m, mais n'ont pu construire de structures plus importantes pour des raisons similaires. Des projets de construction de télescopes de 100 m de diamètre ont été proposés (Gilmozzi et al. 1998) mais le défit technologique que cela représente est toujours impressionnant.

Les interféromètres optiques et infra-rouges ne souffrent pas des limitations dues à la taille des télescopes, puisqu'ils mélangent la lumière de télescopes indépendants et de tailles relativement modestes pour atteindre une résolution angulaire bien meilleure que celle d'un télescope individuel. La résolution angulaire d'un interféromètre est égale à celle d'un télescope dont le diamètre équivalent serait la distance séparant les télescopes individuels. A cette distance, également appelée base de l'interféromètre b, correspond une résolution angulaire b/λ.

1.2 Bref Historique de l'Interférométrie

Les premières expériences d'interférométrie stellaire optique furent réalisées par Stéphan (1873, 1874). Il appliqua les idées proposées par Fizeau (1868) qui pensait placer un masque percé de deux trous devant une lunette afin de mesurer le diamètre de sources stellaires. Stéphan réalisa son expérience à l'observatoire de Marseille. Il utilisa deux masques, dont les trous étaient espacés de 0.5m et 0.65m, placés à la surface du miroir du télescope de Foucault (0.8m) et essaya de mesurer les diamètres angulaires d'étoiles. A la fin de ses observations, il conclut que toutes les étoiles qu'il avait observées devaient avoir un très petit diamètre angulaire puisqu'il avait toujours mesuré des franges très contrastées.

Les premiers résultats astronomiques en interférométrie optique furent obtenus par Michelson (1891). Un masque percé de deux trous, superposé au miroir du télescope de 12 pouces (0.3m) à Mount Hamilton, permit à Michelson de mesurer le diamètre des satellites de Jupiter. Plus tard, en étendant la base au moyen d'un train optique constitué de quatre miroirs (Fig. 1.1), il fut capable de mesurer les diamètres et séparations d'étoiles avec un pouvoir de résolution accru par rapport au système original utilisant un masque. Ce principe lui permit de maintenir l'espacement des franges d'interférence constant, ce dernier dépendant uniquement de l'espacement de la paire de miroirs internes. L'assemblage optique fut installé sur le télescope de Hooker à Mount Wilson, choisi pour la robustesse de sa monture. Avec ce système, Michelson & Pease (1921a,c, 1923) mesurèrent les diamètres de plusieurs étoiles super-géantes.

Après les travaux précurseurs de Pease (1931), qui étudia la possibilité d'un train optique de 50 pieds, l'interférométrie stellaire longue base fut considérée trop difficile à mettre en œuvre avec des ouvertures indépendantes, aux longueurs d'onde visibles, à cause de l'instabilité mécanique du système. Cependant, l'importance des résultats obtenus par Michelson et Pease ne pouvait pour autant être négligée. Il était évident pour Michelson lui-même que les franges observées contenaient non seulement des informations sur le diamètre de la source mais aussi sur la distribution d'intensité de la source.

Après les résultats de Michelson et Pease, Brown & Twiss (1958) expérimentèrent avec succès la détection homodyne avec ce qu'ils appelèrent "interféromètre d'intensité". L'idée était que si les fluctuations d'intensité mesurées par deux collecteurs indépendants proches étaient corrélées, alors la diminution du degré de corrélation,

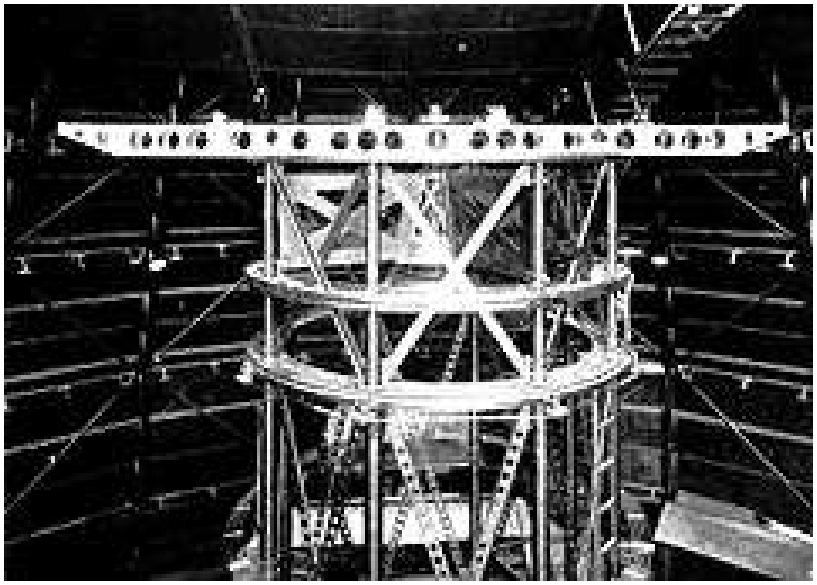

Fig. 1.1.— Le train optique de Michelson placé sur le télescope de Hooker à Mount Wilson en Californie. Avec ce dispositif, Michelson et Pease mesurèrent les diamètres de plusieurs étoiles super-géantes. Les quatre miroirs utilisés pour augmenter la résolution du télescope sont tout juste visible sur le dessus de la poutre. (Image : Musée de l'Observatoire du Mt. Wilson)

due à l'augmentation de la séparation entre les collecteurs, permettrait la détermination du diamètre angulaire de la source observée. La version de 1956 de l'instrument était constituée de deux miroirs où la lumière était collectée par deux photo-multiplicateurs, leurs signaux étaient ensuite amplifiés, puis envoyés vers un multiplicateur analogique. La valeur moyenne du produit intégré sur plusieurs heures mesurait l'inter-corrélation entre les fluctuations d'intensité des deux collecteurs. L'idée fut appliquée avec succès à la construction d'interféromètres avec des bases mesurant jusqu'à 200m. L'avantage de ce type d'assemblage était l'insensibilité à la turbulence atmosphérique et aux instabilités du système, principaux désavantages de l'interférométrie de Michelson. Malheureusement, l'extrêmement basse sensibilité limita les applications possibles.

L'intérêt pour la détection directe par interférométrie otique resta en sommeil jusqu'à ce que Labeyrie (1975) obtienne pour la première fois des franges d'interférence sur l'étoile Vega avec deux télescopes de 25cm séparés de 12m, ouvrant ainsi la voie à l'interférométrie optique et infra-rouge moderne.

1.3 Principes de l'Interférométrie Stellaire

Un interféromètre est un dispositif destiné à mesurer le degré de cohérence de la radiation électromagnétique entre deux (ou plus) éléments séparés[1]. La méthode utilisée pour mesurer cette cohérence change avec la longueur d'onde à laquelle l'observation est réalisée. Dans le domaine des ondes radio, où les photons sont nombreux et la source de bruit dominante est le bruit de détecteur, les champs électriques détectés par les antennes sont amplifiés et convertis à des fréquences plus basses au moyen d'un récepteur hétérodyne (en mélangeant le signal à un oscillateur cohérent). Les signaux sont ensuite échantillonnés et corrélés numériquement. A de plus courtes longueurs d'onde radio, les largeurs de bandes utilisables deviennent progressivement plus grandes, la corrélation est calculée au moyen de multiplicateurs analogiques après amplification et division de fréquence.

Autour de 10 μm, l'aspect corpusculaire de la lumière devient apparent. Le bruit de photon devient comparable au bruit de détecteur et cette longueur d'onde est la plus courte à laquelle la mesure interférométrique est réalisée par détection hétérodyne (de Batz et al. 1973; Sutton et al. 1976). Pour de plus courtes longueurs d'onde, il n'y a plus de bénéfice à amplifier le signal, ce qui met en évidence les grands avantages de la radio-astronomie.

A ce point, la détection directe est la seule voie envisageable avec la technologie actuelle. En interférométrie optique et infra-rouge, la lumière arrivant de télescopes indépendants est directement recombinée et la cohérence est mesurée à partir du contraste des franges détectées par un détecteur quadratique (un détecteur qui mesure uniquement le carré du champ électrique incident et perd l'information de phase du champ électrique).

1.3.1 Interférométrie et Expérience des Trous d'Young

Le corrélateur d'un interféromètre optique/infra-rouge est un dispositif dans lequel une onde incidente est divisée en deux faisceaux, lesquels sont recombinés soit en plan image, au moyen d'une lentille ou d'un miroir, soit en plan pupille, au moyen de lames séparatrices. Les faisceaux recombinés produisent une figure d'interférence, de manière similaire à l'expérience réalisée par le physicien britannique Thomas Young en 1801, dite expérience des trous d'Young. Thomas Young mit en évidence des interférences lumineuses en faisant passer un faisceau lumineux entre deux fentes, apportant la preuve cruciale de la nature ondulatoire de la lumière.

La lumière arrivant d'une source éloignée passe au travers d'une fente primaire, illuminant un écran σ_1 percé de deux fentes secondaires proches.

Le champ électrique de chaque fente secondaire se propage jusqu'à l'écran d'observation σ_0, avec des chemins optiques différents, interférant de manière constructive

[1]Pour une introduction détaillée à l'interférométrie, consulter Lawson (2000); Thompson et al. (2001); Hecht & Zajac (1974); Steward (1989)

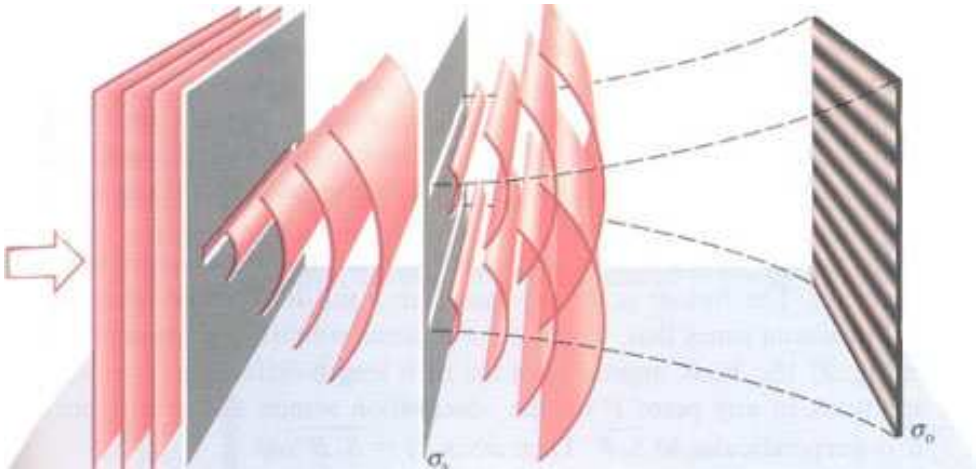

Fig. 1.2.— L'expérience classique des trous d'Young. La lumière en provenance d'une source distante passe au travers d'une fente primaire puis illumine un écran σ_1 percé de deux fentes secondaires proches. Des franges sombres alternées avec des franges brillantes peuvent être observées sur l'écran σ_0. (Hecht & Zajac 1974).

et destructive à différents points de l'écran créant la figure d'interférence illustrée Fig. 1.2., où des franges sombres sont alternées avec des franges brillantes. La fréquence des franges est proportionnelle à la séparation des fentes secondaires B.

1.3.2 Application à l'astronomie

Ce concept peut être étendu à des sources astronomiques. Dans ce cas, les deux fentes peuvent être les trous d'un masque superposé au miroir d'un télescope, ou encore, des télescopes indépendants où les faisceaux sont recombinés au moyen de systèmes optiques relativement complexes. Dans l'interféromètre générique, illustré Fig. 1.3, le front d'onde provenant d'une source stellaire est échantillonné par deux ouvertures générant deux faisceaux que l'on fait ensuite interférer. Des franges d'espacement $\Delta\Theta = \lambda/B$ radians et de fréquence $u = B/\lambda$ radians^{-1} sont visibles sur l'écran S. Ces franges sont virtuellement projetées sur le plan du ciel, comme si le plan du ciel était échantillonné par une fonction sinusoïde de période $\Delta\Theta$ dans la direction de B.

Une seconde source, séparée de la première par une distance angulaire β (dont la lumière est incohérente avec celle de la première source) va produire un second système de franges translaté en phase. Si cette séparation β est égale à $\lambda/2B$ et la brillance des objets est la même, les deux systèmes de franges vont être en opposition de phase et s'annuler l'un l'autre, produisant une illumination uniforme de l'écran. Fig. 1.3 (a) illustre le cas où les deux systèmes de franges sont en opposition de phase, mais n'ont pas la même amplitude. Dans ce cas, des franges de faible contraste sont visibles sur l'écran.

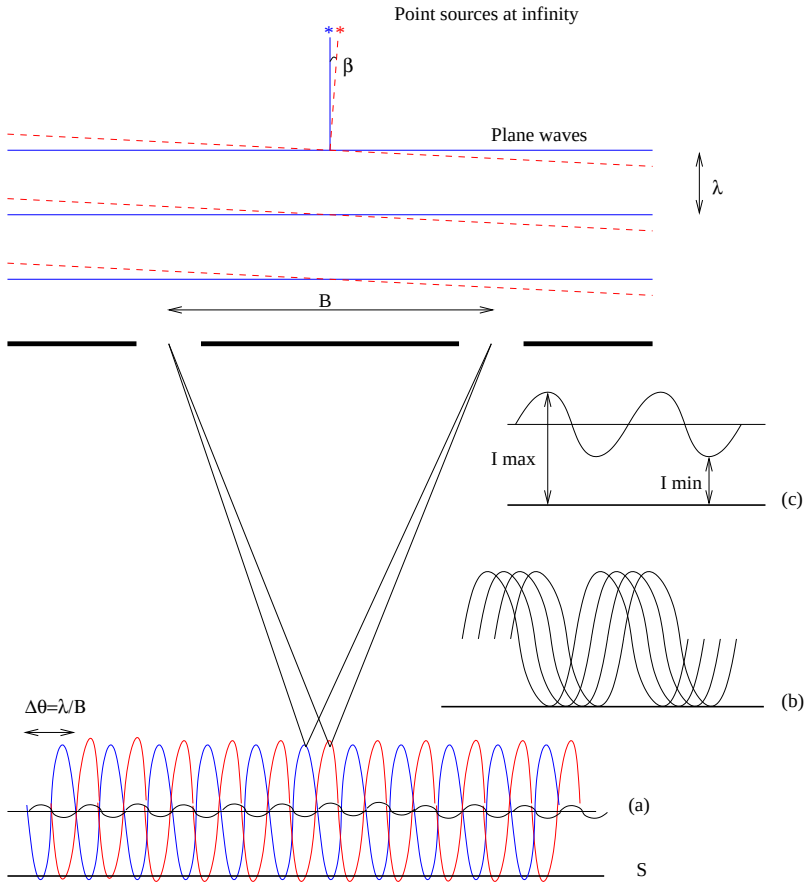

Fig. 1.3.— Expérience des trous d'Young appliquée à l'astronomie : la lumière provenant de deux objets stellaires distants illumine l'ouverture d'un télescope sur lequel est placé un masque pupillaire. Les étoiles génèrent deux fronts d'onde indépendants (trait plein et tirets) qui arrivent au télescope avec des angles différents. Les fronts d'onde sont divisés produisant chacun deux faisceaux que l'on fait ensuite interférer, ce qui forme deux systèmes de franges sur l'écran S. Ces systèmes de franges sont de même fréquence, mais leur position (phase) dépend de la position angulaire de l'objet sur le plan du ciel. Sur l'écran sera visible la superposition des deux systèmes de franges. La visibilité (contraste) du système global dépendra de la phase relative des deux sinusoïdes. De même, un objet résolu par la base B produira un système de franges pour chaque point non-résolu de l'objet (b). La combinaison de ces systèmes de frange donne sur l'écran une figure d'interférence dont le contraste est réduit (c).

Le contraste des franges peut également être réduit lorsque la taille angulaire de l'objet est non négligeable par rapport à l'inter-frange, comme illustré Fig. 1.3 (c). Chaque élément non résolu de l'objet se comporte comme une source ponctuelle et produit un système de frange. La combinaison de ces systèmes de frange donne sur l'écran une figure d'interférence dont le contraste est réduit. Michelson définit la

visibilité des franges V_M, comme la mesure de l'amplitude normalisée des franges, soit

$$V_M = \frac{I_{max} - I_{min}}{I_{max} + I_{min}} \tag{1.1}$$

où I_{max} et I_{min} sont respectivement le maximum et minimum d'intensité mesurés sur les franges. On peut remarquer qu'avec cette définition, la visibilité est normalisée à l'unité lorsque le minimum d'intensité est zéro, c'est à dire, lorsque la taille angulaire de l'étoile est très petite par rapport à la largeur d'une frange. Si la visibilité des franges est considérablement plus petite que l'unité, l'étoile est dite "résolue" par l'interféromètre. Les franges ne donnent une information sur la résolution de l'étoile que dans la direction parallèle à la séparation des deux ouvertures. Dans la direction orthogonale, la réponse est simplement proportionnelle à l'intensité intégrée sur un angle solide.

1.3.3 La Recombinaison des Faisceaux

Plusieurs méthodes peuvent être utilisées pour recombiner les faisceaux d'un interféromètre. Pour une introduction complète sur le sujet, voir Traub (1986, 2000). Historiquement, le principe de recombinaison de Fizeau fut le premier jamais conçu et visait à mesurer la taille de sources stellaires. Il fut tout d'abord implanté en utilisant un masque pupillaire sur un télescope (voir Sec. 1.2). L'interféromètre stellaire de Fizeau a récemment été redécouvert. Un masque pupillaire percé de plusieurs trous a été utilisé pour obtenir des images à haute résolution angulaire de sources stellaires et de leur environnement circumstellaire (Baldwin & Warner 1987; Buscher et al. 1990; Tuthill et al. 2001b,a).

Fig. 1.4 montre l'assemblage optique d'un interféromètre stellaire Fizeau (dit FSI). Un FSI n'est pas nécessairement constitué d'un télescope muni d'un masque pupillaire. Un système optique, constitué d'ouvertures indépendantes, dans lequel la pupille de sortie est simplement une version réduite de la pupille d'entrée, peut être considéré comme un interféromètre de Fizeau. Cette méthode de recombinaison est également appelée méthode "homothétique".

Dans un interféromètre de Michelson (dit MSI), la pupille de sortie est ré-imagée au moyen de miroirs périscopes (Fig. 1.5). Dans ce système optique, la pupille de sortie n'est pas une version réduite de la pupille d'entrée. Cette méthode est également appelée "densification de pupille" (Labeyrie 1996). Cette configuration présente plusieurs avantages, particulièrement lorsqu'utilisée comme corrélateur optique. Le principal avantage est que la fréquence des franges est indépendante de la base B et dépend seulement de la distance b séparant les sous-pupilles. Ceci était crucial pour Michelson qui estimait visuellement la visibilité des franges. Un interféromètre de Fizeau aurait généré des franges à trop haute fréquence, du fait de la grande longueur de base B. Cela aurait rendu les franges invisibles à l'œil nu. De plus, les pupilles ré-imagées offrent la possibilité de réorganiser les sous-pupilles de sortie de manière redondante ou non. Une pupille est redondante lorsque deux bases, ou plus,

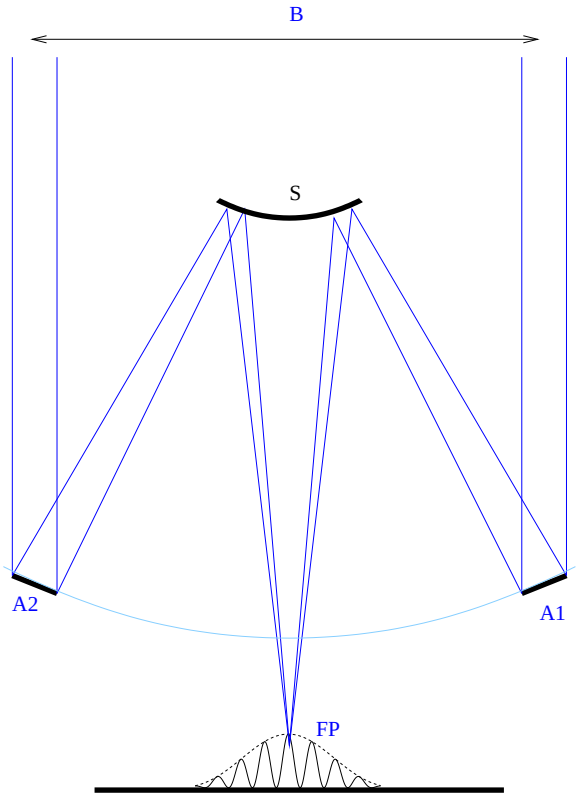

Fig. 1.4.— Interféromètre stellaire de Fizeau. L'onde plane provenant d'une source stellaire distante passe au travers d'un masque pupillaire placé devant un télescope. Les deux faisceaux résultants sont réfléchis par le miroir primaire vers les points A1 et A2 avant d'être renvoyé par le miroir S en un foyer commun. Des franges sont formées dans le plan focal FP. A1 et A2 pourraient tout aussi bien être des miroirs séparés. Des franges d'interférence se forment si la différence de chemin optique entre les faisceaux est maintenue proche de zéro. La résolution angulaire et fréquence des franges sont fixées par la base B, distance entre les deux ouvertures.

sont de même longueur et orientation. Cela présente des avantages pour l'extraction des phases à partir des mesures de clôture de phases (voir Sec. 1.3.4). Cela présente également l'avantage non négligeable de pouvoir obtenir des images directes, à haute dynamique, lorsqu'au moins 6 ouvertures sont recombinées et co-phasées (différence de chemin optique inférieure à une fraction de longueur d'onde) selon ce schéma optique (Labeyrie 1996; Boccaletti et al. 2000; Riaud et al. 2002; Riaud 2003; Borkowski et al. 2002; Gillet et al. 2003).

Les méthodes de recombinaison décrites jusqu'à présent sont des méthodes dites de recombinaison en plan image. Cela signifie que les sous-images des ouvertures individuelles sont transportées en un foyer commun et sont superposées dans le plan image. Une autre méthode très répandue en interférométrie optique/infra-rouge, est

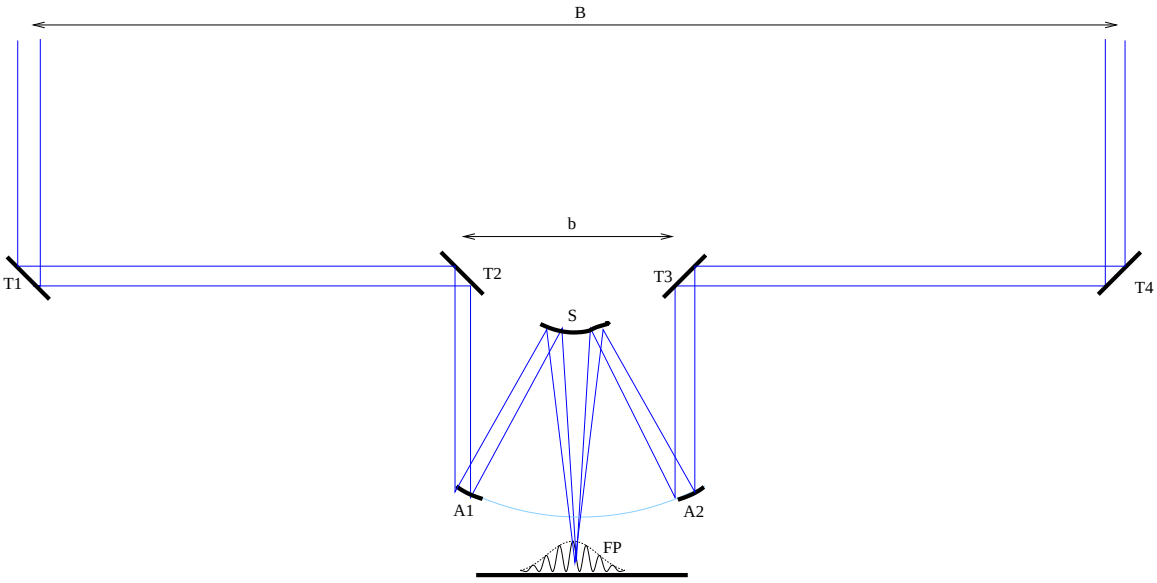

Fig. 1.5.— Schéma de principe du train optique utilisé par Michelson et Pease au télescope de Hooker : quatre miroirs placés dans un arrangement de type périscope, augmentent la base maximale B, tout en conservant la fréquence des franges fixées par la longueur b. Ce périscope permit à Michelson de voir des franges qui auraient été beaucoup trop fines pour être vues avec un interféromètre de Fizeau de base équivalente et augmenta la résolution angulaire accessible au télescope de Hooker.

la recombinaison en plan pupille. Avec cette méthode, les faisceaux sont mélangés et superposés dans un plan pupille au moyen de lames séparatrices. Les faisceaux recombinés sont ensuite focalisés sur des détecteurs mono-pixel ou dispersés pour obtenir de la résolution spectrale. L'information des franges est extraite en appliquant une modulation temporelle du chemin optique, et enregistrée comme séquence temporelle par les deux détecteurs (Fig. 1.6).

1.3.4 Méthodes Indirectes de Reconstruction d'images

Théorème de Van Cittert-Zernike

Une importante application du théorème de Van Cittert-Zernike (Born & Wolf 1999; Traub 2000) est que la distribution de brillance d'une source peut être calculée à partir de la transformée de Fourier de la fonction d'inter-corrélation déduite des visibilités et phases des franges.

Soit une source étendue, quasi-monochromatique et incohérente sur le plan du ciel. Le champ lumineux radié est mesuré en deux points P_1 et P_2, séparé du vecteur $\vec{B}$. Les champs éléctriques E_1 et E_2 sont mésurés en P_1 et P_2. La fonction normalisée de cohérence mutuelle du champ lumineux aux points P_1 et P_2, qui est aussi le degré

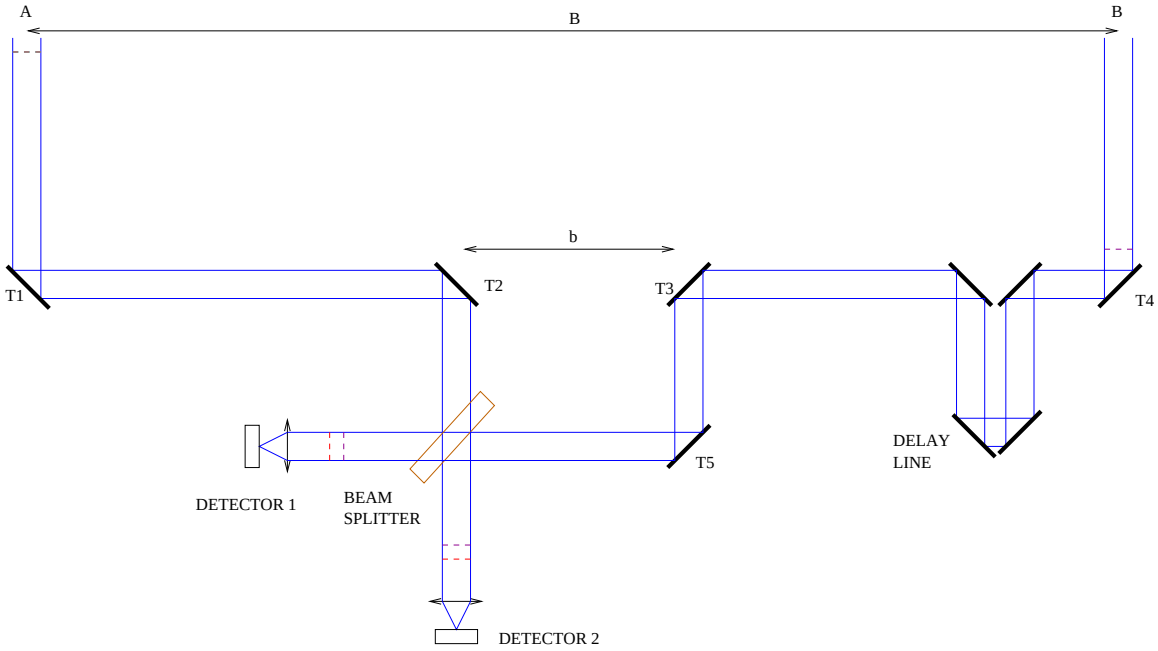

Fig. 1.6.— Recombinaison de faisceaux en plan pupille : Un train optique de type Michelson est utilisé pour transporter les faisceaux jusqu'au recombineur, dans ce cas une lame séparatrice superpose les deux fronts d'onde dans un plan pupille. Les deux faisceaux émergeant de la lame séparatrice sont focalisés sur un détecteur mono-pixel. Le chemin optique entre les deux faisceaux est modulé par une fonction triangulaire en bougeant la ligne à retard au moyen d'un actuateur piezo. La lame séparatrice introduit un déphasage de π entre les deux faisceaux (Traub 2000). Les signaux enregistrés (séries temporelles) sont des ondes sinusoïdales superposées à l'intensité incohérente des deux télescopes.

complexe de cohérence mutuelle (ou inter-corrélation), γ_{12} est défini comme suit :

$$\gamma_{12}\left(\vec{B}\right) = \frac{\langle E_1 E_2^* \rangle}{\sqrt{\langle |E_1|^2 \rangle \langle |E_2|^2 \rangle}}. \tag{1.2}$$

Il peut être montré que lorsque P_1 et P_2 sont proches et que le diamètre de la source est petit par rapport à sa distance au plan de mesure, le degré complexe de cohérence mutuelle est égale à la transformée de Fourier normalisée de la distribution de brillance de la source.

$$\gamma_{12}\left(\vec{B}\right) = \frac{\int I\left(\vec{\alpha}\right) \exp\left(-ik\vec{B}\cdot\vec{\alpha}\right) d\vec{\alpha}}{\int I\left(\vec{\alpha}\right) d\vec{\alpha}}, \tag{1.3}$$

où $\vec{B}$ est le vecteur de base entre deux télescopes, $I\left(\vec{\alpha}\right)$ la distribution d'intensité de la source sur le plan du ciel, $\vec{\alpha}$ la coordonnée bi-dimensionnelle dans le plan du ciel, et $k = 2\pi/\lambda$ avec λ la longueur d'onde d'observation. Les intégrales sont sur le

champ de vue bi-dimensionnel d'une ouverture individuelle. La visibilité d'une source est le module de γ_{12} et la phase des franges, l'argument de γ_{12}. Après avoir mesuré la visibilité et la phase pour plusieurs vecteurs de base, une image de la source peut être obtenue en utilisant la relation inverse de Eq. 1.3.

Les Mesures de Clôture de Phase

L'information de phase des franges mesurée par un interféromètre composé de deux ouvertures, est corrompue par la turbulence atmosphérique, laquelle change l'indice de réfraction du milieu et crée des variations aléatoires du chemin optique. L'information de phase de la fonction de cohérence est fondamentale pour la reconstruction d'images, et sans cette information, les images d'objets complexes ne peuvent pas être obtenues. Cependant, il fut démontré par Jennison (1958), que l'information de phase peut être partiellement restaurée si plus de deux télescopes sont utilisés.

Brièvement, lorsque trois télescopes échantillonnent le front d'onde corrompu par l'atmosphère, les phases des fonctions de cohérence mésurées pour chaque paire de télèscopes seront egales à :

- Un terme associé à la position de l'objet par rapport au plan de mesure. J'appelle ce terme phase intrinsèque ψ_{ij}.
- Un terme associé à l'index de refraction de l'atmosphère, lequel change de manière aléatoire.
- Un terme associé aux erreurs instrumentales dues à des imperfections de l'instrument.

Je traite les deux derniers termes comme une seule erreur globale appellée ϕ_k. Pour chaque paire d'ouverture j'écris Φ_{ij} comme étant la somme des phases intrinsèques ψ_{ij} et de l'erreur due à l'atmosphère et à l'instrument même.

$$\begin{aligned} \Phi_{12} &= \psi_{12} + (\phi_2 - \phi_1) \\ \Phi_{23} &= \psi_{23} + (\phi_3 - \phi_2) \\ \Phi_{31} &= \psi_{31} + (\phi_1 - \phi_3) \end{aligned} \tag{1.4}$$

La clôture de phase est la somme des phases de la function de coherence de chaque paire de télescopes, sur un triangle fermé comprenant trois télescopes,

$$\begin{aligned} \Phi_{123} &= \psi_{12} + (\phi_2 - \phi_1) + \psi_{23} + (\phi_3 - \phi_2) + \psi_{31} + (\phi_1 - \phi_3) \\ &= \psi_{12} + \psi_{23} + \psi_{31} \end{aligned} \tag{1.5}$$

Comme montré Eqn. 1.5, les contributions atmosphériques et instrumentales de la phase ϕ, ajoutées à la phase intrinsèque, s'annulent, laissant uniquement la somme des contributions de la phase intrinsèque de chaque paire de télescopes. Lorsque N télescopes sont utilisés, le nombre de phases indépendantes que l'on peut mesurer est N_Φ, le nombre de triangles possibles est N_T et le nombre de clôtures de phase indépendantes est $N_{\Phi CL}$, avec

$$N_\Phi = N\left(N-1\right)/2 \tag{1.6}$$

$$N_T = N\,(N-1)\,(N-2)\,/6 \quad (1.7)$$
$$N_{\Phi CL} = (N-1)\,(N-2)\,/2\,. \quad (1.8)$$

Le nombre de triangles indépendants est inférieur au nombre maximal de phases existant pour N télescopes. Il n'est donc pas possible de restaurer l'intégralité de l'information de phase théoriquement disponible.

1.3.5 Imagerie Directe

J'ai décrit jusqu'à présent l'utilisation d'un interféromètre comme corrélateur. La mesure de la visibilité des franges permet de déterminer la distribution de brillance d'objets simples par ajustement de modèles aux données. Au sol, la turbulence atmosphérique empêche la mesure des phases lesquelles sont des quantités fondamentales à la reconstruction d'images. Lorsque plusieurs ouvertures sont utilisées (au moins 3), il est cependant possible de restaurer partiellement l'information de phase et reconstruire des images d'objets complexes à partir des mesures de clôture de phase (Sec. 1.3.4).

Cependant, des images directes peuvent être obtenues au foyer d'un interféromètre, si un nombre suffisant d'ouvertures (au moins 6) est utilisé et si les ouvertures sont co-phasées en utilisant l'équivalent d'une optique adaptative (Borkowski et al. 2002). L'utilisation de miroirs périscopes rend la formalisation mathématique d'un interféromètre à pupille densifiée (DPI) très complexe, tandis que le formalisme décrivant un interféromètre à pupille homothétique (HPI) est relativement simple, comme montré par Traub (1986); Beckers (1986); Tallon & Tallon-Bosc (1992). La relation objet stellaire/image observée ne peut plus être décrite par une relation de convolution classique mais par une pseudo-convolution comme il a été démontré par Labeyrie (1996). Fig. 1.7 montre un HPI à deux télescopes.

Fig. 1.8 représente un DPI à deux télescopes ; B est la base de la pupille d'entrée. L'effet du ré-arrangement des pupilles est de réduire la base B à la longueur de b tout en conservant le diamètre des sous-pupilles. Ce DPI peut immédiatement être transformé en un HPI si b égale B. Si une étoile hors-axe par un angle β est imagée par le système, le front d'onde reçu par chaque télescope est également basculé d'un angle β produisant un retard relatif entre les deux faisceaux $d = \beta B$. Dans le plan focal, les sous-images sont superposées et éloignées d'un angle β du foyer (en supposant un facteur d'agrandissement du système égal à 1), par-contre, le système de frange est centré à un angle $\beta' = d/b$ du foyer. La relation de convolution standard n'existe plus et est remplacée par la pseudo-convolution (Labeyrie 1996)

$$\mathcal{B}(x,\beta) = \int O(\beta)A(x+\beta)I(x+\gamma_d\beta)d\beta \quad (1.9)$$

où $\gamma_d = B/b$ est le rapport des distances entre les pupilles d'entrée et les pupilles de sortie, $\mathcal{B}$ est la distribution d'intensité dans le plan focal, O est la fonction objet, A est la transformée de Fourier de la sous-ouverture (une fonction d'Airy si la sous-ouverture est circulaire) et I est la transformée de Fourier de la fonction décrivant

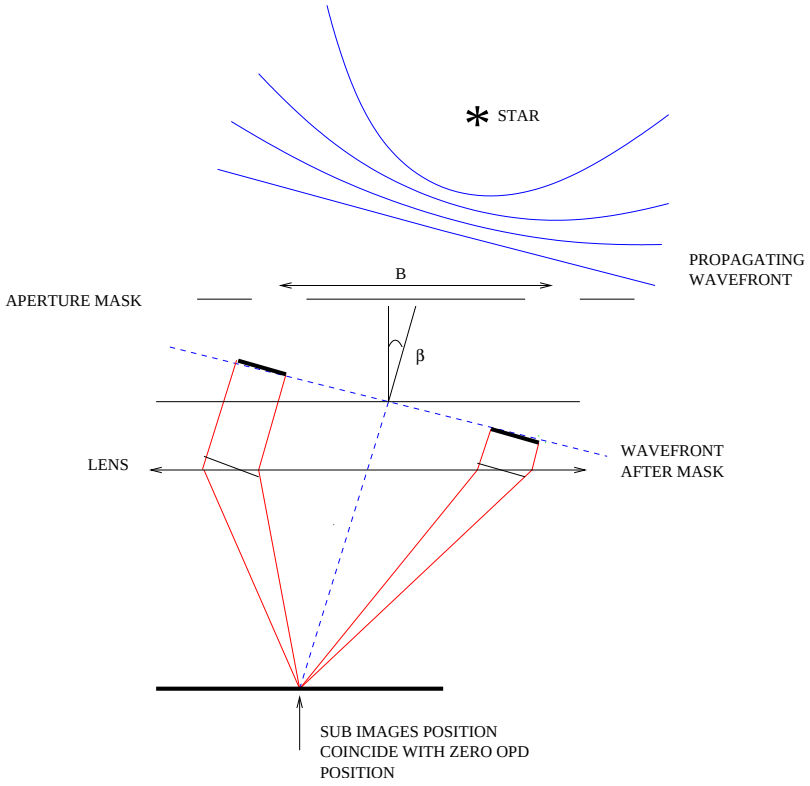

Fig. 1.7.— Dans un HPI, la pupille de sortie correspond exactement à la pupille d'entrée. Les sous-images se superposent dans le plan focal commun et les interférences se produisent toujours au point de superposition des sous-images, c'est-à-dire qu'il existe une relation de convolution entre l'objet dans le plan du ciel et la figure d'interférence dans le plan focal.

la position des ouvertures ou "fonction d'interférence". Cette dernière fonction est équivalente au "faisceau synthétique" défini en radio interférométrie par synthèse d'ouvertures. La dégradation de l'image par un DPI se réduit alors à une diminution du champ de vue (FOV) due au déplacement, dans le plan image, de la fonction d'Airy des sous-ouvertures avec β, plus lent que le déplacement de la fonction d'interférence I. Ceci produit un effet de fenêtrage. Tallon & Tallon-Bosc (1992) ont montré que la dégradation de l'image peut être corrigée, a posteriori, dans le domaine de Fourier. Un exemple de fonction d'interférence, pour un interféromètre à multiples ouvertures, est donné Fig. 1.9. Le front d'onde basculé, échantillonné par plusieurs ouvertures, est densifié et prend la forme de marches d'escalier. Les marches produisent plusieurs fonctions d'Airy superposées et le front d'onde moyen produit un faisceau synthétisé déplacé par rapport à la fonction d'Airy, ce qui restreint le champ de vue de ce type d'instrument.

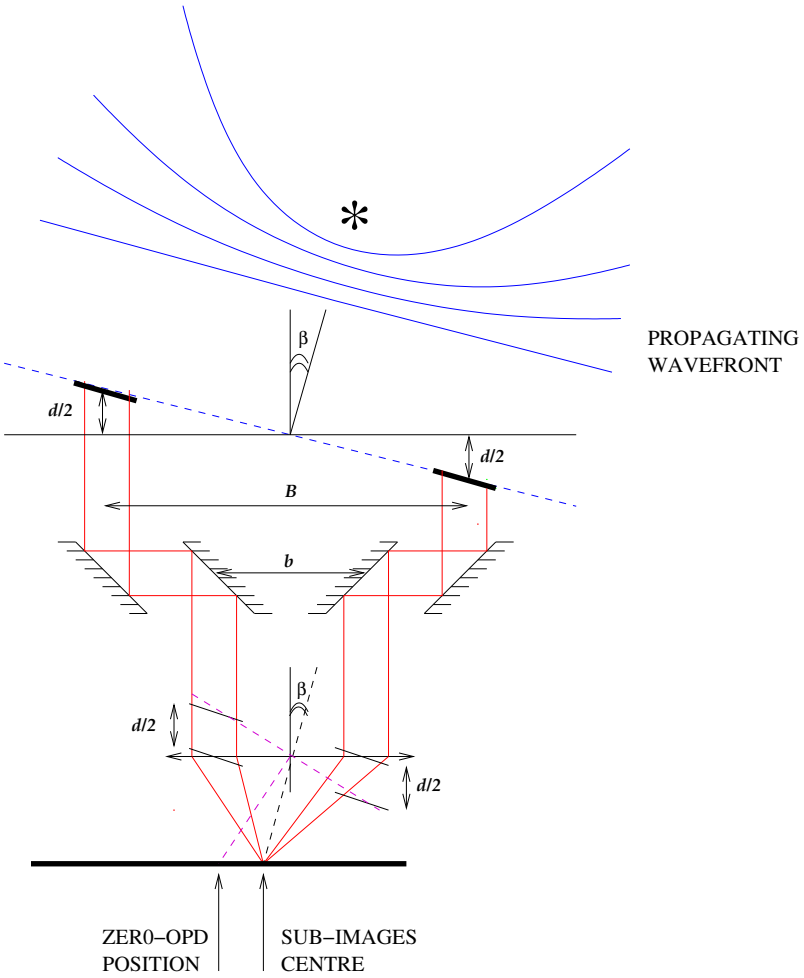

Fig. 1.8.— Un DPI à deux télescopes : Une source stellaire distante produit un front d'onde basculé d'un angle β par rapport à la pupille d'entrée de l'interféromètre. Dans ce schéma, B et b sont respectivement les bases avant et après ré-arrangement de la pupille, et d est la différence de chemin optique introduite par le basculement du front d'onde.

1.4 Science par Interférométrie Optique et Infrarouge

Dans cette section, je donne une vue d'ensemble de l'incroyable potentiel scientifique de l'interférométrie optique et infra-rouge, technique qui dans le futur contribuera à repousser les frontières de l'astrophysique. La précédente génération d'interféromètres produisit une riche quantité de données sur les diamètres angulaires d'étoiles, permettant la mesure d'importantes constantes physiques des étoiles. La nouvelle génération d'interféromètres, dotée d'une meilleure sensibilité et d'une meilleure résolution angulaire, commence maintenant à produire des résultats scientifiques pas-

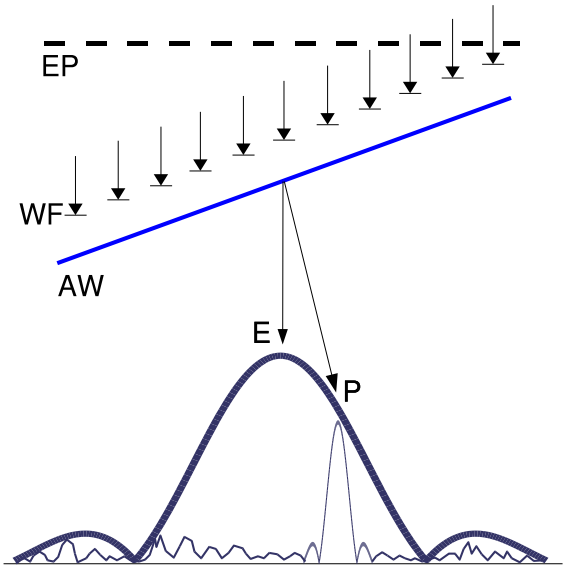

Fig. 1.9.— Un DPI à ouvertures multiples. Le système optique n'est pas représenté sur cette figure. Le front d'onde basculé incident (WF) prend la forme de marches d'escalier après passage par la pupille d'entrée (EP) du DPI. Les sous-images sont superposées au point E et les chemins optiques pour les différentes ouvertures sont égalisés au point P (Labeyrie (1996)).

sionnants sur les objets stellaires et extra-galactiques tandis que des missions spatiales telles que SIM (Space Interferometry Mission), TPF (Terrestrial Planet Finder) et Darwin ont été conçues pour découvrir des planètes extra-solaires et, un jour, produire des images de celles-ci. Dans les prochains paragraphes, je discute quelques-uns des objectifs scientifiques de l'interférométrie stellaire optique et infra-rouge.

1.4.1 Les Étoiles Extrêmes

Variables bleues lumineuses

Les étoiles variables bleues lumineuses (LBV) sont d'intéressantes étoiles massives super-géantes qui présentent de fortes raies d'émission, des variations temporelles et des pertes de masse. P Cygni a fait l'objet d'une attention toute particulière, à la fois des théoriciens et des observateurs, en tant qu'archétype de cette classe d'étoiles. Aux longueurs d'onde du visible, cette étoile présente une enveloppe étendue qui a été résolue pour la première fois avec l'interféromètre GI2T (Vakili et al. 1997). De récentes observations avec optique adaptative (Chesneau et al. 2000) montrent une étoile non-résolue entourée d'une enveloppe contenant des bulbes de matière. L'imagerie interférométrique pourrait permettre de contraindre la structure du vent stellaire et donner un nouvel éclairage sur l'état d'évolution de ces objets en permettant l'accès

à des structures plus fines du vent stellaire autour de l'étoile.

Étoiles Be

Une première tentative pour mesurer la déformation géométrique des rotateurs rapides que sont les étoiles Be, fut entreprise en 1974 avec l'interféromètre d'intensité de Narrabri sur l'étoile Altair, par Hanbury Brown et al. (1974). Cependant, ces observations ne permirent pas de décider entre différents modèles pour cette étoile. Plus récemment, van Belle et al. (2001) observa Altair avec l'interféromètre PTI (Palomar Test-bed Interferometer), mesura un rapport apparent demi-grand axe/demi-petit axe égal à 1.140 ± 0.029 et établit des contraintes sur la relation entre la vitesse de rotation de l'étoile et son inclinaison. (Domiciano et al. 2003) ont récemment observé au VLTI (Very Large Telescope Interferometer) une étoile Be peu commune. Achernar est une étoile dont la masse est six fois celle du soleil. Sa température de surface est environ 20000K et sa distance de 145 années lumières. La géométrie apparente d'Achernar indique un rapport demi-grand axe/demi-petit axe étonnamment élevé de 1.56 ± 0.05. Ceci est évidemment le résultat de la rotation rapide d'Achernar. Le rapport mesuré entre l'axe équatorial et l'axe polaire d'Achernar constitue un défit sans précédent pour l'astrophysique théorique, en particulier en ce qui concerne les pertes de masse depuis la surface, accentuées par la rotation rapide, mais également pour ce qui est de la distribution du moment angulaire interne.

Géantes et Super-Géantes de Type M

Les étoiles évoluées, comme les géantes et super-géantes de type M, sont des objets très complexes avec des atmosphères contenant des molécules qui peuvent, aux longueurs d'onde du visible, faire écran aux observations directes de la surface de l'étoile. Les observations interférométriques dans l'infra-rouge moyen peuvent pénétrer au travers de ces couches épaisses et fournissent la haute résolution angulaire nécessaire pour révéler des détails à la surface de ce type d'étoiles.

L'imagerie de la super-géante Betelgeuse (α Orionis) apporte des preuves concluantes démontrant que la distribution de brillance de son disque est loin d'être uniforme pour la plupart des longueurs d'onde ; une tache brillante a été détectée à différentes longueurs d'onde. Cette caractéristique peut être modélisée par 1-3 taches non-résolues, sur un disque symétrique (Buscher et al. 1990), changeant de forme et de position sur une échelle de temps mensuelle (Wilson et al. 1997). L'une des explications favorisées pour décrire ces taches brillantes, est celle de la présence de cellules de convection géantes, prédites par Schwarzschild (1975). Elles expliqueraient les variations photométriques irrégulières observées sur les étoiles géantes et super-géantes. Les taches brillantes seraient le sommet d'un jet convectif de température supérieure à celle du milieu environnant. Wilson et al. (1992) essayèrent sans succès de trouver une corrélation entre la magnitude de l'étoile en bande V et le flux de ces points chauds sur une échelle de temps de quatre mois.

Des observations interférométriques furent réalisées avec un masque pupillaire

au télescope William Hersheln en visible et à l'interféromètre COAST (Cambridge Optical Aperture Synthesis Telescope) en infrarouge proche (Young et al. 2000). Aux longueurs d'onde visibles l'etoile semblait très asymétrique. Les données ont été interprétées en utilisant de simples modèles de 1–3 taches blanches ou noires superposées à un disque assombri (assombrissement centre-bord). Les taches furent interprétées comme une variation d'opacité dans l'atmosphère étendue de l'etoile en contraste avec l'hypothèse du jet convectif. A de plus courtes longueurs d'onde, l'étoile apparaît comme un disque uniforme. L'imagerie de sources complexes telles que Betelgeuse est cruciale pour obtenir des informations sur des structures récurrentes qui peuvent apparaître à la surface des étoiles évoluées. De récentes simulations obtenues à partir d'un code hydrodynamique 3D (Freytag 2003) ont été utilisées pour produire un modèle des couches externes de Betelgeuse. Ce modèle produit des structures à grande échelle très contrastées, pouvant expliquer les inhomogénéités observées dans la distribution de brillance de Betelgeuse. L'enveloppe convective est habituellement constituée de quelques grandes cellules de convection avec des durées de vie typiques de quelques mois ainsi que de plus petites cellules évoluant sur des échelles de temps plus courtes (et qui ne seront probablement pas observables dans un futur proche du fait de leur petite taille).

Étoiles Mira

Les étoiles Mira sont des étoiles froides et évoluées. Elles sont très grosses, plusieurs fois le rayon du soleil, et très lumineuses, plusieurs milliers de fois la luminosité du soleil. Elles présentent une atmosphère froide et étendue où la formation de molécules et de poussière prend place. Les Miras pulsent avec une période d'environ un an. Pendant leur cycle de pulsation, la magnitude visuelle change par un facteur d'environ 2.5 à 7.5.

En dépit d'un considérable travail observationnel, beaucoup d'aspects fondamentaux des variables Miras demeurent incertains. La détermination des tailles et formes des étoiles variables Miras, et de la variation temporelle de ces quantités est d'importance fondamentale pour la compréhension des structures de l'atmosphère stellaire.

Certaines Miras sont entourées d'une enveloppe de poussière et par conséquent sont très bien adaptées aux observations à haute résolution spatiale dans les longueurs d'onde du proche infra-rouge. Les effets de l'absorption atomique et moléculaire dans l'atmosphère stellaire sont beaucoup moins importants dans le proche infra-rouge que dans le visible, et donc, des mesures interférométriques devraient permettre de sonder l'étoile à travers l'atmosphère jusqu'à la photosphère.

1.4.2 Objets Stellaires Jeunes

L'existence d'une enveloppe de poussière autour des étoiles Herbig fut en premier déduite de la présence d'un fort excès infra-rouge par Mendoza (1966) et plus tard, directement avérée à partir de la détection de silicate par Cohen (1980). Bien que beaucoup ait été appris sur ces étoiles au cours des quarante dernières années, la

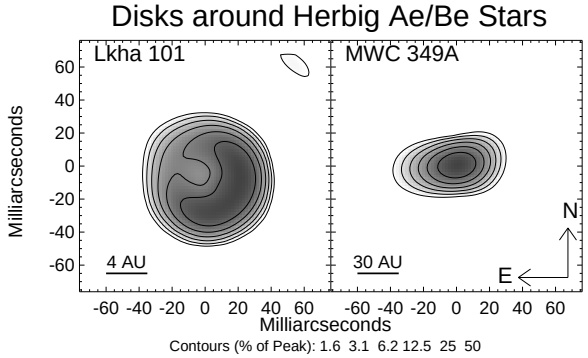

Fig. 1.10.— Disques protostellaires observés par la technique du masque pupillaire au télescope de Keck. (Tuthill et al. 2001a; Danchi et al. 2001).

question de la distribution géométrique de la poussière est controversée. Deux modèles son favorisés : le premier propose une distribution de la matière dans une enveloppe sphérique (Miroshnichenko et al. 1997), le second propose une structure en forme de disque (Hillenbrand et al. 1992). Les observations spectroscopiques ne permettent pas de distinguer sans ambiguïté entre les deux modèles, pour cette raison, seules des images à haute résolution angulaire pourraient résoudre la controverse.

La poussière fut résolue pour la première fois par Millan-Gabet et al. (1999b); Millan-Gabet (1999) avec l'interféromètre IOTA-2 (Infrared-Optical Telescope Array - 2 telescopes), lequel permettait mesurer la taille de ces structures mais pas de produire des images. Il trouva que les tailles, mesurées dans le proche infra-rouge, de la région émettrice étaient beaucoup plus grandes que précédemment supposées et qu'aucune des sources ne présentait de variation de visibilité lorsque l'orientation de la base de l'interféromètre changeait, indiquant une distribution de brillance centro-symétrique de l'objet. Les données obtenues pouvaient être expliquées par l'utilisation de simples modèles où la poussière est distribuée dans une enveloppe sphérique ou bien une fine coquille, et les tailles dans le proche infra-rouge seraient significativement plus grandes que les tailles prévues pour les modèles de disques.

Cependant, les observations effectuées avec un masque pupillaire à Keck (Tuthill et al. 2001a; Danchi et al. 2001) sur des étoiles plus massives (Figure 1.10), hors de la classification Herbig, montrèrent une distribution en forme de disque, pratiquement de face, avec un trou central (ou cavité) et un bord intérieur chaud. La cavité prouva être plus grande que prévue par la théorie. Les meilleurs ajustements aux visibilités mesurées dans les bandes J, H et K étaient des ellipses uniformes.

Seule une image haute résolution angulaire pourrait résoudre sans ambiguïté la controverse, établir la taille correcte pour la région d'émission de l'excès infra-rouge, et enfin décider de la distribution exacte de la poussière pour ces étoiles. Les étoiles Herbig Ae/Be ne peuvent pas être imagées avec la classe des télescopes de 10m. Seule l'interférométrie longue base peut atteindre la résolution angulaire requise.

1.4.3 Planètes Extra-Solaires

Ce qui à mon point de vue sera le domaine de recherche le plus passionnant et le plus prometteur pour la prochaine génération d'interféromètres, est la découverte et la caractérisation de planètes extra-solaires au moyen des techniques interférométriques. La question de l'existence de planètes de type Terre dans les zones "habitables" autour de leurs étoiles parents, où la température de surface est capable de supporter de l'eau liquide, pour un domaine de pressions de surface, sera adressée dans les prochaines années. Il sera possible de déterminer la composition de l'atmosphère de planètes terrestres orbitant des étoiles proches. En particulier, la présence d'eau, de monoxyde de carbone, ou de dioxyde de carbone sera établie. La découverte des composants atmosphériques, ou de conditions attribuable à des formes de vie primitives, telle que l'ozone ou d'oxygène, qui sont observés dans l'atmosphère terrestre, semble réalisable. Cela sera possible en utilisant de nouveaux équipements aux sols et dans l'espace. L'astrométrie de précision, pour la détection de planètes de masses équivalentes à la masse de la Terre, semble être possible à la fois depuis le sol et l'espace. Un nouvel instrument, PRIMA (Phase-Referenced Imaging and μas Astrometry), capable de détecter des planètes extra-solaires grâce à des mesures astrométriques de haute précision, est prévu pour être installé au VLTI. PRIMA est un instrument double-champ qui permettra d'augmenter la sensibilité du VLTI jusqu'à K=15-20 avec une résolution angulaire meilleure que 10 mas. Une haute précision astrométrique ($< 10\mu$as) permettra la détection de planètes extra-solaires.

Des expériences similaires pour des mesures astrométriques sont également prévues à l'interferomètre Keck. Une expérience de nulling, qui prévoit de réduire la lumière de l'étoile par interférences destructives afin d'imager les planètes peu lumineuses autour d'étoiles, est en progrès. L'astrométrie de précision peut être beaucoup mieux réalisée depuis l'espace où les fluctuations rapides générées par la turbulence atmosphérique sont remplacées par un déplacement lent et des vibrations introduites par le vaisseau spatial. SIM (Space Interferometry Mission), programmé pour être lancé en 2009, déterminera les positions et distances d'étoiles avec une précision plusieurs centaines de fois meilleure qu'aucun autre instrument. Cette précision permettra à SIM de déterminer les distances d'étoiles au travers de la galaxie et de sonder les étoiles proches pour la détection de planètes de type Terre. SIM sera un inestimable précurseur pour la mission d'imagerie de planètes : TPF (Terrestrial Planet Finder). Il sélectionnera les cibles pour cette mission plus efficacement que TPF lui-même qui nécessiterait de trop longs temps d'intégration (sous réserve que SIM atteigne les objectifs de précision astrométrique requis).

Le modèle standard décrivant la formation de systèmes solaires suppose que les planètes sont crées dans un disque plat de matière formé par l'effondrement de nuages de gaz et de poussière en rotation. Tandis que cette théorie a été appuyée par des observations de disques protoplanétaires d'une envergure de dizaines d'unités astronomiques, les découvertes récentes de planètes extra-solaires aux propriétés orbitales diverses suggèrent que les systèmes planétaires sont dynamiques et que les planètes

peuvent migrer de leur location après leur naissance.

TPF apportera des informations essentielles sur les distributions de masse et de température dans les disques autour des étoiles jeunes, berceaux de nouvelles planètes. Ces informations vont apporter d'importantes preuves sur les processus physiques de formation qui déterminent si une planète est rocheuse ou gazeuse.

1.4.4 Galaxies

La nouvelle génération d'interféromètres optiques et infra-rouges a maintenant atteint la sensibilité nécessaire pour observer des sources extra-galactiques telles que les noyaux actifs de galaxie (AGN). Il a récemment été rapporté l'acquisition de franges d'interférence sur ces objets au VLTI.

Les AGNs sont parmi les phénomènes les plus énergétiques et mystérieux de l'univers. Dans certaines galaxies, le cœur génère des quantités d'énergie bien supérieures à celles de galaxies ordinaires, de plusieurs ordre de magnitude. Le moteur central est supposé être un trou noir super-massif. Des preuves indirectes ont suggéré que ces trous noirs massifs sont cachés au milieu d'un tore de gaz épais et de poussière. Cependant, à cause de la limitation en résolution angulaire des images pouvant être obtenues avec les télescopes actuels, un tel tore n'a encore jamais été imagé. Le VLTI a permis de résoudre pour la première fois la structure du tore de poussière de l'archétype des AGNs, NGC 1068. Des structures dont la taille est environ 0.03″, soit environ 10 années lumière à la distance de la galaxie, ont été détectées (ESO Press Release 17/03). Quasi-simultanément, une communication informelle, m'informa que l'interféromètre Keck avait mesuré des franges sur une autre source extra-galactique, mais aucun détail relatif à ces mesures n'a été publié à ce jour.

1.5 Ce Travail de Thèse

La contribution de cette thèse est dans le domaine de l'imagerie à haute résolution angulaire au moyen de techniques interférometriques.

Au Chapitre 2 je décris la simulation d'un système d'optique adaptative pour la pupille densifiée. Cette optique adaptative est nécessaire pour permettre d'obtenir des images directes à haute resolution angulaire de sources stellaires avec un système interférométrique à pupille densifiée.

Au Chapitre 3 je décris les premiers tests sur le ciel d'un interféromètre à pupille densifiée. L'interféromètre avait une base maximale de 10 cm et fut réalisé avec un télescope muni d'un masque pupillaire percé de petits trous.

Aux chapitres 4 et 5, dans le cadre des systèmes d'imagerie indirecte, je décris le contrôleur de caméra infrarouge que j'ai réalisé pour l'interféromètre infrarouge IOTA (infrared optical telescope array). Les interféromètres de ce type ont une transmission optique très faible à cause du grand nombre de réflexions et d'atténuations dans le montage optique. Il est donc très important de construire des contrôleurs de caméra très performants capables d'obtenir de très bas bruits de lecture.

Au chapitre 6 je décris un système pour la recherche et le suivi de franges que j'ai realisé pour IOTA. Même si l'optique adaptative nécessaire à l'imagerie directe en mode pupille densifiée n'est pas nécessaire pour l'imagerie indirecte, maintenir les trois bases en cohérence est très important pour la mesure des clôtures de phases. Il est en fait nécessaire de maintenir les trois paquets des franges le plus possible superposés afin d'augmenter le rapport signal sur bruit de la mesure.

Finallement au chapitre 7 je présente les résultats astrophysiques que j'ai obtenus avec des données d'archive acquises avec deux telescopes à IOTA. Ces données ont été utilisées pour la mesure de diamètres angulaires d'étoiles Mira dans les bandes spectrales J, H et K (proche infrarouge).

Chapitre 2

Un Algorithme de Phasage Hierarchique pour un Interféromètre à Plusieurs Éléments

Pedretti E. & Labeyrie A. 1999, paru dans *Astronomy and Astrophysics* **137**, 543

Résumé

Les grands interféromètres à plusieurs ouvertures sont conçus pour obtenir des images instantanées avec une résolution angulaire de quelques milli/micro secondes d'arc, directement au foyer recombiné. Cela requiert d'une part une pupille de sortie densifiée, d'autre part, des faisceaux phasés pour toutes les longueurs d'onde utilisées. Les méthodes d'analyse du front d'onde utilisées pour l'optique adaptative des télescopes monolithiques ne peuvent pas être utilisées pour des ouvertures diluées. C'est pourquoi nous avons développé un algorithme de phasage différent. Il utilise une hiérarchie de triplets d'ouvertures et un critère de finesse d'image. Des simulations numériques sur des objets non-résolus et résolus montrent qu'une seule itération est généralement suffisante. Pour des objets dépendant de la longueur d'onde, le correcte indexage de la position des composantes monochromatique de l'image semble également efficacement réalisable.

Mots clé : Instrumentation : Interféromètres – Méthodes : numériques – Techniques : traitement d'image – Techniques : interférométriques – Télescopes

Introduction

Cet article et les simulations que j'ai réalisées ont été conçus pour démontrer la faisabilité d'un interféromètre à pupille densifiée. Lorsque les faisceaux provenant de télescopes séparés sont recombinés pour obtenir une image directe, il est nécessaire que pour tous les faisceaux, la lumière parcoure la même distance de l'objet au point de recombinaison. Plus précisément, la différence de marche optique entre les différents télescopes doit être inférieure à une petite fraction de la longueur d'onde à laquelle l'observation est menée. Ceci est d'autant plus vrai pour les observations menées au sol, où il faut compenser des changements rapides de chemins optiques introduits par la turbulence de l'atmosphère terrestre. C'est pourquoi nous sommes contraints d'installer sur les interféromètres des systèmes équivalents à des optiques adaptatives qui maintiennent les chemins optiques identiques.

J'ai donc réalisé la simulation numérique d'un nouvel algorithme basé sur une hiérarchie de triplets d'ouvertures comme décrit dans l'article suivant. La simulation est divisée en deux parties. La première partie concerne la simulation d'un système à pupille densifiée où la relation de convolution dans l'image est substituée par une relation de pseudo-convolution (Labeyrie 1996). La seconde présente la simulation du phasage et du cohérençage de faisceaux par l'utilisation de triplets d'ouvertures.

Dans ces simulations, je considère que les détecteurs sont parfaits et ne produisent pas de bruit de détecteurs. Par contre, je prends en compte le bruit de photons.

A hierarchical phasing algorithm for multi–element optical interferometers

Pedretti E. & Labeyrie A. 1999, *Astronomy and Astrophysics* **137**, 543

Abstract

Large multi–aperture interferometers are expected to provide snap–shot images with milli– to nano–arcsecond resolution, directly at the combined focus. This requires a densified exit pupil and phased beams for all the wavelengths used. The wave analysis methods serving for adaptive optics in monolithic telescopes being inadequate for diluted apertures, we have developed a different phasing algorithm. It involves a hierarchy of aperture triplets and uses image sharpness criteria. Numerical simulations on unresolved and resolved objects show that a single iteration is generally sufficient. On wavelength–dependant objects, the proper position indexing of the monochromatic image components appears also efficiently achievable.

Keywords : Instrumentation : Interferometers – Methods : numerical – Techniques : image processing – Techniques : interferometric – Telescopes

2.1 Introduction

Long baseline optical interferometry is still in its infancy, with aperture count currently limited to 3. The feasibility of using numerous apertures, spaced kilometers apart, to obtain high–resolution snapshot images was initially debated (Traub 1986; Beckers 1986). Fizeau interferometry, the only beam–combining scheme then known to provide snap–shot images did not appear usable with highly–diluted apertures. Only recently was a solution found (Labeyrie 1996), in the form of "densified–pupil imaging", a beam–combining scheme which can achieve efficient imaging on compact objects.

With this scheme, ways of using diluted apertures spanning up to 100,000 km are foreseen (Labeyrie 1999). It will require active or adaptive phasing, like in monolithic telescopes.

The closure phase method (Jennison 1958), widely used in the radio interferometry domain and also recently used in the COAST optical interferometer (Baldwin et al. 1996) for observing the binary star Capella, is suitable for phasing diluted arrays but requires individual phase measurements on all the baselines taken into account for the closures. In our case, this would imply a pair wise recombining technique for a number of baselines much larger than the 13 groups of apertures used for our approach to cophasing the array.

We have developed a different algorithm, suggested by one of us (A.L.), and possibly well suited for this type of instrument. We describe the algorithm in section 2.4, results of numerical simulations in section 2.5, and discuss the limitations in section 2.6.

2.2 Simulated Images From a Diluted Array

We considered the case of densified–pupil interferometers (Labeyrie 1996), a new class of instruments where beams are combined like in Michelson's 20– and 50–feet systems, but with more than 2 beams. The densified–pupil concept evades the "golden rule", once thought inescapable, which stated that imaging interferometers had to be Fizeau–like (Dugue et al. 1983; Traub 1986; Beckers 1986). Fizeau–type interferometers having many apertures can produce snapshot images, but not if the aperture is highly diluted since most energy then goes in the numerous side–lobes rather than in the central interference peak. Densifying the exit pupil (Fig. 2.1), by extending to many apertures the kind of "periscopic" arrangement originally used by Michelson, can concentrate the energy in the interference peak, but appeared to destroy the isoplanaticity needed to observe resolved objects.

The solution recently found uses a restricted class of Michelson–type arrangements where :

- the pattern of sub–aperture centres is identical in the entrance and the exit pupils.
- all sub–pupils are of homogeneous size and shape.

It can provide full energy concentration in the combined high–resolution image, but the field and object size are restricted to about $N \times N$ resolved elements, if N is the number of apertures.

If the exit pupil is highly densified, as is necessarily the case in large space instruments such as the proposed Exo–Earth Discoverer (Boccaletti et al. 2000), the Terrestrial Planet Finder (Angel et al. 1997; Woolf 1997) and the Exo–Earth Imager (Labeyrie 1999), then a valid approximation for the monochromatic intensity distribution B(x, y), in the combined focal image was shown to be (Labeyrie 1996) :

$$B_{(x,y)} \approx {\gamma_d}^{-2} A_{(x,y)} \left[O_{(\frac{x}{\gamma_d}, \frac{y}{\gamma_d})} \otimes I_{(x,y)} \right], \tag{2.1}$$

where $O_{(x,y)}$ is the intensity distribution of the object. $I_{(x,y)}$ is the interference function of the interferometer, i.e. the Fourier transform of an array of Dirac peaks located

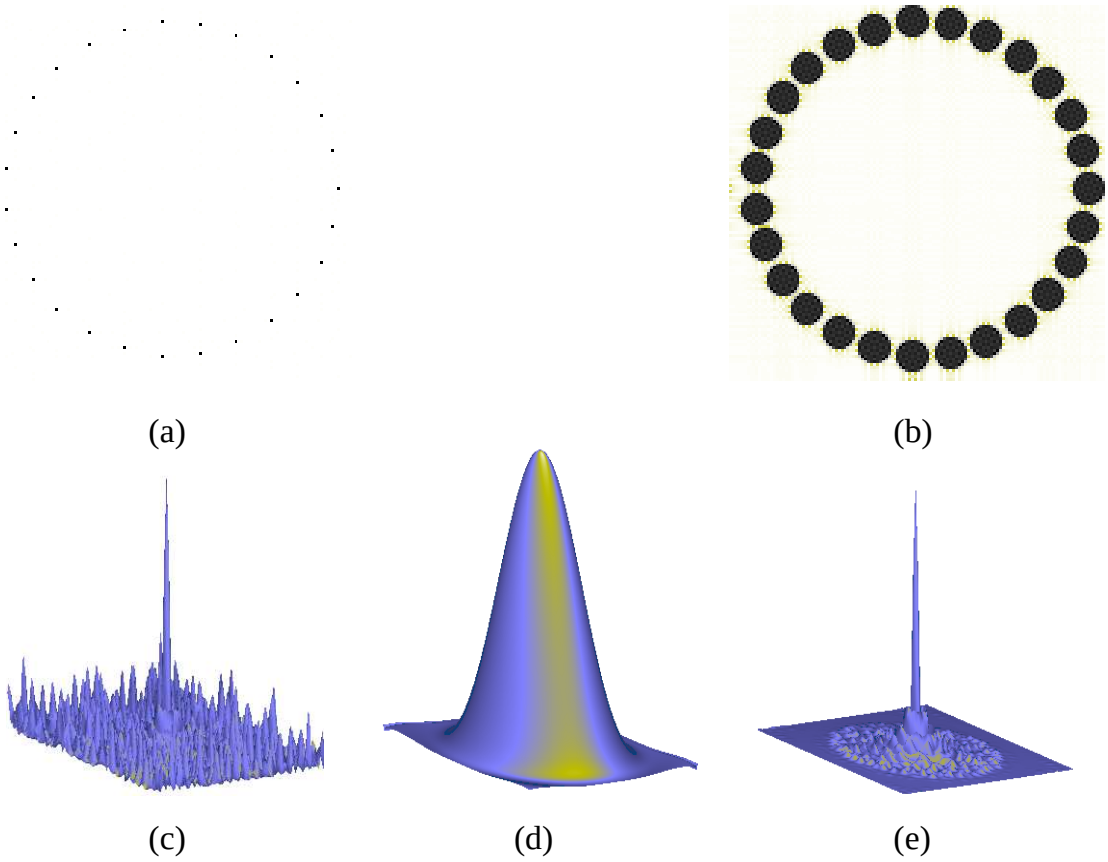

Fig. 2.1.— Image formation with a densified–pupil array. The array's exit pupil is the convolution of an array of Dirac peaks a–, with a sub–pupil. The Fourier transform of the peak array c–, called the interference function, here has a central peak surrounded by 54 lower peaks. The broad multiplicative envelope, called the diffraction function, shown in d– is the Fourier transform of the sub–pupil, made proportionally larger in the exit pupil than in the entrance aperture. The image of a non–resolved star is obtained in e– as the product of the patterns c– and d–. With a resolved star, only the interference function is becoming convolved with the star function if the pupil is highly densified.

at the sub–aperture centres, $A_{(x,y)}$ the diffraction pattern from one sub–aperture and $\otimes$ is the convolution symbol. Finally, x and y are the coordinates in the focal plane. The quantity $\gamma_d = (d_o/D_o)/(d_i/D_i)$ describes the amount of pupil densification, D_i and d_i, being the pupil and sub–pupil sizes at the entrance, while D_o and d_o are the corresponding quantities at the exit pupil.

Eq. 2.1 shows that the interference function $I_{(x,y)}$ (Fig 2.1.c) is convolved with the object's intensity distribution and then multiplied by the wide diffraction pattern of the sub–pupil (Fig. 2.1.d). For the large values of the pupil densification this latter pattern is considered insensitive to object position and simply behaves, where Eq. 2.1 is valid, as a windowing function which multiplies the convolution.

$I_{(x,y)}$ generally has a central peak if the sub apertures are phased, a desirable situation which improves greatly the quality of the snapshot image $B_{(x,y)}$ (without phasing, speckle interferometry can still produce images). In monochromatic light, the phasing is required modulo 2π radians, but reaching the phasing condition at numerous wavelengths simultaneously requires all optical paths to be equal, as is the case for a perfect giant telescope. In our simulation we used 3 wavelengths to reduce the path differences from $10\mu m$ to nearly zero. The example discussed here involves 27 identical apertures, arrayed along a circle, but the algorithm can be extended to any hierarchy of triplets arbitrarily arrayed.

2.3 Phasing a Hierarchy of Triplet Apertures

An early algorithm for adaptive optics, not relying on wavefront continuity, was proposed by Muller & Buffington (1974). It is based on the maximisation of a sharpness function, defined as :

$$S = \int B^2_{(x,y)} dxdy, \tag{2.2}$$

where B is the intensity of the image at a point (x, y).

The mirror actuators are adjusted each in turn, with repeated iterations performed faster than the seeing lifetime, to maximise the sharpness function. The convergence however tends to be trapped in secondary maxima. To overcome this problem, (Ribak et al. 1990) used simulated annealing : noise is added to the actuator signals and gradually reduced until the system falls in a state of minimum energy, reached when the sharpness function is maximised.

Hamaker et al. (1977) have later remarked that, according to Parseval's theorem, maximising the sharpness function is equivalent to maximising the integrated square modulus in the image's Fourier transform, which is the pupil's auto–correlation function multiplied by the object's Fourier transform. The maximum occurs for uniform pupil phases. However, if the aperture is diluted, the intensity of the autocorrelation peaks remains invariant if they do not overlap. This indicates that the sharpness approach cannot work if the exit pupil aperture is highly diluted, as would be the case for long–baseline Fizeau interferometers. The densified exit pupils considered here can be made to meet the peak overlap requirement.

We have tried to improve the convergence and to avoid the simulated annealing, by using a hierarchy of aperture triplets. The 27–aperture interferometer is initially divided in 9 separate interferometers, each combining images from 3 adjacent apertures, then re–arranged as 3 separate interferometers having 9 apertures each and finally re–arranged as a single interferometer having 27 apertures. If observations are performed from Earth the steps of re–arrangements are cycled at high speed, within the life–time of seeing, by tilting elements of the active mirror support to "explode" the image into separated triplet components. More delicate tip–tilt and piston adjustments of the same elements provide the phase adjustments, as described in Fig. 2.2.

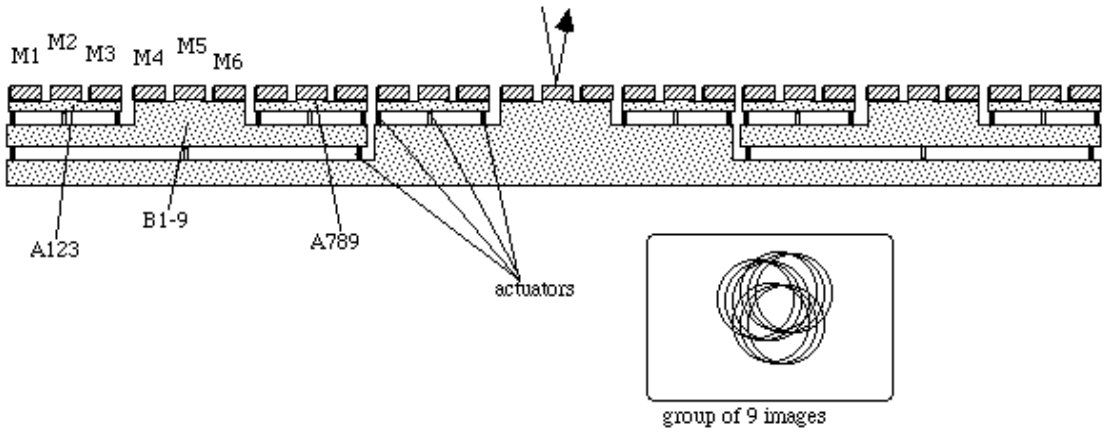

Fig. 2.2.— Hierarchical arrangement of actuators carrying 27 mirrors for phasing according to the triplet algorithm. For clarity, the system is sketched as a line array, and without the tip–tilt correctors carrying each elementary mirror. Each triplet of mirrors is carried by a plate, itself carried by3 actuators, arranged as a triangle to provide piston and tip–tilt corrections. 3 such plates, carrying a total of 9 mirrors, are themselves carried by a larger plate, also carried by 3 actuators. A group of 9 mirrors can be phased by adjusting both lateral triangle plates, in terms of tip–tilt and of piston. The criterion used for this 6–parameter adjustment is the sharpness value. If the star is unresolved, centering the honeycomb fringe patterns from each mirror triplet, and the finer honeycomb from the triplet of triplets is also suitable. Once the 3 groups of 9 mirrors are independently phased, the global phasing of 27 mirrors can be obtained similarly by applying tip–tilt and piston corrections to both lateral plates carrying 9 mirrors. Finally, the diffraction functions from each elementary mirror may be centered with their tip–tilt actuators (not shown). Phasing is achieved modulo 2π, but the use of several wavelengths can remove the ambiguity and provide zero path difference.

The monochromatic interference pattern from 3 sub–apertures is generally a honeycomb–like interference function, multiplied by the diffraction function. Adding 3 such patterns from adjacent groups creates a finer honeycomb pattern within the coarse one. The triplet grouping can be pursued at higher levels of the hierarchy to include 27, 81, 243, etc. apertures. The closest apertures are grouped first to benefit from the fact that the object is less resolved.

For a non–resolved star, phasing is directly achievable by centering a cell of the honeycomb pattern appearing at each level of triplet formation. This requires adjusting 2 phases, those of 2 among the 3 groups of apertures at every step of the routine (Fig. 2.3). In monochromatic light and for 3 groups of apertures, the honeycomb pattern can be centered by extracting the phase values in the 6 peaks of its Fourier transform. In polychromatic light, 3–dimensional Fourier transforms of the x, y, λ data cubes provided by the spectro–imaging camera can provide similar

information with full removal of the modulo 2π phase ambiguity. This algorithm has not been tested yet, but a 2–aperture analog is routinely used at the "Grand Interferometre a 2 Telescopes" (GI2T) (Morel & Koechlin 1998) for fringe acquisition.

More simply, the central white cell appearing in a honeycomb pattern amidst the coloured lateral cells can also be identified, even with a broad–band monochrome camera, from its higher contrast. Centering all the white cells from the various triplet groups onto a common fiducial mark corrects directly the optical path errors. On resolved objects, such honeycomb centering should not generally succeed since de–centered honeycomb components can be present. Indeed, imaging an object through a diluted triplet aperture causes a convolution with the honeycomb–like spread function. If the object is itself a honeycomb–like grid pattern matching this function, then the convolution preserves the image contrast, a situation which may be qualified as "honeycomb resonance". With 3 different triplets now forming a single aperture, 3 different grid components of the object add their images, but they do not generally have a common centering. Hence the need for another criterion, sharpness for example, to adjust the tip–tilt of 2 pupil triplets before adjusting their global piston. Six parameters should therefore be adjusted at each level in the hierarchical procedure.

When calculating the sharpness integral, the diffraction envelope of the sub–images causes unwanted biases, which tend to center the brighter zones. The bias can be avoided by "flattening" the diffraction peak : each recorded sub–image must be first divided by the known diffraction function, within the peak area.

Somewhat surprisingly, our simulations (Fig. 2.4) on resolved objects worked well without these precautions, using a simplified version of the routine : only piston adjustments were made at each level, and no flattening of the diffraction envelope was carried out. It is however likely that some object shapes require the complete routine. Also, no trapping in secondary maxima of the sharpness function was observed, but the reasons are unclear. Further investigations are desirable in these respects.

A single camera can receive all partial images and the fully combined image, using either temporal or spatial separations as shown in Fig. 2.5. Rather than using the actuators for exploding the image into the various groups at a fast cycling rate, beam–splitters can provide a parallel display of these triplet, ninetuplet, etc. groups (Labeyrie 1999). Mapping the x, y, λ information is efficiently achievable with a spectro–imaging attachment such as the combination of a grism and a micro–lens array developed by Bacon, and co–workers (Bacon et al. 1995) at the Observatoire de Marseille.

2.4 Phasing And Path Difference Equalisation

The sharpness S was maximised by exploiting its sine response to phase variations (Muller & Buffington 1974). In polychromatic light, the algorithm is applied separately to the different wavelength components in the x, y, λ data cube.

The set of pupil phases is thus obtainable at each wavelength, and the modulo 2π ambiguity can be removed to find the true optical path deviations and correct

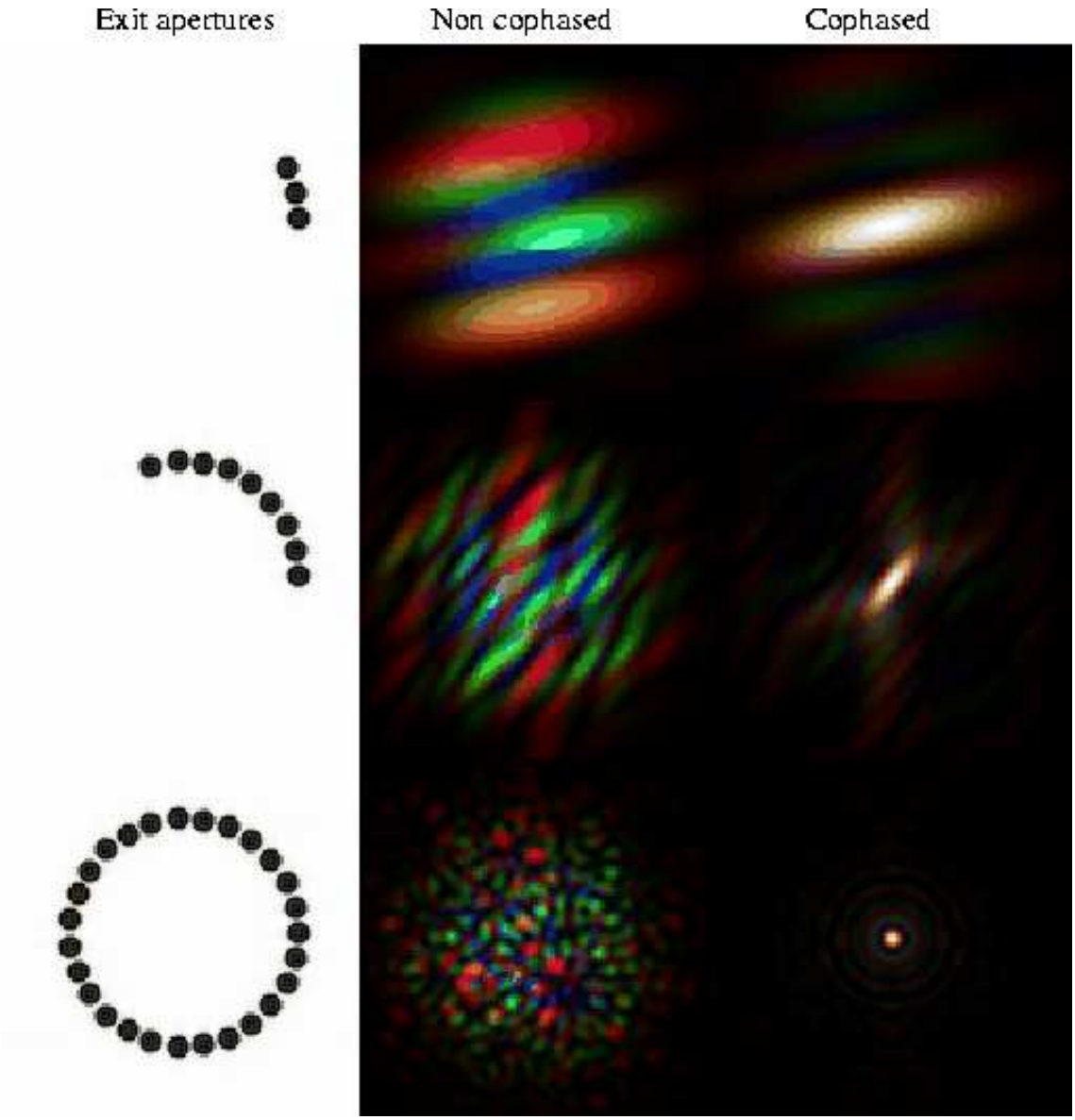

Fig. 2.3.— Steps of phasing sequence for 27 apertures, using 3 wavelengths on a point source. Top row : 3 elements of the entrance aperture (top–left) and their interference pattern obtained before (middle) and after (right) correcting optical path errors. Middle row : combining 3 such groups of apertures provides finer fringes, which can be centered by adjusting the global phases of 2 groups. Bottom row : one more similar step corrects the optical path errors among the 27 apertures, thus producing a narrow interference peak. With a continuous spectrum rather than just 3 wavelengths, the speckles of the central bottom image would be appreciably smoothed.

them. Only in such conditions of ideal interferometer adjustment can one obtain white images directly at the combined focus, with perfect colour registration and

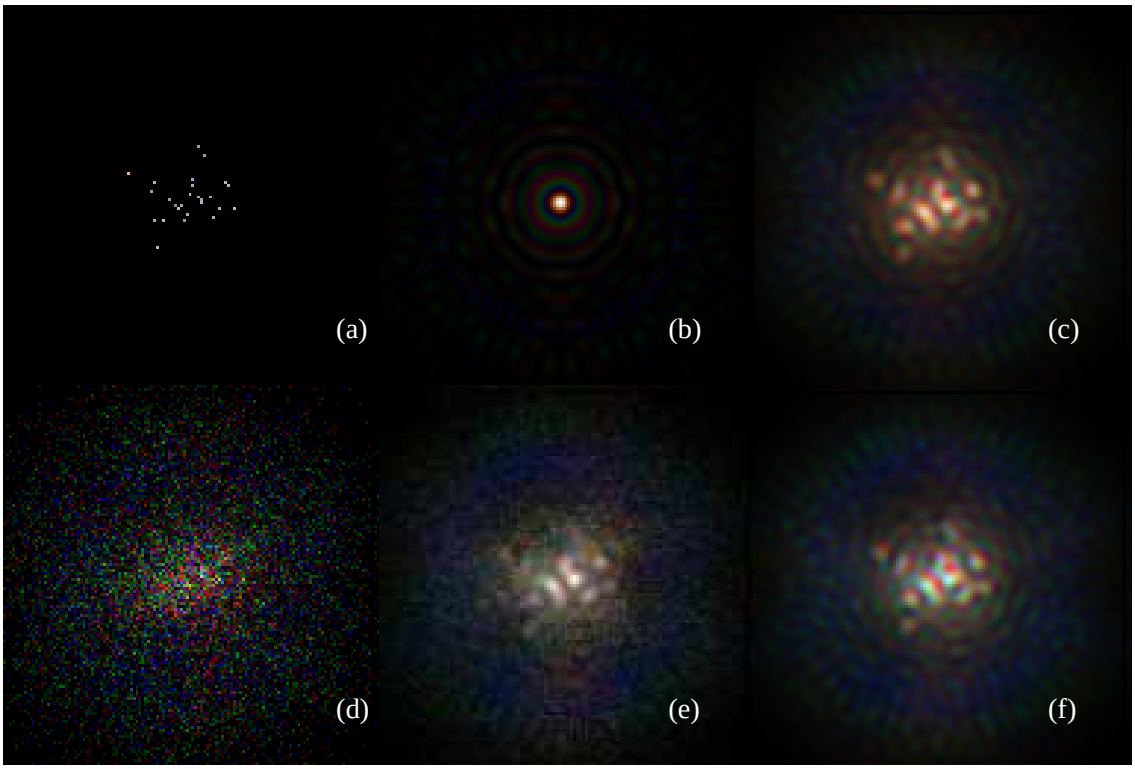

Fig. 2.4.— Effect of photon noise on the phasing algorithm ; a– simulated star cluster having 27 stars of different colour ; b– interference function ; c– theoretical image with zero path difference. The images were obtained with a single iteration of the phasing algorithm ; d– image obtained with 2200 total photons obtained from 3 wavelengths, Strehl ratio = 0.3 ; e– case of 29,000 photons, Strehl ratio = 0.7 ; f– case of $18 \cdot 10^6$ photons, Strehl ratio = 0.8.

including any spectral components too faint for being separately imageable with the monochromatic algorithm. On resolved and colour–dependant objects, ensuring zero optical differences is made more difficult by the a priori unknown position indexing among the monochromatic images. One needs to solve for the value of integer k in Eq. 2.3

$$\delta = (k + \epsilon)\lambda + (\alpha x + \beta y), \tag{2.3}$$

where $\epsilon = \phi/2\pi$ and λ is the wavelength. The term $\alpha x + \beta y$, where α, β are the sub–pupil's position coordinates, is the path difference generated by the wavelength–dependant image position error x, y. For a non–resolved star the shift x, y is identical at every wavelength and the second term of Eq. 2.3 therefore vanishes. One may then apply the classical fractional excess algorithm, used in the field of interferometric metrology since Michelson's measurement of the standard metre, to calculate the optical path differences. It consists in calculating, at every wavelength, δ values corresponding to all possible values of the unknown integer k. A δ value re–appearing at all wavelengths is the correct value of the optical path error for the sub–pupil

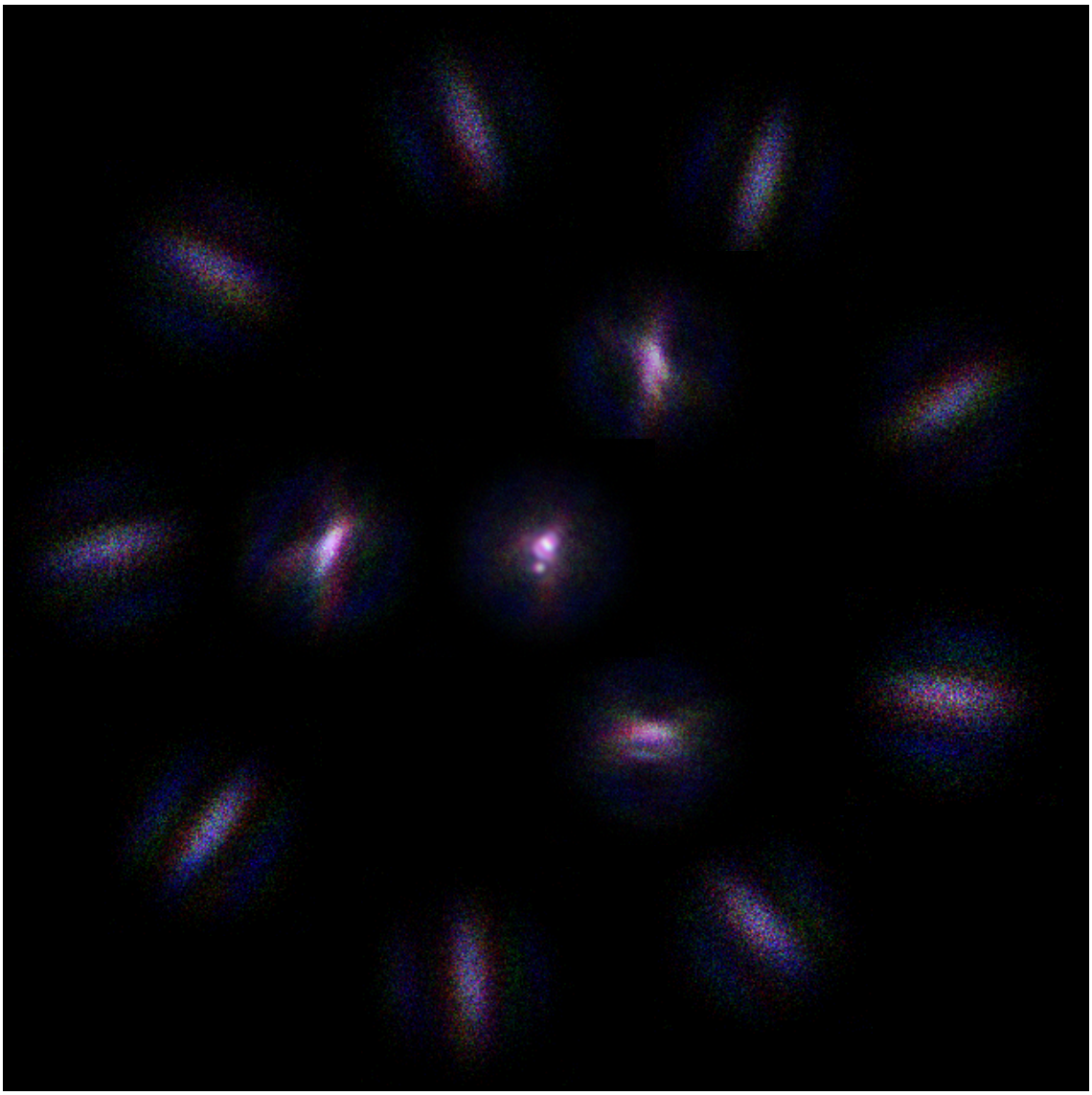

Fig. 2.5.— Picture of partial and fully combined images with 9 groups of 3 apertures (external ring), 3 groups of 9 (intermediate ring), 1 group of 27 (centre), and the corresponding diffraction patterns, as they would appear when formatted on a single camera. The object used in the simulation is the galaxy M51. The simulation was performed with photon noise. In the final image a Strehl ratio of 0.84 was obtained with 250,000 photons.

considered. We have used this type of method, rather than the 3–dimensional Fourier transform, and verified the expected performance. Although not expected to work on resolved, colour dependant, objects, it also succeeded with such objects in most cases (Fig. 2.4 & 2.5).

It appears possible to extend the method for dealing also with the shift term

in Eq. 2.3, as required for full adjustment on resolved, colour–dependant, sources. Because the x, y image shift is identical for all sub–pupils, at a given wavelength, the corresponding equations are coupled and appear solvable if enough wavelengths are used. Different values of x, y and again the integer k can be inserted in the series of equations obtained at all wavelengths. The candidate values of δ thus obtained may be organised as a 2–dimensional array of cubes, each being derived from a pair of vectors x_λ, y_λ, specifying a trial set of position shifts. The cube axes are divided in units of k, λ and the sub–pupil number. The particular cube providing the correct set of optical path errors is identified from the presence of numbers repeating in all lines within each of its k, λ planes.

No attempt has yet been made to apply this method, although it may also solve classical problems of source position indexing in radio interferometry.

2.5 Results

Fig. 2.4 shows one of the objects used in the simulation, a coloured cluster of 27 stars. The object's intensity distribution was convolved with the interference function of the interferometer and then multiplied with the diffraction function, both functions being converted to intensities. The optical path differences were found, using 3 wavelengths, with initial wavefront errors of the order of $10\mu m$. The Strehl ratio, i.e. the peak intensity in the image of a point source, relative to the case of perfect phasing, gives an idea of the phasing performance. It reaches 30% with 2200 photons detected during the phasing cycle and 80% with $18 \cdot 10^6$ photons.

The successive frames of Fig. 2.6 from left to right depict changes in the full combined image during the phasing steps for the same object.

The field and object size restriction with densified–pupil imaging often implies that the object is unresolved or little resolved by the smallest baselines. Although the simplified routines which we used in the simulations did not include all the features which appeared necessary, the resulting imaging quality approached the theoretical limits on the source shapes used, typical of resolved stellar and galactic objects. Even better results should therefore be expected with future refined versions of the algorithm.

2.6 Limiting Magnitude

The limiting magnitude estimates given by the early proponents of the sharpness criterion (Muller & Buffington 1974) were lower than those obtained in monolithic adaptive telescopes. This can be attributed to the intrinsic advantage of exploiting the wavefront continuity with analyser systems such as Shack–Hartmann (Shack & Platt 1971) or curvature sensing (Roddier & Roddier 1991). Long–baseline interferometers obviously cannot benefit from this advantage, but the triplet algorithm appears to improve somewhat the limiting magnitude with respect to the original sharpness

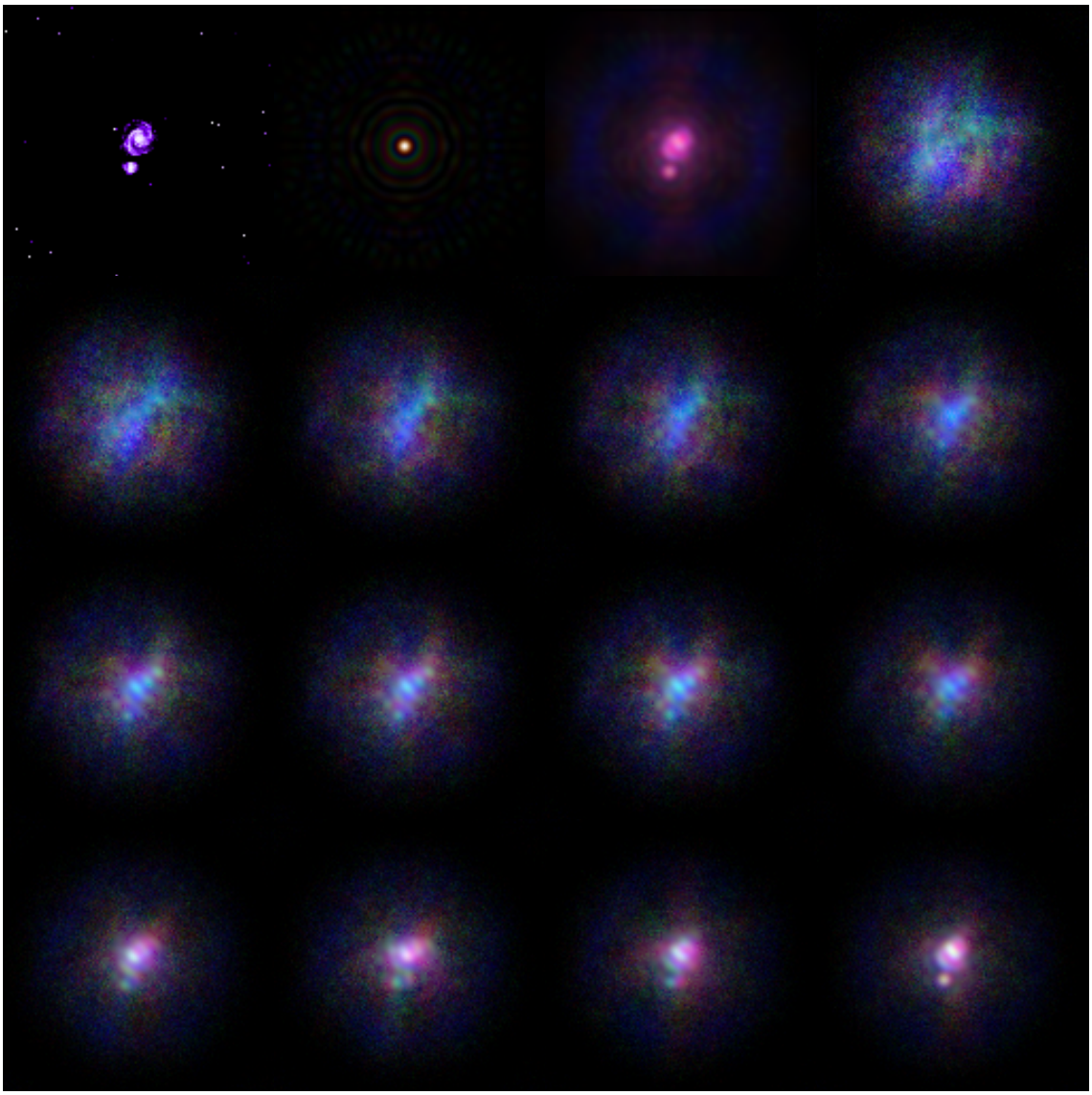

Fig. 2.6.— Simulated phasing sequence on galaxy M51, in presence of photon noise. The galaxy is shown in the top–left frame, followed by the interference function of the interferometer and the convolution of the object with the interference function. The object is unresolved by the smallest baselines, its components have different colours and phasing is achieved with 250,000 photons. Successive frames depict changes in the full combined image during the phasing steps. The last frame, at bottom right, is the final step of the phasing process, where a Strehl ratio of 0.80 was achieved.

algorithm.

Photon noise in the recorded image generates a speckled halo in its Fourier transform. The halo's addition to the correlation peaks affects their phase and intensity. With a photon–counting camera as the image detector, the Poisson statistics of the

detected photons is preserved. If p photons are detected during a short exposure, the image's Fourier transform has a central peak having p times the average intensity of the halo. As in the high–level pattern, the intensity of the surrounding correlation peaks relative to the central peak is N^{-2} and further attenuated if the star is resolved. To have correlation peaks emerging from the halo $p > N^2$ photons are thus needed, as required for reasonably accurate determination of the phases.

If the star is unresolved, the aperture phases can be calculated directly from the phases of the correlation peaks. Simulations with a simple iterative routine provided a fast convergence (2 or 3 iterations) and verified the $p > N^2$ condition. This was achieved by subtracting from the phase of each aperture the average phase from the N correlation peaks related to the aperture, and iterating after recalculating the image's Fourier transform. In polychromatic light, the fractional excess method can be applied to the phases obtained in each correlation peak for deriving the optical path in each peak, and the routine then provides the optical paths of the apertures.

The 6–parameter optimisation of sharpness for each triplet requires 2 exposures for adjusting each parameter and thus 12 exposures. This requires $12 \times 9^2 = 972$ detected photons from 9 apertures. Similarly, the full aperture stage requires 12×27^2 photons, hence a total of about $p = 14000$ within the life–time of seeing. In practice fewer photons, about 800, proved enough to obtain rather good images in our simulations of non–resolved objects, but resolved objects are less favorable. This number also matches the $p > N^2$ condition mentioned above for direct phase retrieval on un–resolved stars. On a resolved object such as shown in Fig. 2.7.d, 130,000 photons were needed to obtain a Strehl ratio of 0.96 with a single wavelength.

With p photons received from the N–element aperture in time τ, corresponding to the life–time of seeing, the incident photon flux per square centimeter B is : $B = 4p/(\pi d^2 \tau N \eta)$ and the stellar magnitude $m_v = 2.5 \log(734\ \delta\lambda/B)$, d being the size of the sub–aperture elements in centimeters, η the overall quantum efficiency, and $\delta\lambda$ the bandwidth in Angström units. The limiting magnitude found with 27 apertures of 10cm, 0.02s seeing lifetime, $\eta = 0.1$ and 300nm optical bandwidth is 5.4 with $p = 14000$ photons and 8.3 with $p = 800$ photons, somewhat higher than the value 4.3 found by Muller et al. in identical conditions.

Large sub–apertures with uniform phase, obtainable with a number of large ground–based telescopes equipped with adaptive optics and a laser star, can push the limiting magnitude for inter–aperture phasing towards $m_v = 20$, assuming 10m telescopes. The intra–aperture adaptive optics increases the lifetime of the wavefront's phase, owing to its averaging effect, and this contributes to the magnitude gain.

In space, much longer lifetimes can be expected, given the excellent predictability and measurability of telescope motions in the quiet micro–gravity environment. The availability of reference stars also favors efficient phasing on very faint objects. As discussed elsewhere (Labeyrie 1999), the extreme case of 100,000 km optical baselines dedicated to observations of neutron stars appears manageable in terms of phasing. A more detailed analysis of limiting magnitudes with various array configurations, object shapes and phasing methods is desirable.

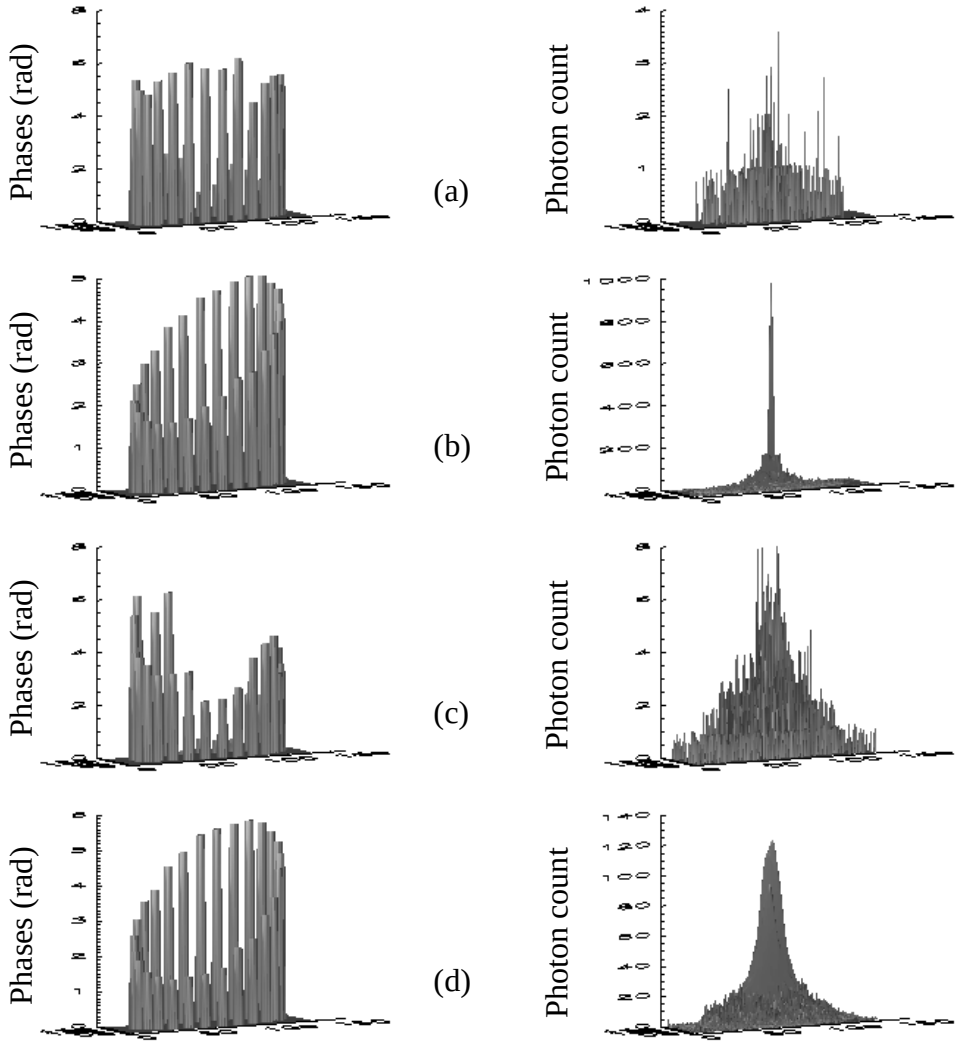

Fig. 2.7.— Corrected phases (left) and images (right) obtained with an unresolved monochromatic source (frames a & b) and with the object shown in Fig 2.6, the galaxy M51(frames c & d). Images are obtained after 1 iteration of the phasing algorithm for 500 a–, 100,000, b–, 5000 c– and 130,000 d– photon events detected during the phasing sequence. The corresponding Strehl ratios are 0.48, 0.97, 0.38, 0.96. The residual slope of the phase pattern affects only the image position.

2.7 Conclusions

Our simulations of co–phasing algorithms, using a triplet hierarchy, show convergence for both the cases of unresolved and resolved objects. With 3 different wavelengths, zero path difference has been achieved with initial errors of the order of $10\mu m$. Simulations with limited photon rates have shown that resolved images of bright stars are in principle obtainable with apertures of 10cm, using adaptive phasing at visible

wavelengths. Arrays of large adaptive telescopes should extend the limiting magnitudes towards $m_v = 20$ on Earth and $m_v = 35$ in space. Possible refinements of these algorithms remain to be explored, but the simulations demonstrate the effectiveness of the triplet algorithm, used with image sharpness criteria, for phasing a multi–aperture array. This establishes the practical feasibility of obtaining high–resolution snapshot images on compact objects, with future interferometers spanning up to thousands of kilometers. In particular, it supports current projects towards obtaining resolved images of exo–planets with sufficient quality to see clouds, continents and vegetated areas (Boccaletti et al. 2000).

Acknowledgements

One of us (E.P.) would like to express his gratitude to Alastair Macgregor for his supervision in the early stages of this project. He would also like to thank Neal Jackson for his supervision and fruitful discussions during the continuation of this project at Jodrell Bank.

We are very much indebted to Laurent Koechlin and Luc Arnold for their critical reading of the manuscript and useful suggestions. This work started at the University of Northumbria as a final year project and continued at the Observatoire of Haute Provence and NRAL, Jodrell Bank.

Chapitre 3

Premières Images Sur le Ciel d'Un Hyper Télescope.

Pedretti, E., Labeyrie, A., Arnold, L., Thureau, N., Lardiere, O., Boccaletti, A., & Riaud, P. 2000, paru dans *Astronomy and Astrophysics*, **147**, 285

Résumé

Nous présentons des images obtenues avec un "interféromètre imageur à pupille densifiée" miniature, également appelé hyper-télescope. La formation de telles images viole l'une des règles de d'or de l'interférométrie qui semble interdire l'utilisation d'assemblages interférométriques différents d'un interféromètre de Fizeau. Ce type d'arrangement produit des images non exploitables dès que l'espacement des sous-ouvertures devient bien plus grand que leur diamètre, du fait de la diffraction produite par les sous-ouvertures. L'arrangement interférométrique de l'hyper-télescope résout ce problème, ce qui permet d'envisager la réalisation d'interféromètres imageurs spatiaux à bases kilométriques. Avec cette expérience, nous obtenons un gain en intensité de $24 \pm 3\times$, lorsque l'interféromètre à pupille densifiée est comparé à un arrangement de type Fizeau. Nous présentons également des images de l'étoile double α Gem obtenues avec cet instrument miniature. Ces premiers résultats confirment la possibilité de former des images directes à haute résolution angulaire et très contrastées, au foyer recombiné d'un grand interféromètre, si un nombre suffisant de sous-ouvertures est utilisé.

Mots clé : Interféromètre –images d'étoiles doubles – images en laboratoire –densification de pupille

Introduction

Après les travaux théoriques de Labeyrie (1996), il n'existait que des simulations numériques pour prouver que des systèmes d'imagerie directe basés sur le principe de la pupille densifiée pouvaient effectivement former des images.

Les suggestions de mon directeur de thèse Antoine Labeyrie d'essayer d'obtenir des images en laboratoire m'amenèrent à construire un système optique dédié à cette expérience. Les premiers résultats en laboratoire furent très convaincants, et je décidais que l'expérience était faisable sur le ciel.

J'ai donc construit un interféromètre de taille réduite, tout le système ne faisait pas plus d'un mètre de long, que j'ai d'abord testé en laboratoire avant de l'installer sur une des tables équatoriales de l'Observatoire de Haute Provence pour des essais sur le ciel.

L'interféromètre fut construit en utilisant un télescope refracteur de 10 cm et un masque percé de très petits trous, superposé à l'ouverture du télescope. La taille des trous fut choisie pour permettre de simuler un interféromètre très dilué. Pour créer la densification de pupille, j'ai utilisé un réseau de micro-lentilles, comme décrit dans l'article suivant.

Ce prototype a été entièment construit en utilisant le materiel optique disponnible au laboratoire d'optique de l'Observatoire de Haute Provence, afin d'en limiter le coût. Les réseaux de micro-lentilles ont été construits par Antoine Labeyrie, par moulage d'un réseau de micro-lentilles utilisé pour l'optique adaptative. La construction de l'interféromètre et les tests en laboratoire me prirent environ une semaine et furent très encourageants.

Pour les test en laboratoire, j'ai d'abord simulé des objets simples et complexes en lumière laser (En utilisant un masque en aluminium, percé d'un ou de plusieurs trous, illuminé par la source laser). La qualité optique des micro-lentilles s'avéra être suffisante pour que je puisse également utiliser des objets en lumière blanche. Après ces derniers tests en lumière blanche, je décidais de poursuivre les tests sur le ciel.

L'instrument fut installé sur une table équatoriale à l'Observatoire de Haute Provence. J'ai utilisé un CCD pour l'acquisition des images ainsi qu'une lunette de 15 cm pour le guidage que j'ai dû effectuer manuellement. Une semaine d'observation m'a permis d'obtenir les images présentées dans cette publication.

First images on the sky from a hyper telescope

Pedretti, E., Labeyrie, A., Arnold, L., Thureau, N., Lardiere, O., Boccaletti, A., & Riaud, P. 2000, *Astronomy and Astrophysics*, **147**, 285

Abstract

We show star images obtained with a miniature "densified pupil imaging interferometer" also called a hyper-telescope. The formation of such images violates a "golden rule of imaging interferometers" which appeared to forbid the use of interferometric arrangements differing from a Fizeau interferometer. These produce useless images when the sub-apertures spacing is much wider than their size, owing to diffraction through the sub-apertures. The hyper-telescope arrangement solves these problems opening the way towards multi-kilometer imaging arrays in space. We experimentally obtain an intensity gain of $24 \pm 3\times$ when a densified-pupil interferometer is compared to an equivalent Fizeau-type interferometer and show images of the double star α Gem. The initial results presented confirm the possibility of directly obtaining high resolution and high dynamic range images in the recombined focal plane of a large interferometer if enough elements are used.

keywords : Interferometers –double star images– laboratory images– pupil densification

3.1 Introduction

The possibility of obtaining direct usable images at the combined focus of a diluted interferometric array was long overlooked. Theoretical work on densified pupil interferometry (Labeyrie 1996, 1998), numerical simulations of its imaging properties (Boccaletti et al. 2000) and a new algorithm for co-phasing a diluted array of several apertures (Pedretti & Labeyrie 1999; Pedretti 1999) now open a new evolutionary track towards large optical arrays in space and on ground.

Fizeau optical arrays, the equivalent of a telescope carrying a multi-hole aperture mask, have imaging properties similar to telescopes. If Rayleigh's criterion is

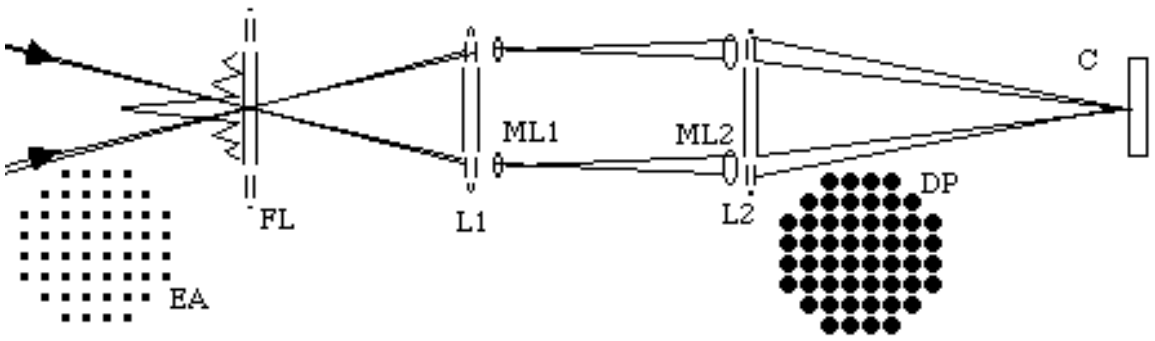

Fig. 3.1.— Pupil densification with micro lenses. The converging beams coming from widely separated sub-apertures (EA) are collimated by lens L1. An image of the entrance aperture is formed, by field lens FL, on the micro-lenses array ML1 having a shorter focal length than the second micro-lens array ML2 located downstream. The focal length ratio of ML2 and ML1 is the pupil densification factor. With suitable phasing adjustments L2 forms a directly exploitable image on the detector C (©PASP).

met, there is a peaked spread function which becomes convolved with features of the observed object. Field is infinite in principle, although limited by telescope aberrations. If the holes in the mask are much smaller than their spacing however, the spread function has a vast halo of diffracted light surrounding its central interference peak. This removes most energy[1] from the peak and creates a useless continuous level in the image. The ensuing image degradation would become disastrous in the giant systems, spreading across kilometers, considered for space interferometry with metre-sized mirrors as aperture elements

Michelson (Michelson & Pease 1921b), in his 20-feet beam, avoided the halo problem by densifying the exit pupil with his four-mirror periscopic arrangement, i.e, giving it a higher sub-pupil size/spacing ratio than in the entrance aperture. This caused the spread function to lose its field invariance : fringes were moving across the diffractive halo if a point source moved. The convolution thus no longer applied. Extended versions of Michelson's beam, using many apertures instead of two, were considered since the 1970's, but the loss of the convolution relation appeared to make them incapable of forming direct images (Labeyrie 1985; Beckers 1986). The point was formalized into a "golden rule of imaging interferometry" (Traub 1986).

Only much later did it appear that the rule can be evaded (Labeyrie 1996), with considerable benefit in terms of future applications. It was shown that a densified pupil such as Michelson's arrangement, but incorporating many elements, can provide direct images if the sub-pupil centres are preserved in terms of their relative locations. The

[1]If a noiseless detector was used and the detector had infinite collecting area, in order to sample all the side peaks, there would be no advantage in densifying the pupil.

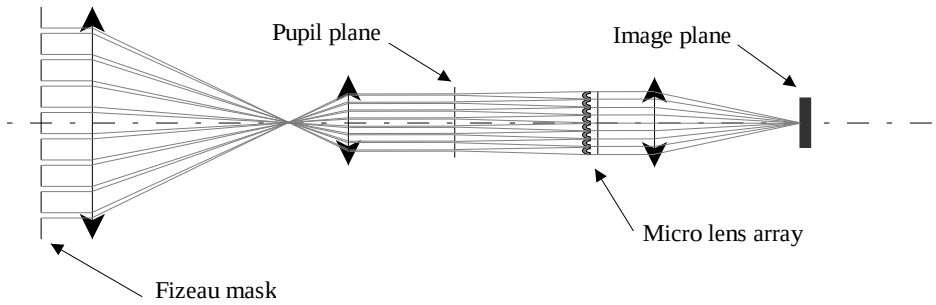

Fig. 3.2.— Miniature hyper-telescope. A Fizeau mask is placed in front of an afocal diffracting telescope. Its image in the exit pupil has narrow sub-pupils which diffract light so that facing elements of the micro-lens array located downstream are each filled by the corresponding diffracted lobe. The pupil-array distance matches the focal distance of the micro-lenses in the array, so that the diverging diffracted beams are approximately re-collimated, thus achieving the desired pupil densification.

image formation may then be described as a "pseudo-convolution" (Labeyrie 1996), where two functions :

- a field-invariant "interference function", which is the Fourier transform of the sub-pupil centres array,
- a broad "diffraction function" which is the Fourier transform of a single sub-pupil,

move at different speed when a point source moves away from the central axis of the instrument. The interference function moves faster than the diffraction function, the speed depending on the densification factor. If the densification factor is large then the movement of the diffraction function with respect to the interference function, becomes negligible[2] .

The diffractive envelope can then be considered a static windowing function, limiting the angular span of the interference function. Inside the envelope, an ordinary convolution of the object with the interference function, takes place .

Systems other than the Michelson beam can be used to densify the exit pupil. Labeyrie proposed the system shown in Fig. 3.1 (Labeyrie 1998) which utilises 2 micro lens arrays to re-image the exit pupils as nearly contiguous wavefront segments.

Here we show the first images obtained on the double star α Gem from a miniature hyper-telescope proving that snapshot, high dynamic range images are obtainable from a Michelson type array.

[2]If the densification factor is one, the two functions move at the same speed and the pseudoconvolution becomes a normal convolution. This is the case of the Fizeau interferometer.

3.2 Experimental Setup

Following the theoretical work which established the feasibility and imaging properties of hyper-telescopes, verifications were first made through computer simulations, followed by a laboratory system and a miniature hyper-telescope tested on the sky.

The latter instrument consists of a $100\,mm$ afocal refracting telescope the aperture of which is masked with a square array of 8×8 holes of $0.8\,mm$, regularly spaced by $s = 8\,mm$. An eyepiece produces an exit pupil image 8 times smaller thus containing $0.1\,mm$ sub-pupils spaced $1\,mm$ apart. The densification is achieved with an array of micro-lenses of similar pitch located $100\,mm$ downstream where the beams from each sub-pupil are spread out by diffraction in such a way that their central lobe fills the facing micro-lens in the array. These lenses having $100\,mm$ focal length provide parallel and nearly adjacent collimated beams expanded from $0.1\,mm$ to $1\,mm$, achieving a densification factor of about $10\times$. At the focus of a lens located immediately downstream, the central interference peak obtained is intensified with respect to the equivalent but non densified Fizeau array. This micro-lens array, obtained commercially, was modified by immersing its active face in silicon elastomer, a medium having a slightly lower refractive index than the lenses' material, in order to lower the optical path difference (from now on OPD) caused by unequal thickness of the micro-lenses. With its aperture diameter of $D = 56\,mm$ this miniature array has $\lambda/D = 2.6''$ FWHM angular resolution ($1.8''$ in the diagonal direction) and a usable interferometric field of view of $\lambda/s = 18''$ for a wavelength $\lambda = 700\,nm$ (the centre band for the detector used). Larger arrays would require adaptive optics unless used in speckle interferometry mode. We recorded the images in the focal plane of the interferometer array using a commercial Peltier cooled CCD, camera with $9\,\mu m$ pixel size.

3.3 Laboratory Results

The interferometer was aligned and tested in the laboratory with an artificial star using a laser and a quartz-iodine bulb for white light. After the alignment was completed the imaging capabilities of the interferometric array were tested by replacing the pin hole placed in front of the white source with a multi-hole mask simulating a multiple star. Fig. 3.3 (left) shows a simulated triple system and a cluster of 6 objects (right).

Owing to the unequal thickness of micro-lenses in the array, used initially without immersion, the images obtained at this stage were not correctly phased and exhibited a speckle pattern rather than the expected interference peak. As expected, the speckle pattern was observed to become double when observing a binary artificial star, thus confirming that large hyper-telescopes will be usable for speckle interferometry when not phased adaptively.

In such large hyper-telescopes adaptive piston phasing will however be desirable,

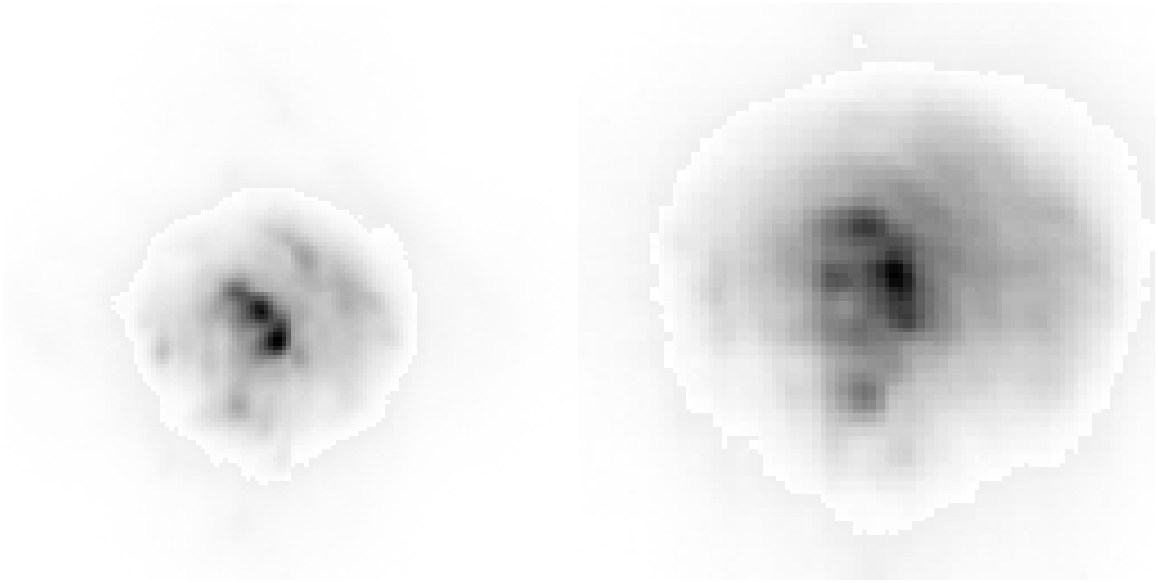

Fig. 3.3.— Laboratory images of multiple artificial stars obtained with the hyper-telescope. Several pin-holes, located very close to a quartz-iodine light bulb simulated a triple (left) and a sextuple(right) star. Both snapshot images were directly recorded with a CCD camera without de-convolution or image enhancement.

in addition to adaptive optics within the sub-apertures. We recall that speckle interferometry does not have an equally good imaging performance for complex objects.

The first micro-lens array can be removed if the sub-pupil size is small enough that diffraction suffices to fill the facing micro-lenses of the second array. This also facilitates somewhat the phasing and makes the alignment easier at the cost of an increased difficulty in controlling the size of the diffraction lobe on the micro lenses. We discuss this effect in Sect. 3.5

3.4 Sky Results

The miniature hyper telescope was tested on the sky (Fig. 3.4**).** This image was obtained on the star Capella (a close binary which is completely unresolved here) by taking two separate exposures of $100\,s$ in the Fizeau and densified-pupil mode of the hyper-telescope. It is of interest to calculate the intensification achieved in the densified-pupil case comparing the 2 images of Fig. 3.4. We start off calculating the theoretical intensity gain, in the central peak, for the 2 instrumental configurations. For an unresolved star the photon count in the central peak is $f = F_s(d_0/D_0)^2$, where F_s is the photon count from a single, unresolved star, d_0 the output sub–pupil diameter and D_0 the output pupil diameter (Labeyrie 1996). In the case of our interferometer the value of d_0/D_0 is 1/70 with the micro-lenses removed (Fizeau) and 1/7 with

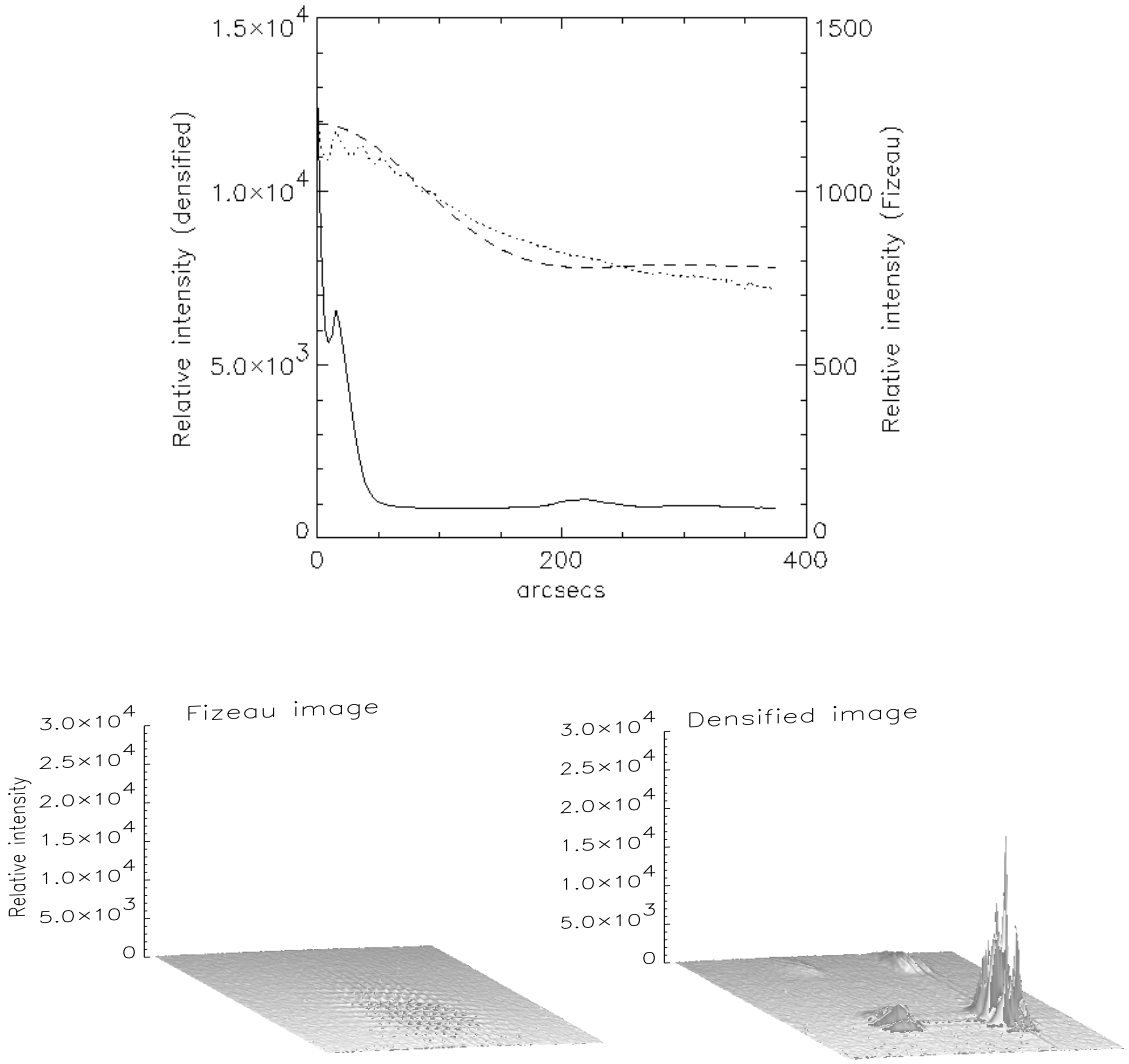

Fig. 3.4.— Fizeau (bottom-left) and densified (bottom-right) surface plots of the star Capella. The top plot is a angularly averaged intensity profile from the bottom plots. The dashed line represents the intensity profile for the Fizeau image, which matches the diffraction pattern of a sub–aperture, represented by the dotted line fit. The solid line is the densified intensity profile. Both snapshot images were taken in a short succession with the same exposure time of 100 s. An intensity gain is noticeable by comparing the graphs. Ghost images (left and top of the surface plot), caused by a sub-pupil diffractive spill off of light outside of the facing micro lens are visible around the densified pupil image. The loss can be negligible with proper adjustments.

the micro-lenses in place (densified pupil). Substituting these values in the previous equation and dividing the densified pupil photon count by the Fizeau photon count

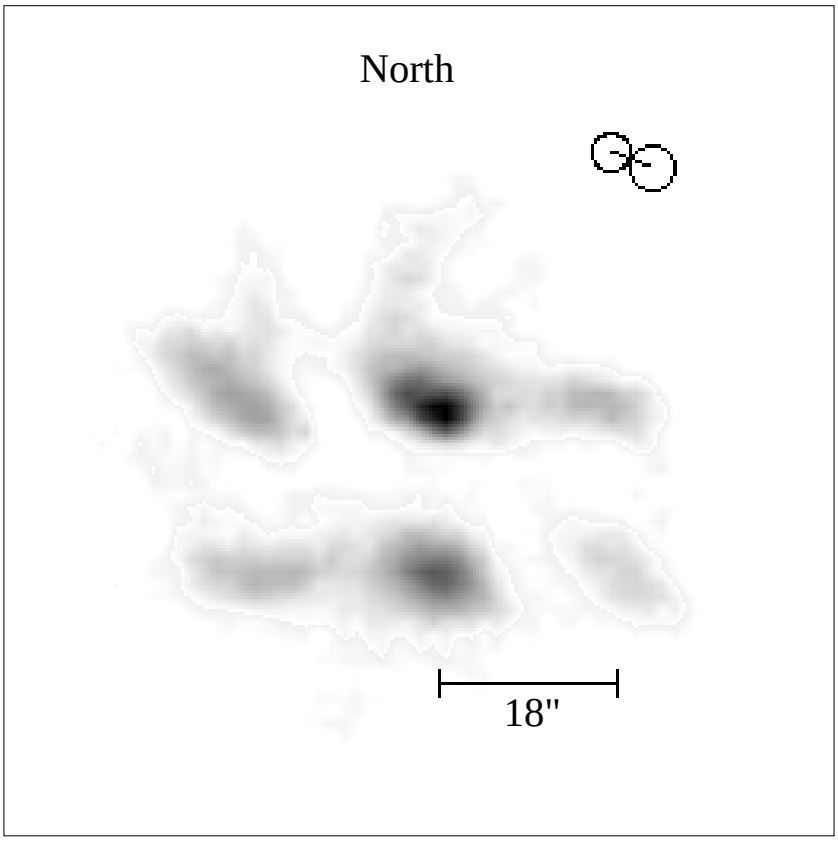

Fig. 3.5.— White light image of the double star α Gem produced by the miniature hyper-telescope. The central peak is seen to be double in accordance to the calculated position angle and separation of the binary star (sketched at top–right). Attenuated and dispersed side lobes are also visible around the central peak owing to the incomplete pupil densification and to a slight pointing offset of the telescope. The ghost images shown in Fig. 3.4 are outside the picture.

we find a value of $100\times$ for the intensification.

We then calculate the intensification factor from the images used for generating the plots of Fig. 3.4. For the densified pupil image and the Fizeau image, the intensity f was measured by integrating the central peak. The measurements were repeated for the Fizeau and densified configuration, using several recorded images. The comparison of the obtained values showed an intensity gain of $9.2 \pm 0.4\times$ of the densified with respect to the Fizeau configuration. When we take into account the stray light introduced in the measurement, caused by the instrument not being properly baffled we obtain a value of $24 \pm 3\times$, closer to the theoretical value. The stray light produced a constant offset in both the Fizeau and densified pupil image. The value of this offset was calculated from the Fizeau image by fitting to the measured data an Airy function corresponding to the diffraction function of the $0.8\,mm$ entrance apertures

Fig. 3.6.— Numerical simulation of PSF for the instrument (left) with the pupil densifier removed (Fizeau mode), in densified-pupil mode on a dispersed order (centre) and the star α Gem (right). Comparing the star image to the numerically simulated PSF we deduced that pointing errors positioned the object outside the field of view of the interferometer. The result is a dispersed image of the double star.

(Fig. 3.4). After the first minimum at $220''$ the function is nearly constant and its corresponding value can be subtracted from the intensity calculation of the Fizeau and densified pupil images. We verified that the discrepancy between the Airy fit and the data, towards the end of the plot, was due to the detector response threshold at low light intensity levels. This effect was found in several other images. The data plot is also affected by photon and atmospheric noise. The remaining discrepancy between the theoretical and the measured intensification is probably caused by the residual optical path errors introduced by the micro-lenses unequal thickness, the atmosphere and the misalignment of the micro-lenses with respect to the Fizeau mask.

Given its miniature size**,** narrow field and modest collecting area ($41\,mm^2$), comparable to that of a naked human eye, the hyper-telescope was tested on bright binary stars. Fig. 3.5 shows the image obtained on α Gem the night of December the 3rd 1999 with a $30\,s$ exposure. This image is compared to the calculated position angle and separation of the system[3] for $JD\,2451515.694$ in Fig. 3.5

The orbital parameters of the star were obtained from the Washington Double Star catalog. The angular separation ρ and the position angle θ were calculated using the peak pattern produced by the array. The period of the peaks is in fact equal to λ/s; we found a value $\rho = 4.1 \pm 0.4''$ for the angular separation. The position angle θ measured on the photo centres of the double star image produced a value of $\theta = 67 \pm 3°$. This values agree with the calculated separation $\rho = 3.97''$ and position angle $\theta = 67.4°$.

[3]The separation and orientation of the peaks was consistent with what I expected.

3.5 Discussion

The use of a square grid aperture was dictated by the geometry of the micro lenses used, which permitted to easily achieve pupil densification. Periodic arrays, with either square or hexagonal pitch, have interference functions similarly having a periodic array of peaks of uniform height. Non-periodic arrays, composed, for example, of concentric rings of apertures providing little or no redundancy have a speckled halo of side-lobes in their interference function. The average level of this halo is N times fainter than the interference peak, assumed perfectly phased.

We found that acquiring the image requires a pointing accuracy better than $18''$, corresponding to the distance of the first dispersed side lobes. The wavefront propagating from the star must be parallel to the main axis because an angle of the wavefront with the axis produces an increase of the OPD among the different apertures. As a result the white light central peak is shifted outside the magnified diffraction function. Since the array behaves as a bi-dimensional grating one of the dispersed peak may be found in the centre of the diffraction function. This will still form an image but dispersed and so elongated in one direction (Fig. 3.6).

A disadvantage of Michelson with respect to Fizeau arrays is the limited field of view. This is noticeable for an object moving off axis on the sky : the diffraction envelope from the sub–pupils moves with a lower speed than the interference peak forming the image, the speed proportional to the densification factor (Labeyrie 1996). From this observation, we define the field of view for a densified pupil interferometer as the angular extent on the sky over which the white image of stars remains inside the diffraction envelope of the sub–pupils. Owing to the pupil densification, the field thus defined is typically much narrower than the Airy radius of the sub-apertures on the sky. Following this definition, the field of view for a densified pupil interferometer depends on the amount of densification achieved**.** Maximum densification is achieved when the sub–pupils become adjacent**.** When this occurs the first dispersed side lobes coincide with the first zero of the diffraction function. In the practical case of our array we did not reach the maximum pupil densification since the first side lobes are still visible. The distance between 2 apertures is $8\,mm$; in the image plane the angular distance between the central white light peak and the first dispersed peak is then $\alpha = \lambda/s$, giving α slightly larger than $18''$ (λ and s as previously defined).

The basic gain of densified-pupil imaging , with respect to Fizeau, is that the concentration of energy from a halo of many dispersed peaks into a single white central peak intensifies the main image, thus increasing its ratio to photon-noise[4]. A more accurate device would contain 2 micro lens arrays working in an afocal configuration to meet the requirements of geometrical optics as sketched in Fig. 3.1. In the current device, shown in Fig. 3.2, the diffracted Airy patterns from the sub-apertures have their feet which fall upon neighbouring micro-lenses and this produces “ghost images” in the focal plane shown in Fig. 3.4. The shape of the high resolution peak is not

[4]This is very important when background and detector noise are dominant.

affected but its intensity is thus slightly reduced. Other losses in the system are caused by the imperfect alignment of the diffracted sub-pupils with the micro-lenses. This effect is seen as an asymmetric intensification of the side dispersed peaks with respect to the central white light peak. Most important perhaps, the phasing of the micro-lenses is less than perfect. This affects the intensity of the interference peak and creates a speckled halo around it.

3.6 Conclusions

The rather modest scale of the miniature hyper-telescope sufficed to verify the theory of its operation and to confirm the imaging performances to be expected with future interferometers at the kilometres scale. We have verified that arrays in which the entrance and exit pupil are non homothetic can form direct images, contrary to what was commonly believed. We have also measured an intensity gain of $24 \pm 3\times$ with respect to an equivalent Fizeau array and this is considered as supporting the $100\times$ value obtainable in principle with perfectly phased components.

Hyper-telescope architectures are candidates for the next generation of extremely large ground-based telescopes. Aperture sizes even larger than the 30 to 100 metres, currently considered for large steerable mosaic mirrors (Gilmozzi et al. 1998), can be implemented in the form of sparse mosaics. Rather than large pointing mounts, these can extend the principle of the Arecibo radio-telescope , with a fixed diluted primary mirror and moving focal optics, possibly carried by stationary balloons. This configuration appears of interest even to achieve kilometre size apertures .

In space, the situation seems more favourable and many sub-apertures can be combined in formation flight to achieve kilometre size apertures (Boccaletti et al. 2000) for detecting Earth-like exo-planets.

Acknowledgements

This work is based on observations with the equatorial table at the Observatoire de Haute Provence and used hardware and software of the Observatoire de la Côte d' Azur for data reduction. We thank the referee, Jacques Beckers, for his useful criticism. One of us (Ettore Pedretti) would like to thank Farrokh Vakili for his encouragement and many useful discussions.

Chapitre 4

L' Électronique Reconfigurable De l'interféromètre IOTA.

Pedretti, E., Millan-Gabet, R., Monnier, J. D., Morel, S., Traub, W. A., Carleton, N. P., Berger, J., Schloerb, P., Brewer, M. K., Ragland, S. & Lacasse, M. G., 2003, paru dans *Proceeding of SPIE* **4838**, 943.

Résumé

Nous décrivons un nouveau système de contrôle pour la caméra proche infrarouge PICNIC et le suiveur d'étoile visible, implanté à l'interféromètre IOTA, basé sur les circuits programmables ALTERA Complex Programmable Logic Device (CPLD). Ces composants digitaux fournissent une interface adaptable entre le système de contrôle et les détecteurs utilisés à IOTA, et permettent un grande flexibilité pour connecter des instruments très différents. En particulier les circuits horloge et calcul utilisés pour la caméra PICNIC peuvent être changés en quelques millisecondes pendant les observations. La caméra peut être ensuite utilisée en un mode de lecture plein champ, utilisé pour les alignements et diagnostiques, et un mode où N pixels sont lus pour l'enregistrement de données scientifiques.

Mots clé :interférométrie infrarouge, contrôle de détecteurs, acquisition de données, CPLDs, instrumentation.

Introduction

Les résultats de cet article ont été présentés au cours d'une contribution orale que j'ai donnée au colloque SPIE en 2002 à Kona, Hawaii dans la section Interferometry for Optical Astronomy II. J'y décrit un contrôleur universel réalisé à partir de circuits programmables CPLDs qui est utilisé à IOTA d'une part pour l'acquisition des images d'une caméra proche-infrarouge et d'autre part pour le suivi d'étoile dans le visible.

J'avais déjà utilisé des composants similaires appelés FPGAs (Field Programmable Gate Arrays) pour un projet antérieur mené à l'Observatoire de Haute Provence. Contrairement aux CPLDs, ces composants ne sont pas re–programmables, mais ils présentaient pour ce projet l'avantage de pouvoir réaliser des circuits complexes dans un petit espace. J'ai réalisé avec ces composants un contrôleur pour l'entraînement du télescope boule, télescope conçu par Antoine Labeyrie pour l'interférométrie optique et infrarouge. Le même circuit réalisé avec des composants traditionnels aurait été composé de plusieurs cartes électroniques relativement encombrantes. Le circuit que j'ai réalisé était complêtement contenu dans une FPGA et présentait l'avantage de pouvoir très facilement être utilisé sur des télescopes traditionnels.

L'expérience acquise à Haute Provence fut très utile pour réaliser le projet des contrôleurs des caméras à IOTA. J'ai jusqu'à présent réalisé 5 circuits qui sont installés sur l'interféromètre IOTA :

- deux contrôleurs pour la caméra infrarouge
- deux circuits pour deux différentes caméras visibles (utilisées pour la correction active du tip-tilt pour les télescopes)
- un circuit utilisé pour acquérir des données à partir de photodiodes à avalanche.

Reconfigurable electronics at the IOTA interferometer

Pedretti, E., Millan-Gabet, R., Monnier, J. D., Morel, S., Traub, W. A., Carleton, N. P., Berger, J., Schloerb, P., Brewer, M. K., Ragland, S. & Lacasse, M. G., 2003, in *Proceeding of SPIE* **4838**, 943.

Abstract

We describe the new control system for the PICNIC near-infrared camera and the visible star tracker, implemented at the IOTA interferometer, based on the ALTERA Complex Programmable Logic Device (CPLD) technology. These digital components provide an adaptive interface between the control system and the cameras used at IOTA, allowing flexibility when connecting very different devices. In particular the clocking and processing circuits used for the PICNIC camera can be changed in milliseconds during normal operation. The camera can then switch between full quadrant readout mode used for alignment and diagnostics, and a N pixel readout mode used for science operation.

keywords : infrared interferometry, detector control, data acquisition, CPLDs,

4.1 Introduction

A digital circuit is built by connecting several devices which perform logic functions. Such devices usually provide standard functions of different complexities, starting from simple logic functions such as Small Scale Integration (SSI) and Medium Scale Integration (MSI) Transistor-Transistor Logic (TTL) device and ending in high performance full custom designs such as microprocessors and random access memories. Full custom design requires years of development and test and is used when high volume production is required.

There are intermediate solutions for building prototypes and for small volume production. The so called Programmable Logic Device (PLD) permits full construction of logic circuits by internally connecting basic logic functions such as logic ports and flip-flops by burning fuses or using electronic switches.

CPLDs and FPGAs (Field Programmable Gate Arrays) permit the implementation of complex digital circuits on a single chip. CPLDs tend to have faster and more predictable timing properties while FPGAs offer the highest gate density (Hamblen & Furnan 2000). The number of gates in the chip is on the order of hundreds of thousands and this number is increasing rapidly while the technology improves. In the Altera Flex-10K70, used in the PICNIC IR-camera at IOTA, gates can be interconnected to form complex networks using electronic switches ; the switch interconnections are stored on a static RAM, so the interconnection among elements can be changed in just milliseconds. This means that a single component can host several circuits performing very different functions at different times.

CPLDs can be programmed using different tools :

- CAD entry, using standard electronics symbols interconnected by drawing wires.
- AHDL (Altera High level logic Description Language) : C-like Altera proprietary language which describes the interconnection of various components into a logic circuit.
- VHDL (Very High level logic Description Language) : Pascal-like language which describes interconnection among logic blocks.

There is no particular advantage in using VHDL with respect to AHDL or the CAD entry but we decided to use VHDL because it is a widely used industrial standard.

The work presented in this paper concerns the design of several circuits loadable in the two CPLD interfaces used at IOTA and of the control software built for them. In particular :

- A circuit for fast readout of a visible CCD matrix used for the detection of star centroid error in the tip-tilt system, which feeds the telescopes' light to the beam combiner.
- A circuit capable of reading a whole 128×128 PICNIC matrix for future use as a IR wavefront sensor for the tip-tilt correction system and for the beam combiner alignment.
- A circuit for the fast readout of the IONIC (Berger et al. 2003) integrated optics beam combiner or the IOTA free-space combiner (or any future beam combiner to be implemented at IOTA) through the readout of sparse pixels on the PICNIC matrix.
- Software libraries built to interface the CPUs to the various circuits.

4.2 The Data Acquisition And Control Subsystem

Driven by the requirements of the 3-telescope upgrade at the IOTA interferometer (Traub et al. 2003), the data acquisition and control system at IOTA has undergone through major changes. The distributed computing network once composed of separate computers running different operating systems are now replaced by a system based on the VME bus and the real time development system *VxWorks* in order to cope with the increased data processing needs introduced by having two

new baselines and an additional telescope. A block diagram of the real time system is shown in Figure 4.1

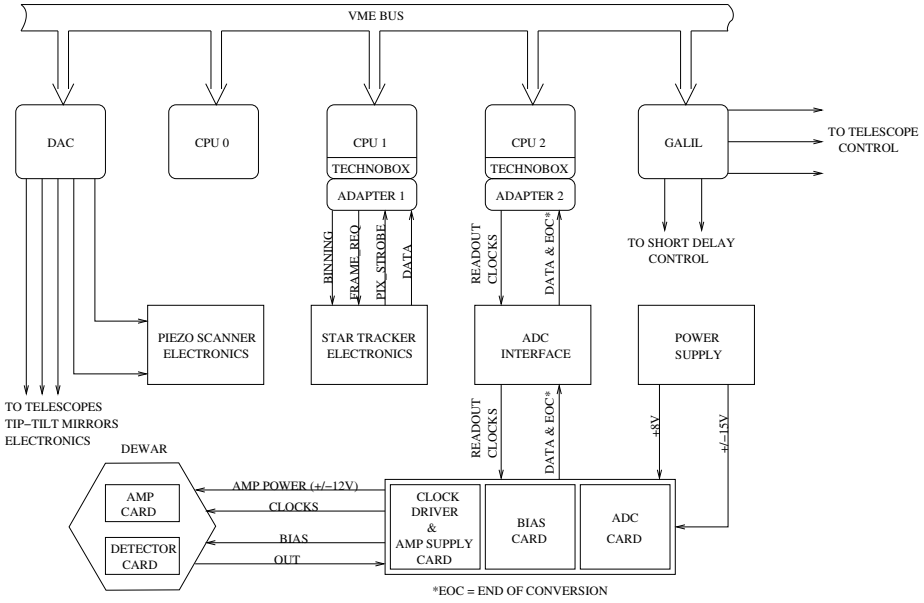

Fig. 4.1.— Control system block diagram at IOTA. The three CPUs manage different functions of IOTA. CPU-0 controls the telescopes and the short delay lines through the Galil interface. The long delay lines are controlled through a standard Ethernet socket. Components, like shutters and remotely operated mirrors, are operated through a serial interface board. CPU-1 is entirely dedicated to the wavefront tip-tilt sensing and correction. The interface functions for the wavefront sensors are implemented through the Technobox re-configurable interface, which uses an Altera CPLD. An adapter was built to drive a differential cable which runs from the Technobox interface to the remote star-tracker camera. CPU-2 is dedicated to data acquisition and fringe-tracking. The CPLD on the Technobox interface performs all the tasks necessary to the PICNIC camera operation.

The new control system is composed of three Central Processing Units (CPUs) based on the Motorola Power-PC microprocessor architecture. This hardware runs on the VxWorks real time operating system. The logic functions programmed inside the CPLDs (Hamblen & Furnan 2000) are implemented using a high level description language called *VHDL.* The circuit can change according to the application and is downloaded by the CPU to the CPLD board permitting very high flexibility in interconnecting dramatically different digital hardware. This means, for example, that a new IR star tracker could be plugged into the system in place of the visible star tracker without changing the interface. Only a different circuit is loaded and a different adapter plugged in. The adapter is simply a passive electrical adaptation from the Eurocard connector on the backplane of the VME rack to the electronics to be controlled.

4.2.1 The VxWorks Real-Time System

The control system for the IOTA interferometer is centralised in a VME type computer. VME is an industrial standard defining the mechanical and electrical characteristics of a computer bus, oriented to instrumentation control. CPUs based on different processors can be plugged into the bus : the most widely diffused architectures are Power-PC (a Motorola - IBM joint venture), SPARC (SUN based architecture) and Intel architecture.

Real-time means that the different tasks are executed at very precise intervals in time, synchronised by a "real time clock" which defines the pace of the system. This is crucial for instrument control (in our case controlling visible and IR cameras, telescopes, delay lines, fringe trackers and data storage).

The VxWorks system is UNIX based, meaning that all the development can be done on a UNIX computer, using standard cross-compilers (GNU) editors, etc. UNIX is not per-se a real time system (RT-LINUX is a notable and very interesting exception in the open-source real time world). The UNIX computer host (in our case a SUN station) is connected to the VME rack through a fast optical link and communicates with three VME-based CPU targets. The SUN host loads the compiled programs on the targets but these programs (tasks) are executed using another operating system (VxWorks) which is basic and streamlined, but allows us to use standard UNIX sockets to communicate with UNIX based workstations, file-servers etc on a standard Ethernet connection.

4.2.2 Reconfigurable Electronics Versus Programmed I/O

Programmed I/O using microprocessors, microcontrollers or computers connected to hardware implemented with parallel interfaces is widely used to control equipment. The advantage of these systems is that their operating mode can be easily changed by modifying the control program, compared to hard-wired digital circuits which once established can normally not be changed. Digital circuits have the advantage of being usually faster and more predictable in real time applications because they are tailored to the specific task, while microprocessors are built for general applications. CPLDs get advantages from both worlds.

- The circuit can be changed in real time like a program in a processor based machine.
- The digital circuit is tailored to the application.
- It is advantageous to use the same interface for controlling different hardware, for maintaining spare boards and for debugging purposes.

4.2.3 Disadvantages of Reconfigurable Hardware

Programming FPGAs or CPLDs is not as straightforward as programming a micro-controller. The application is still a digital circuit which, even if it has been implemented correctly from the digital logic point of view, could still not work, or

would work at slower speed than expected, due to internal propagation delays of the clock tree and/or of specific signals. CPLDs are usually more predictable than FPGAs from the internal delay point of view (Hamblen & Furnan 2000).

4.2.4 Circuit Implementation

We developed our circuits on a commercially available PCI-PMC card which contained an Altera 10K70 CPLD. This card plugs directly into the PMC slot of our VME CPUs. The advantage of this configuration is being able to load a new circuit in the CPLD from the CPU memory or from the disk during operation. The disadvantage of this configuration, we found out, is in forcing outputs to be be assigned to specific components and I/O pins. The compiler prefers that the pins are freely assigned the first time it builds the circuit, in order to optimise the routing of signals. Fixed output pins likely add delays to the circuit which makes it failure prone at higher speed. Another disadvantage of using a PMC interface is the intrinsic difficulty in using an oscilloscope probe on the component ; also the real time debug tools present in the parallel port programming interface cannot be used, complicating the debugging process.

A PMC interface, electrically identical to a standard PCI bus used for on personal computers, connects the CPLD to the CPU. There are several components present on this board. The components used for the star-tracker and IR cameras are :

- The PLX-9050 PCI bridge, which is connected to the PCI bus ; its main function is the bidirectional data transfer between the PCI bus and the internal bus of the board. An internal bus composed of 16 data lines, 18 address lines and read-write and enable signals, interconnects the components present on the board. It can generate interrupts on the PCI bus in response of events generated by the CPLD.
- A $128K \times 16$ static RAM connected to the internal bus. The CPU has access to this RAM through the PCI bridge. The RAM is shared by the CPLD using arbitration signals.
- A 33 MHz clock line (PCI clock) used as master clock for the CPLD.
- An Altera 10K70 CPLD. This component is programmed through the PLX-9050.

4.3 Visible Star Tracker Read-Out Using a CPLD

Unlike the previous version of star tracker at IOTA, which used two CCD detectors (one for each telescope), the new star tracker uses only one detector for acquiring stellar images from three telescopes. The software running on CPU-1 is responsible for bringing the star to the right position on the detector and sending corrections to the tip-tilt mirrors which feed the beam combiner. The circuit built on the CPLD interfaces the existing CCD electronics to CPU-1 without building any extra hardware, with the exclusion of interconnection cables and differential line drivers. The

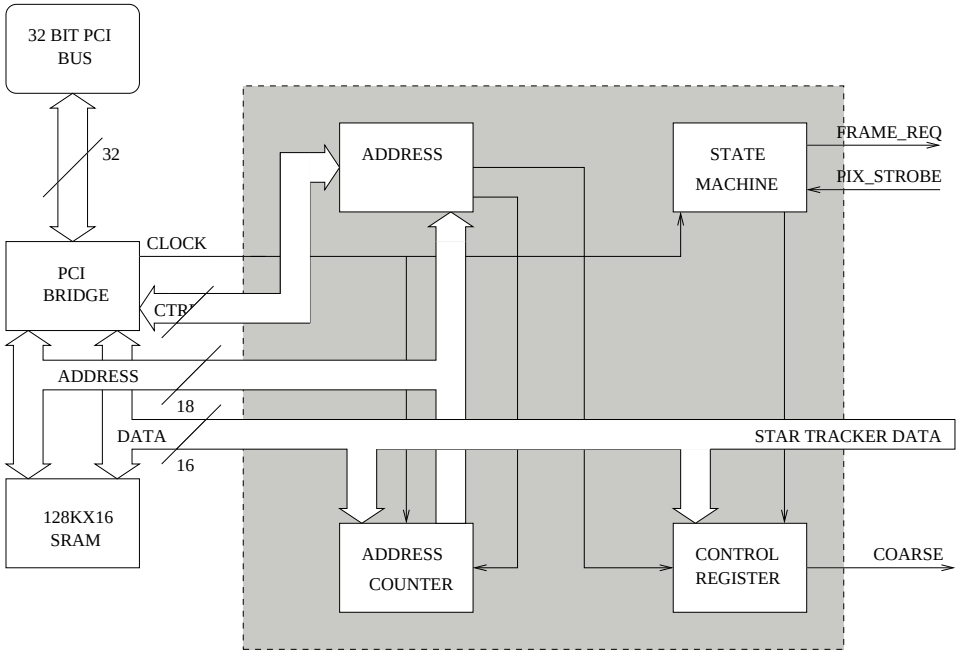

Fig. 4.2.— The visible star tracker data block diagram. The state machine implemented here is mostly responsible for the arbitration of the internal bus with the PCI-bridge. It also sends a frame request to the star-tracker camera. The star tracker then clocks data words out, one by one and increments the address counter until 16 data words are transfered.

star tracker camera transfers data on a 12-bit parallel data bus. Three control lines are used :

- Frame_req ; this line is asserted by the interface to ask for a new frame.
- Pix_strobe ; this line is asserted by the camera after a new word is put on the data bus.
- Fine/coarse ; this line is asserted by the interface to select the coarse or the fine mode for the readout.

The transferred image is 8×8 pixels wide (64 data words are transferred), in coarse or fine pixel mode. In coarse mode the full 32×32pixel CCD image is binned in blocks of 4×4 to generate an 8×8 output. this 8×8 image has four 4×4 quadrants ; three of the quadrants are used for the star images from our three telescopes. In fine mode only the central 8×8 pixels are read out, and the rest ignored ; this mode cannot be used for three stars. The camera is connected to the interface with a long parallel cable using differential line drivers and receivers. Figure 4.2 shows the star tracker implementation on the reconfigurable interface. The CPLD (shaded box) is controlled through the PCI bridge which can write into a control register defined in the CPLD. The acquisition starts when the CPU asserts the start bit in the control register. This bit is hard-wired to the control line “Frame_req” of the CCD star-tracker and also

connected to a state machine inside the CPLD. The state machine changes state and asks the CPU through the PCI bridge for the control of the internal bus; the PCI bridge asserts a line to inform the state machine that the CPU has released the bus.

The address counter is enabled; this counter is connected to the address lines of the static RAM and it is incremented directly (after being synchronised with the 33MHz system clock) by the star tracker through the signal "Pix_strobe". The data bus is bufferised by D-type flip-flops (to synchronise it with the system clock) and connected to the RAM buffer through tri-state ports, to avoid conflicts with the CPU signals. Bus arbitration is performed by the CPLD and the PCI bridge. After the 64 words have been transferred, the CPLD asserts the INTA line of the PCI bridge. This line is an interrupt which is serviced by the CPU as a high priority task. When received, the CPU transfers the block of 64 words from the static RAM to a buffer and processes it to calculate the centroid of the star and correct the star-tracker tip-tilt mirror.

If for any reason the number of transferred words is less than 64, the system would hang, waiting for the missing words. To avoid this we implemented a watchdog timer; the timer is reset by the INTA signal every time a data frame of 64 words is received. If data transfer takes more than 4.3 ms (the total frame time is around 3.3 ms) the timer sets the timeout flag in the control register, informing the CPU that a communication problem has occurred.

4.4 An Infrared Camera Based On the PICNIC Detector And CPLD Technology

4.4.1 The PICNIC Detector

The PICNIC focal plane array (Kozlowski et al. 2000; Cabelli et al. 2000) is composed of four 128×128 quadrants of a HgCdTe detector which can be addressed simultaneously and independently. The active area of each pixel is $40\mu m$ square. The PICNIC detector is the evolution of the NICMOS3 (Kozlowski et al. 2000; Cabelli et al. 2000) array. The quantum efficiency (QE) of the detectors is better than 50% for wavelengths in the range of $0.8 - 2.5\mu m$.

The PICNIC detector is a hybrid device where the detectors are built on a small band-gap material (HgCdTe) on an insulator substrate (sapphire) which is interconnected to a silicon substrate, where the clocking and analog circuitry are built and interconnected through indium bumps (a well established technology where indium is deposited on the contacts of the two wafers and the bumps are pressed together to make contact).

The P-N junctions deposited on sapphire are illuminated through this substrate. These junctions are reverse biased during the RESET cycle, when the junctions are connected to a positive potential, so that conduction cannot happen and the width of the depletion zone across the junction is increased. We recall that the depletion zone

Fig. 4.3.— The PICNIC camera dewar and the optics focusing the beams from the IONIC3T beam combiner are shown in this picture. The mechanical assembly is an improved version of the previous NICMOS3 design, but the dewar is taller and contains more liquid nitrogen, one extra filter wheel is implemented, (in order to insert density filters), and both filter wheels are able to be motorised.

is a region devoid of free carriers (electrons or holes) which naturally forms at the interface of different conductor or semiconductor materials (eg. copper-constantan thermocouple for metals, or semiconductors doped with acceptors or donor atoms ; P and N semiconductors). The junctions can also be considered, in the case of reverse bias, as a capacitor charged by a bias potential. After the bias potential is applied and disconnected, when a photon hits this region it will generate a electron-hole couple (intrinsic carriers) which will recombine in the depletion zone reducing its thickness and also the electric charge deposited on the two sides of the junction. This voltage decrease can be measured through a source follower circuit, a MOS feedback amplifier of unity gain and very high input impedance. Since this discharge follows

the reverse bias characteristic I-V curve of a diode it is intrinsically non-linear before the saturation region.

When the photon-generated carriers have depleted all the initial charge separation, the device is saturated. The dynamic range of the detector is then determined by the saturation voltage applied at the beginning of the cycle.

Analog Electronics

The analog electronics on the new PICNIC camera is identical to the electronics used in the IOTA NICMOS camera (Millan-Gabet et al. 1999a) with the exception of new PCB housing the array itself.

Clocking The Detector

The detector matrix is addressed through two shift registers : the horizontal shift register and the vertical shift registers. These are controlled respectively by the LINE, FSYNC clocks and the PIXEL, LSYNC clocks. FSYNC and LSYNC act as reset for the shift registers (active low) : when they are asserted the respective registers are loaded with all zeroes. The LINE and PIXEL clocks are double edge clocks. The first edge of such clocks will simply connect the line or pixel circuitry to the output of the detector ; the second edge will put a zero in the first bit of the clocked shift register. The following clock edges will shift the zero of one position throughout the register ; the zero bit will enable an analog switch to read the corresponding line and pixel of the detector. Before reading the detector the pixels must be connected to the bias potential, in order to charge the junction capacitance. The circuit used in the PICNIC detector permits us to reset a whole line at the time, a large improvement in speed and performance with respect to the NICMOS3 detector, where the pixels were reset one at a time. Asserting the RESET signal (active high) together with the LINE clock will reset the whole line.

Implementation of the Quadrant Readout Mode

Although the camera's principal use is reading out a sparse number of pixels illuminated by the beam combiner, it is necessary to read a whole quadrant for alignment purpose, and, because in the future the camera could be used as an IR star tracker, to track sources which are too faint at visible wavelengths for the CCD detector. The mode adopted for quadrant readout is Correlated Double sampling (CDS).

Correlated Double Sampling

In CDS mode the detector is reset, sampled, allowed to integrate and re-sampled. The difference between the two frames is then recorded. This reduces noise and eliminates detector offsets

CDS is implemented entirely in the CPLD electronics. The CPU receives a buffer containing the final, ready to use, data.

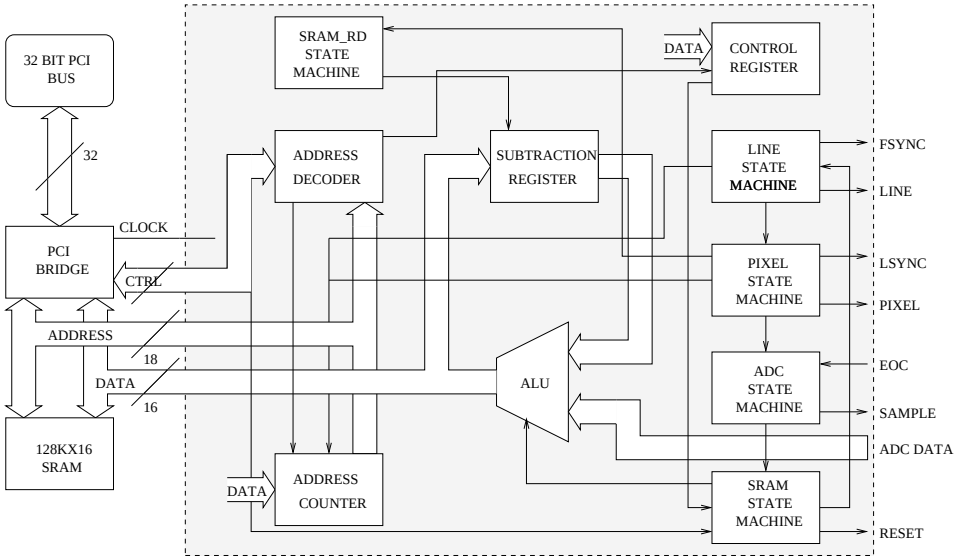

Fig. 4.4.— The PICNIC quadrant readout circuit. Five state machines are responsible for the operations of the camera. Complex functions are broken into elementary functions of clocking lines, pixels, resetting the detector, commanding the ADC and transferring data into SRAM, executed by each single state machine.

This mode reads a whole quadrant from the PICNIC array ; the image is stored in the static RAM on the Technobox card which is shared between the CPU and the CPLD through the PCI bus. The readout starts when the start bit in the control register of the CPLD is asserted by the CPU. The interrupt line (INTA) is asserted when the readout process has finished and a frame is present in the SRAM.

Between these events many operations are handled in parallel by state machines which have been built into the CPLD ; these state machines are :

- SRAM state machine which handles communications with the PCI bridge for bus arbitration. This state machine is a slight modification of the state machine used for the same purpose in the star-tracker. It polls the start bit of the control register and sets a semaphore which starts the clock generation state machine. If a reset frame and an image frame have been acquired and subtracted, it releases the PCI bus and asserts INTA.
- LINE state machine, which controls the line clocks generation for the PICNIC array ; once a line has been selected it sets a semaphore to start the PIXEL clock generation ; lines are counted by the line counter. It will also assert the RESET line, together with FSYNC if the toggle flip flop, which keeps the state of the frame (reset-frame or data-frame), is set on reset-frame.
- PIXEL state machine, which controls the PIXEL clock generations for the PICNIC array ; it controls the sequence of clocks and sets a semaphore when the ADC can sample the selected pixel ; pixels are counted by the pixel counter.
- ADC state machine : it sends start of conversion to the ADC, waits for the

end of conversion signal from the ADC and writes a word of data in the static RAM if the toggle flip-flop is in data-frame state. If it is in reset-frame state, it stores the difference between the data word at the current SRAM address and the data word obtained from the ADC ; the SRAM address is obtained by combining the line counter and pixel counter.

– Read SRAM state machine : it reads one word of the reset frame previously written to SRAM, during the ADC conversion. The current value of the ADC is subtracted from this value .

The DAQ scheduler task, running on the CPU when in quadrant state loads the circuit into the CPLD and initialises the readout parameters. After that the start bit is asserted in the CPLD register and the state machines are started.

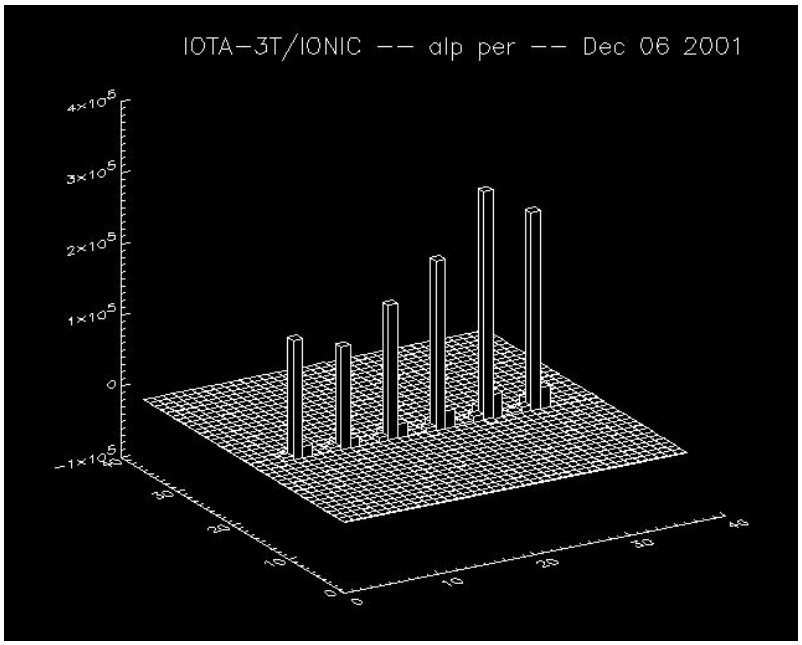

Fig. 4.5.— Image of the pixels illuminated by the IONIC3T beam combiner on the PICNIC camera in quadrant readout mode. Two consecutive channels contain information about the same baseline and they are subtracted one from the other to improve SNR and calibration.

Readout Parameters

Some readout parameters can be changed by the application running on the CPU, accessing the registers on Altera :

1. PICNIC base clock period. The 33 MHz PCI clock is divided by a programmable counter built into the CPLD, in order to generate the base clock rate used to clock the PICNIC array ; the counter can be programmed by the CPU through the PCI bridge.

2. Delay between PICNIC clock and sample assertion ; this is necessary to avoid sampling the PICNIC pixel when it is not stable, after it has been addressed, which results in increased readout noise. The delay is generated by a programmable counter and is accessible to the CPU through the PCI bridge.

3. Integration time ; this is also a presettable counter which determines the time between the reset frame and the image frame

4. Sub-quadrant corner position ; with these variables it is possible to define a sub quadrant to read a small area of the detector. This flexibility will be crucial when implementing an IR wavefront tip-tilt sensor.

Interferogram Detection - Scan Mode

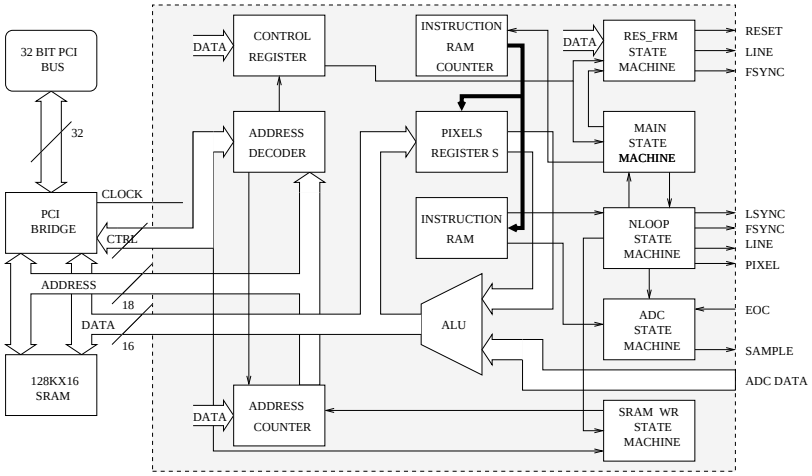

Fig. 4.6.— The block diagram of the PICNIC camera in scan mode. The basic functions are implemented with five state machines. The same functions of the NICMOS3 camera are available for integrating pixel values. The pixel readout sequence is stored in the instructions RAM, internal to the CPLD. This RAM stores micro-coded instructions specialised to generate clocks sequences for the PICNIC array.

This mode reads a number of pixels at arbitrary coordinates on the camera. For better clocking efficiency the pixels should be closely spaced and, preferably, on the same line. The pixel voltages are read sequentially and stored in SRAM. INTA is asserted at the end of every group of pixels readout. INTA is used to delimit the end of a data frame but it is also used to step the piezo OPD scanner which is synchronous with data acquisition. This simple cycle is performed several times and stored in memory as a time sequence. When one sequence (or scan) is finished a flag is asserted in the control register and the CPU transfers the stored vector to a buffer.

Differential Sampling

With this method the array is reset only once, then sampled for the pixels of interest and the difference between a sample and the following sample in time is taken ; avoiding the array reset for every frame readout improves the SNR and the readout speed but reduces the dynamic range of the detector.

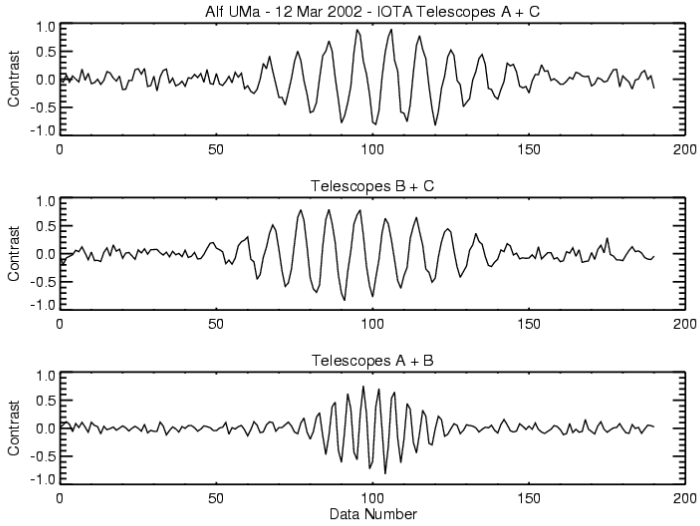

Fig. 4.7.— Fringes from the IOTA IONIC3T combiner on the PICNIC camera obtained using the CPLD sparse pixels readout circuit. Complementary fringes for each telescope pair have been subtract to enhance the SNR.

Circuit Implementation

We use here the same methods implemented in the NICMOS3 (Millan-Gabet et al. 1999a) camera previously employed at IOTA : each pixel can be sampled several times and the values added up and stored in a register ; we call this *reads*. It is also possible to read the whole group of pixels and integrate the values separately ; we call this *loops*. In this way values are integrated and the readout noise is divided by $\sqrt{N}$ where $N = loops \times reads$. Using many reads achieves a better SNR but increases the latency between sampling different pixels ; using many loops degrades slightly the SNR since we are clocking the detector, which adds noise, but the time delay among different pixels is reduced.

This was implemented in the readout software for the NICMOS3 camera. The hardware implementation of this function for the PICNIC was more complex than the software implementation for the NICMOS3 camera. Data for each pixel must be stored in separate registers and added there, then data is transferred to SRAM and INTA is sent to the CPU through the PCI-bridge. The interrupt must be cleared by the CPU at the end of this process. To limit access to the SRAM and avoid conflict with the CPU we opted to do processing in the internal registers rather than in the SRAM as was done for the quadrant readout. This unfortunately limits the number of pixels that can be read to nine, since generating internal memory in the CPLD is intrinsically inefficient. This limitation will only become important when spectral dispersion is implemented (Ragland et al. 2002).

The interrupt generated from the CPLD, other than merely informing the CPU that a new data point is available in the SRAM, is also used for incrementing the voltage ramp generated by a DAC card installed on the VME bus. The pixel registers, the adders used to integrate the value of the pixels, the counters which count the number of data points transferred, the SRAM address, the internal RAM address and clock generation are controlled by five separate state machines :

- RES_FRM_PROCESS state machine : this state machine resets the whole PICNIC array continuously, clocking lines from 0 to 127 and back to zero. This process is stopped when the start flag is asserted and the main process is idle.
- main state machine : schedules the N_LOOP_PROCESS state machine and increments the address of the instruction internal RAM which contains the readout sequence transfered from the CPU. It starts when the start bit of the control register is asserted ; it clears all registers and starts the loop state machine. It ends when the loop_tc semaphore is asserted.
- N_LOOP_PROCESS state machine : it is scheduled by the main process and decodes part of the instructions written in the internal RAM. The internal RAM is loaded by the CPU via the DAQ scheduler program. It schedules the SAMPLE_PROCESS and the SRAM_WR_PROCESS.
- SAMPLE_PROCESS : it sends start of conversion to the ADC, waits for the end of conversion signal from the ADC and writes a word of data to the internal register corresponding to the pixel sampled ; if the requested number of reads is greater than one the state machine reads the ADC several times and the values are accumulated in the corresponding pixel register.
- SRAM_WR_PROCESS : this state machine executes the data transfer to SRAM from the internal registers when the requested loops and reads are completed. When the sequence starts again to sample a new data point it executes in parallel, transfers the data from the pixel registers to SRAM and sends an interrupt when the process is completed.

Micro-Coded Instructions

It is highly desirable to have the flexibility of choosing which pixels are sampled in order to use different combiners. For this reason the scanning sequence has to be alterable. This was solved by allowing the state machines to change state according to a program written into a RAM internal to the CPLD. Five instructions can be executed by the state machines as shown in Table : 4.1 These instructions permit to

Instruction	Hex Value	Action
fsync	02	FSYNC pulse generated
lsync	03	LSYNC pulse generated
line	00	LINE clock transition n-times
pixel	01	PIXEL clock transition n-times
jump	04	Jump to program location

Table 4.1: CPLD micro-coded instructions

generate a clock sequence ; the LINE clock will change level n-times according to the value of the following byte in the program. The same happens with the PIXEL clock, but in this case every pixel is read n-times, according to the value written in the "Nreads" register. Loops are achieved through the jump instruction which permits to branch back to a specific instruction in the program. The loop is executed n-times according to the content of register "Nloops".

Readout Parameters

In this readout mode some of the parameters, which can be changed, are the same as in the quadrant readout circuit. Some registers are only used in the pixel readout mode.

1. PICNIC base clock period : same as in Section : 4.4.1 for quadrant mode.
2. Delay : same as in Section : 4.4.1 for quadrant mode.
3. Nloops : reads the specified pixels group in a loop several times, the value specified in the Nloops register. The values read are integrated separately in the pixels registers.
4. Nreads : reads the specified pixel several times the value specified in the Nreads register. It integrates the values for that pixel only and puts the value in the corresponding pixel register.
5. Readout sequence : vector containing the readout code sequence used to sample the pixels : the vector contains instructions which assert the lines LSYNC or FSYNC for the detector as well as the LINE and PIXEL lines. Line and pixel instructions have arguments which specify the number of lines or pixels to clock the detector
6. Nsamples : number of npixels sample acquired and stored into memory.

The C Libraries

The PPC-CPU is interfaced to the Altera CPLD using a PMC bus, as described earlier. The kernel of this library is given by the manufacturer of the card (Technobox). This is only an example which can be modified by the user according to the CPLD programming. The modules dealing with the PCI bridge and the remote programming of the CPLD do not need any modification.

Two basic function are associated with the library :

– Writing to the control register to modify the behavior of the CPLD.

– Read the static RAM and transfer its contents to a data buffer.

These functions are common to the CCD and the PICNIC camera readout circuits. .

4.5 Future Developments

Based on this positive first experience we envisage including other instruments under the control of the CPLD reconfigurable interface. The first application in order of importance will be the interfacing of the avalanche photo-diodes (APDs) (Coldwell et al. 1998) with the VME rack. These detectors are used for the visible beam combiner. This will entail implementing another circuit on the CPLD which will count the photo-events from the detectors. The rest of the electronics which deal with transferring data to the SRAM will probably stay untouched.

It has also been proposed to install an IR star tracker at IOTA using the previous science camera based on the NICMOS3 array. This requires some slight modifications for the clocking circuits used for the PICNIC camera but essentially most of the circuit used there for the quadrant readout could be ported untouched.

More sophisticated processing could also be ported to the CPLDs : in the case of the star-tracker circuits could be implemented to calculate the star centroids, unloading the CPU from processing tasks. Likewise, the piezo OPD scanner could be controlled directly by the CPLD by means of DAC circuits connected to its outputs, increasing the resolution of the waveform generated to scan the piezo mirrors.

4.6 Conclusions

We have shown that CPLDs are a mature technology which can handle the many digital circuit necessary to interferometer subsystems. At IOTA we were able to implement the complex functions necessary to read our science detector for different modes of operations, entirely on the CPLD. We have also shown the advantage of being able to change digital circuits on the fly and of using a standard interface for controlling very different electronics.

Acknowledgments

We thank the Altera corporation for providing the CPLD development software through the Altera University Program.

Chapitre 5

La Caméra Contrôlée Par CPLD De l'interféromètre IOTA

Pedretti, E., Millan-Gabet, R., Monnier, J. D., Traub, W. A., Carleton, N. P., Berger, J., Schloerb, P., Brewer, M. K., Ragland, S. & Lacasse, M. G., 2003, *à soumettre à PASP* .

Résumé

Nous décrivons une nouvelle caméra proche infrarouge, basée sur la matrice PICNIC, développée pour l'interféromètre "Infrared-Optical Telescope Array" (IOTA). Le système de contrôle de cette caméra est basé sur les circuits programmables CPLDs (complex programmable logic device). Cette architecture permet de produire des horloges stables pour la matrice PICNIC ce qui permet une lecture rapide et un bruit de lecture plus bas. L'architecture CPLD permet également une reconfiguration rapide du circuit. Nous démontrons cette caractéristique avec l'implémentation de circuits dédiés à deux fonctions : l'acquisition d'images utilisées pour l'alignement et la lecture séquentielle et rapide d'un nombre limité de pixels, utilisée pour la détection des franges d'interférences. Dans le mode de détections des franges, l'écart type mesuré pour une seule lecture du détecteur est $\sigma_{\mathrm{single-read}} = 8.7 \pm 0.6$ électrons. Dans le mode acquisition de données, le signal est donné par la différence de deux lectures successives. Le bruit sur ce type de signal est donc plus grand d'un facteur $\sqrt{2}$, donnant $\sigma_{\mathrm{read}} = 12.4 \pm 0.8$ électrons. Avec M multiples lectures d'un pixel donné, le bruit de lecture est réduit par moyennage et devient $\sigma_{\mathrm{M}} = \sigma_{\mathrm{read}}/\sqrt{\mathrm{M}}$, pour au moins l'intervalle $1 \leq \mathrm{M} \leq 16$, ce qui démontre une importante amélioration de la performance du détecteur PICNIC avec des lectures multiples.

Introduction

La nouvelle caméra interférométrique PICNIC installée à IOTA présente des performances supérieures à celles de l'ancienne caméra NICMOS. La raison principale de ces améliorations provient probablement du nouveau détecteur PICNIC désormais utilisé. Une autre raison est l'utilisation du nouveau contrôleur que j'ai construit pour cette caméra en utilisant la technologie CPLD. Ce nouveau contrôleur remplace un système basé sur un PC MS–DOS qui générait des horloges bien plus instables. Mon choix d'utiliser des CPLDs a été motivé par les résultats très satisfaisants que j'avais obtenus au cours de mon stage à l'Observatoire de Haute Provence, où j'avais déjà utilisé des field programmable gate arrays (FPGAs, technologie similaire aux CPLDs). J'avais réalisé, avec les FPGAs, un contrôleur pour l'entraînement du télescope "boule" (un télescope construit pour l'interférométrie optique et infrarouge). D'autres groupes ont construit des contrôleurs basés sur des "digital signal processors" (DSPs) (Fischer et al. 2003), des transputers (McLean et al. 1993, 1994; Probst et al. 1994; Joven-Alvarez et al. 1994), des processeurs bit–slice (Chin & Gezari 1987) et différentes combinaisons de ces technologies. Ces contrôleurs présentent des caractéristiques similaires à celles d'un contrôleur CPLD.

CPLD-Controlled PICNIC Camera at IOTA

Pedretti, E., Millan-Gabet, R., Monnier, J. D., Traub, W. A., Carleton, N. P., Berger, J., Schloerb, P., Brewer, M. K., Ragland, S. & Lacasse, M. G., 2003, *To be submitted to PASP* .

Abstract

We describe a new near-infrared camera based on the PICNIC array for the Infrared-Optical Telescope Array (IOTA). The camera control is based on a complex programmable logic device (CPLD). This architecture allows fast and stable clocking of the PICNIC array, resulting in faster and lower-noise readout. The CPLD architecture also allows on-the-fly reconfiguration of the readout circuit. We demonstrate this capability with the implementation of circuits dedicated to two different functions : imaging used for alignment purposes, and fast sequential readout of a few pixels used for interference fringe detection.

In fringe detection mode, the measured rms readout noise for a single read of the detector is $\sigma_{\mathrm{single-read}} = 8.7 \pm 0.6$ electron. In data-acquisition mode, the signal is the difference of two successive reads, so the noise on this signal is larger by $\sqrt{2}$, giving $\sigma_{\mathrm{read}} = 12.4 \pm 0.8$ elec.

With M multiple reads of a given pixel, the read noise averages down as $\sigma_{\mathrm{M}} = \sigma_{\mathrm{read}}/\sqrt{\mathrm{M}}$, for at least the range $1 \leq \mathrm{M} \leq 16$, showing that fast, multiple reads significantly improve performance in the PICNIC detector.

5.1 Introduction

The IOTA – a collaborative project between the Smithsonian Astrophysical Observatory, Harvard University and the University of Massachusetts at Amherst – is an optical long baseline interferometer located on Mount Hopkins, AZ. The array consists of three 45 cm diameter telescopes able to be relocated along the arms of an L shaped track. The arms of the L track are 15 m and 35 m in length, with south-east and north-east orientations respectively. The minimum and maximum baselines have length of 5 m and 38 m.

IOTA has operated routinely since 1995 with the first two telescopes that were first installed. Installation of the third telescope started in the summer of 1998 and culminated in February 2002, when first simultaneous three telescope measurements were obtained. For a full description of IOTA and its subsystems see Traub et al. (2000, 2003).

Driven by the requirements of the third-telescope upgrade, the control and data acquisition systems have undergone major changes. The distributed computing network, once composed of separate computers running different operating systems, has now been replaced by a system based on the VME bus (a real-time, control oriented computer architecture) and the real time operating system VxWorks. These changes have allowed us to cope with the increased real time control and data processing needs introduced by having two new baselines and an additional telescope.

The need for simultaneous combination of three telescope beams also imposes the following new constraints on our fringe detection camera. (1) More pixels need to be sampled, as any beam combiner design will have more outputs than for the two-telescope case. (2) Each beam combiner output contains less light from each telescope, due to the required additional beam splitting. (3) Measurement of the new closure-phase observable requires substantial overlap of interferograms, which have to be measured in the same coherence time. Therefore it is critical for the detection to be made in as short a time as possible compared to atmospheric piston time scales. Thus, building on the success of our previous NICMOS3-based infrared instrumentation (Millan-Gabet 1999; Millan-Gabet et al. 1999a) we have upgraded our science camera. The new camera, described in this paper, is based on the improved PICNIC array (developed by Rockwell Scientific). Mechanically, the new dewar is an improved version of that of the previous camera, but now hosts two motorized filter wheels which will allow us to conduct near-IR narrow-band observations.

The most important difference in the new camera over the previous NICMOS3 system is the use of CPLDs (Pedretti et al. 2002) as control electronics, to substitute for the previously-used PC based programmed I/O approach.

A block diagram of the overall control system is shown in Fig. 5.1. In this section the CPLDs are located in the blocks labeled “Technobox”. The CPLDs allow faster and jitter-free clocking of the detector, which benefits our measurements in three distinct ways. (1) Minimum clocking noise is expected due to the fact that our jitter-free clocking results in very constant effective integration times from sample to sample. (2) Lower effective noise results from being able to average a larger number of reads within the same total integration time per sample. (3) With lower noise, faster readout allows faster detection of interferograms with no loss in signal to noise ratio (SNR), ultimately improving the calibration of visibility amplitudes and closure phases as indicated above. Moreover, this method unloads the CPU from clocking tasks, freeing-up time which can be better spent in our also-new active fringe tracking task, described elsewhere (Pedretti et al. 2003).

The fast readout of a few pixels is very specific to interferometry. IOTA is and will be a testbed for new schemes of beam combination. This will likely require re-

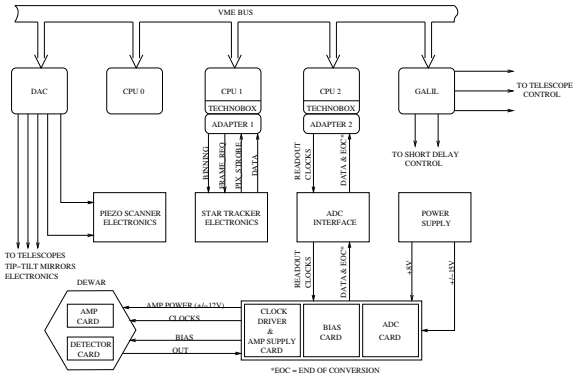

Fig. 5.1.— Control system block diagram at IOTA. The three CPUs manage different functions of IOTA. CPU-2 is dedicated to data acquisition and fringe-tracking. The CPLD on the Technobox interface performs all the tasks necessary to the PICNIC camera operation.

configuration of the pixels being read, and the current camera readout scheme is well-suited to provide this flexibility.

5.2 Camera Electronics

5.2.1 The PICNIC Detector Array

The PICNIC focal plane array (Kozlowski et al. 2000; Cabelli et al. 2000) is composed of four 128×128 pixel quadrants of a HgCdTe detector which are addressed simultaneously and independently. The active area of each pixel is $(40\ \mu m)^2$. The PICNIC detector is an evolved version of the NICMOS3. Both detectors are hybrid devices : a small band-gap material (HgCdTe) on an insulator substrate (sapphire) interconnects through indium bumps to a silicon substrate, where circuitry for addressing the pixel and analog electronics are built. The quantum efficiency of the individual detectors is better than 50% for wavelengths in the range 0.8-2.5 μm. Our PICNIC camera is equipped with standard near-infrared broadband filters : J (1.11–1.39 μm), H (1.50–1.80 μm) and K′ (2.00–2.32 μm), as well as a variety of narrow-band filters within the those bands.

The main differences between the NICMOS3 and PICNIC arrays are in the silicon substrate (sometimes called the multiplexer). (a) In an attempt to reduce the effects of noise caused by resetting pixels in the array (reset anomaly), PICNIC has a line by line reset instead of a pixel by pixel reset. (b) The LINE and PIXEL clocks (cf. Section 5.2.5) used to address the pixels of the detector are both double-edged for the PICNIC detector whereas they are single edged in the NICMOS3. (c) The output source follower, used to read the pixels in the PICNIC array, can be turned off when not in use in order to decrease the effects of the output source follower glow. (d) In the NICMOS3 array it is possible to address each quadrant separately, but for PICNIC

a single set of bias, clocking and output lines are available to the user and the four quadrants must be operated in parallel.

5.2.2 Analog Electronics

The analog electronics of our new PICNIC camera are identical to the electronics used in the IOTA NICMOS3 camera (Millan-Gabet 1999; Millan-Gabet et al. 1999a), with the exception of the printed circuit board (PCB) on which the detector itself is mounted (since the PICNIC and NICMOS3 carriers are not pin-to-pin compatible).

Our NICMOS3 analog electronics design was very successful in avoiding noise induced by the digital circuitry. All digital signals and ground arriving from the outside world are de-coupled from the camera analog electronics by using opto-isolators. The PCBs are carefully designed to separate the local digital ground of the opto-isolators from the analog ground. Separate digital and analog ground planes were laid out around digital and analog components in order to shield out interference from the switching of the opto-isolators and other digital circuits. Both grounds are connected to the metal chassis at a single point to avoid ground loops. All the interconnection cables to and from the dewar are shielded to avoid electromagnetic interference.

Nevertheless, in the new camera and in the new laboratory environment that resulted from the substantial upgrades made to most of our sub-systems, we experienced some interference problems, attributed mostly to the delay lines' power electronics and to a lesser extent to VME real-time control system rack. After these problems were solved we were left with some residual, high frequency noise, increasing the camera noise to about 20 electrons. This, we discovered, was due to a bad ground network which was injecting noise into the camera. A solution which we found viable was to protect the sensitive electronics with a choke wound around a ferrite bead, connected in series to the ground connection of the PICNIC camera. This solution, although not ideal, eliminated this source of noise.

5.2.3 CPLD Technology

A digital circuit is built by connecting several devices which perform logic functions. Such devices usually provide standard functions of different complexities, starting from simple logic functions such as Small Scale Integration (SSI) and Medium Scale Integration (MSI) Transistor-Transistor Logic (TTL) devices and ending in high performance full custom designs such as microprocessors and random access memories. Full custom design requires years of development and test and is used when high volume production is required.

CPLDs and FPGAs (Field Programmable Gate Arrays) permit the implementation of complex digital circuits on a single chip. CPLDs tend to have faster and more predictable timing properties, while FPGAs offer the highest gate density (Hamblen & Furnan 2000). The number of gates in the chip is on the order of hundreds of thousands and this number is increasing rapidly while the technology improves.

In the Altera Flex-10K70, used in the PICNIC IR-camera at IOTA, gates can be interconnected to form complex networks using electronic switches; the switch interconnections are stored on a static RAM, so the interconnection among elements can be changed in just milliseconds. This means that a single component can host several circuits performing very different functions at different times.

We developed our circuits on a commercially available PCI-PMC[1] card which contained an Altera 10K70 CPLD. This card plugs directly into the PMC connectors of our CPUs. The advantage of this configuration is being able to load a new circuit in the CPLD from the CPU memory or from the disk during operation. The disadvantage of this configuration, as we discovered, is in forcing outputs to be be assigned to specific components and I/O pins. The compiler prefers that the pins are freely assigned the first time it builds the circuit, in order to optimize the routing of signals. Fixed output pins likely add delays to the circuit which makes it failure prone at higher speed. Another disadvantage of using a PMC interface is the impossibility of using an oscilloscope probe on the component; also the real time debug tools which permit the physical testing of the timing on the component can only be used with the ALTERA programming interface and software, complicating the debugging process.

5.2.4 The VxWorks Real-Time System

The new control system for the IOTA interferometer is centralized in a VME type computer. VME is an industrial standard defining the mechanical and electrical characteristics of a computer bus, oriented to instrumentation control. CPUs based on different processors can be plugged into the bus.

Real-time means that the different tasks are executed at very precise intervals in time, synchronized by a "real time clock" which defines the pace of the system. This is crucial for instrument control (in our case controlling visible and IR cameras, telescopes, delay lines, fringe trackers and data storage).

The VxWorks system is UNIX hosted, meaning that all the development can be done on a UNIX computer, using standard cross-compilers (GNU) editors, etc. UNIX is not per-se a real time system. The UNIX computer host (in our case a SUN Blade-1000) is connected to the VME rack through a fast optical link and communicates with three CPU targets. The SUN host loads the compiled programs on the targets and these programs (tasks) are executed using the VxWorks operating system, which is basic and streamlined, but allows us to use standard UNIX sockets to communicate with UNIX based workstations, file-servers, etc. with a standard Ethernet connection.

---

[1] A card based on an interface electrically identical to a standard PCI bus used in personal computers but implemented with a different type of connectors (following the PMC standard definition). This card connects the CPLD to the CPU card.

5.2.5 Clocking the Detector

The detector matrix is addressed through two shift registers The vertical shift register for lines is controlled by the [LINE , FSYNC] clocks. The horizontal shift register for pixels is controlled by the [PIXEL, LSYNC] clocks. FSYNC and LSYNC act as reset for the shift registers (active low) : when they are asserted the respective registers are loaded with all ones. The LINE and PIXEL clocks are double edge clocks. The first rising (or falling) edge connects the line or pixel circuitry to the output of the detector ; the second falling (or rising) edge will put a zero in the first bit of the corresponding shift register. Each of the following clock edges will shift the zero by one position (bit) in the register ; the zero bit will enable an analog switch to read the corresponding line and pixel of the detector.

Before reading the detector the pixels must be connected to the bias potential, in order to charge the junction capacitance (reset). The PICNIC multiplexer resets a whole line at a time (an important improvement in speed and performance compared to the NICMOS3 detector, where the pixels were reset one at a time) by asserting the RESET clock (active high) together with the LINE clock.

After reset, the reset bias voltage appears across the detector pixels. Subsequently, photo-electrons are generated and the voltage decreases linearly with incident flux, until the pixel voltages are zero, at which point the array is *saturated* and needs to be reset again in order to be responsive. A variety of clocking methods are possible for measuring the incident flux integrated during a given time. Two such methods will be described below, but in general always involve resetting the array or pixels of interest and then differencing the (amplified and digitized) output voltages corresponding to two consecutive reads separated by the integration time.

5.2.6 Implementation of the Quadrant Readout Mode

Although the camera's principal use is reading out a small number of pixels illuminated by the beam combiner, it is necessary to read a whole quadrant for optical alignment purposes. Moreover, in this mode the camera could be used as an IR wavefront tip-tilt sensor, to track sources which are too faint at visible wavelengths to be observed using our current CCD-based system. A block diagram of the CPLD circuit in quadrant mode is shown in Fig. 5.2.

Correlated Double Sampling

In correlated double sampling (CDS) mode, adopted for quadrant readout, the detector is reset, sampled (reset frame), allowed to integrate and re-sampled (image frame). The difference between the reset and image frames is then recorded. This is the basic operational mode of the NICMOS3 and PICNIC detectors, both of which are integrating detectors, with non-destructive readout. CDS is implemented entirely in the CPLD electronics. The CPU receives a buffer containing the final, ready to use, data. Unless otherwise stated, in this paper we will use the term “read” to mean

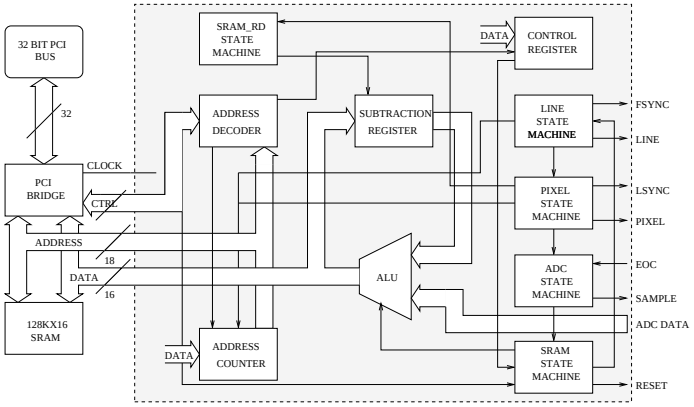

Fig. 5.2.— The PICNIC quadrant readout circuit. Five state machines are responsible for the operations of the camera. Complex functions are broken into elementary functions of clocking lines, pixels, resetting the detector, commanding the ADC and transferring data into SRAM, each executed by a single state machine.

a CDS read cycle.

Circuit Implementation

The quadrant image read is stored in the static RAM (SRAM) on the Technobox PCI-PMC card, which is shared between the CPU and the CPLD through the PCI bus. The readout starts when the start bit in the control register of the CPLD is asserted by the CPU. The interrupt line (INTA) is asserted when the readout process has finished and a frame is present in the SRAM.

Between these events, many operations are handled in parallel by state machines which have been built into the CPLD. These state machines are as follows.

1. SRAM state machine, which handles communications with the PCI bridge for bus arbitration. It polls the start bit of the control register and sets a semaphore which starts the LINE state machine. When a reset frame and an image frame have been acquired and subtracted, it releases the PCI bus and asserts INTA.
2. LINE state machine, which controls the FSYNC and LINE clock generation for the PICNIC array. Once a line has been selected it sets a semaphore to start the PIXEL clock generation ; lines are counted by the line counter. It will also assert the RESET line, together with LSYNC if the toggle flip-flop, which keeps the state of the frame (reset-frame or data-frame), is set on reset-frame.
3. PIXEL state machine, which controls the LSYNC and PIXEL clock generation for the PICNIC array. It controls the sequence of clocks and sets a semaphore when the analog to digital converter (ADC) can sample the selected pixel ; pixels are counted by the pixel counter.
4. ADC state machine, which controls the ADC. If the toggle flip-flop is in reset frame state, then the ADC state machine sends a start of conversion pulse to

the ADC, waits for the end of conversion signal from the ADC, and writes a word of data in the static RAM. If the toggle flip-flop is in data-frame state, then the ADC state machine stores the difference between the data word at the current SRAM address and the data word obtained from the ADC. The SRAM address is obtained by combining the line counter and pixel counter.

5. READ-SRAM state machine, which reads one word of the reset frame previously written to SRAM, during the ADC conversion. This operation is carried out in parallel with the ADC data conversion. The data previously stored in memory, and addressed by the ADC state machine, is recovered and stored in a temporary register. This value will be used to calculate the difference between the reset value and the current value obtained from the ADC converter.

The data acquisition (DAQ) scheduler task, running on the CPU when in quadrant mode, loads the circuit into the CPLD and initializes the readout parameters. The start bit is then asserted in the CPLD control register, the state machines are started and the controller runs in a loop until a whole quadrant is acquired.

Readout Parameters

A number of readout parameters can be changed by the application running on the CPU by accessing the registers on Altera. The registers are as follows.

1. T_{base} is the PICNIC base clock period. The 33 MHz PCI clock is divided by a programmable counter built into the CPLD, in order to generate the base clock rate used to clock the PICNIC array ; the counter can be programmed by the CPU through the PCI bridge. A typical value is 1 μs.
2. T_{del} is the delay between the PICNIC clock and the sample assertion to the ADC. This delay is necessary to avoid sampling the addressed PICNIC pixel before it has settled. The delay is generated by a programmable counter and is accessible to the CPU through the PCI bridge. A typical value is 4 μs.
3. T_{int} is the integration time. This is also a presettable counter which determines the time between the reset frame and the image frame. A typical value is a few ms.
4. (N_x, N_y) is the sub-quadrant corner position in units of pixels (cf. Sec. 5.2.7). With these variables it is possible to define a small area of the detector. This flexibility will be crucial when implementing an IR wavefront tip-tilt sensor.

5.2.7 Implementation of Interferogram Detection Mode

This mode reads a number of pixels located at arbitrary coordinates on the PICNIC array, for detection of interference fringes. In practice, for better clocking efficiency and noise performance the pixels should be closely spaced and, preferably, on the same line. A block diagram of the CPLD circuit in interferogram detection mode (also sometimes called scan mode) is shown in Fig. 5.3.

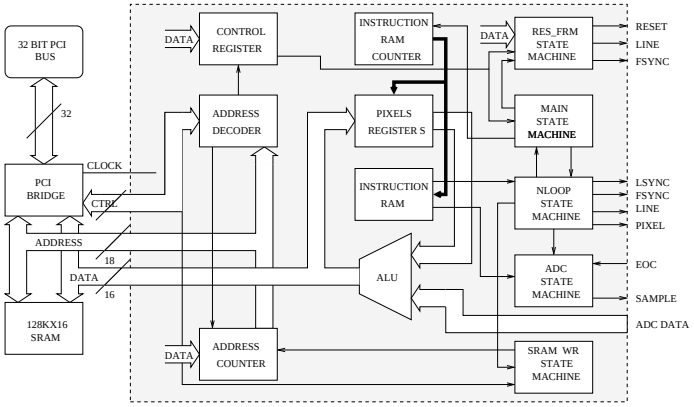

Fig. 5.3.— Block diagram of the PICNIC camera in interferogram detection (scan) mode. The basic functions are implemented with five state machines. The pixel readout sequence is stored in the instructions RAM, internal to the CPLD. This RAM stores micro-coded instructions specialized to generate clocks sequences for the PICNIC array.

Fringe Detection and Sampling

A brief description of how interferograms are produced at the IOTA is required before we describe our sampling method.

Starlight collected by each telescope enters a vacuum enclosure (in order to avoid chromatic dispersion) as afocal beams of 45 mm diameter. The change of optical path introduced by the sidereal motion of the star is compensated by sending the beams from two of the telescopes to two separate delay lines. After the delay system, the telescope beams exit the vacuum and enter the beam combination laboratory, located at the center of the array. For near-IR science operation, three dichroics transmit visible light towards the wavefront tip-tilt sensor, and reflect near-IR light into the beam combination table.

Three-way beam combination at the IOTA was first achieved using the H-band integrated optics component, IONIC-3T, developed by the IONIC collaboration in Grenoble[2] (Berger et al. 2003). In the following, we refer to this setup, and show sample data obtained with it.

Near-IR light is directed towards three flat steering mirrors and then three off-axis parabolas, which focus the three beams into three fibers feeding the IONIC-3T component. In this component, each input is first divided into two parts. Interference then takes place pair-wise inside the component, resulting in six output beams comprising three complementary pairs. Each output interferes the light from a pair of telescopes. The six output beams are then focused onto six separate PICNIC pixels. The interference fringes are recorded while two of the dichroics are piezo-driven to scan a path of 100 μm and 50 μm in order to modulate the optical path difference

[2]The IONIC project is a collaboration between LAOG, LETI and IMEP, Grenoble, France.

(OPD). A scan typically contains 256 data points.

Differential Sampling

With this method, adopted in fringe detection mode, the array is reset only once, at the start of each scan, then the pixels of interest are sampled continuously as they discharge. Each data point in the scan is the difference between consecutive samples, and the integration time per data point is set by the time needed to sample each target pixel, possibly multiple times, as described below. Avoiding the array reset for every data point reduces the noise, and increases the readout speed, but at the expense of dynamic range.

Circuit Implementation

The digitized pixel voltages are stored in SRAM. INTA is asserted at the end of every group of pixels which are read out. INTA is used to delimit the end of a data frame but it is also used to step the piezo OPD scanner which is synchronous with data acquisition. This simple cycle is executed once per data point (e.g., 256 times per scan) and stored in memory as a time sequence. When one scan is finished a flag is asserted in the control register and the CPU transfers the stored vector to a buffer.

Following the same methods implemented in the previous NICMOS3 camera, each time a pixel is accessed it can be sampled several times and the values added and stored in a register ; we call this *reads*. It is also possible to read the whole group of pixels and sum the values separately ; we call this *loops*. By averaging the $N = loops \times reads$ samples, the readout noise is ideally reduced by the factor $\sqrt{N}$. Using many reads achieves a better SNR but increases the latency between sampling different pixels ; using many loops degrades slightly the SNR since it involves clocking the detector, which adds noise, but the time delay among different pixels is reduced. In practice, we choose combinations of reads and loops which are compromises between those two effects.

The hardware implementation of this function is as follows. Data for each pixel must be stored in separate registers and added there, then data is transferred to SRAM and INTA is sent to the CPU through the PCI-bridge. The interrupt must be cleared by the CPU at the end of this process. To limit access to the SRAM and avoid conflict with the CPU, the data is double-buffered in the internal registers, rather than using the SRAM, as is done for the quadrant readout. This unfortunately limits the number of pixels that can be read to nine, since generating internal memory in the CPLD is intrinsically inefficient. This limitation will become important when spectral dispersion is implemented (Ragland et al. 2002) or if polarization splitting is desired, and will be removed in future versions of the CPLD circuit.

The interrupt generated from the CPLD, in addition to informing the CPU that a new data point is available in the SRAM, is also used for stepping a sawtooth modulation of the OPD. This modulation is necessary for acquiring data in fringe mode. The pixel registers, the adders used to integrate the value of the pixels, the

counters which count the number of data points transferred, the SRAM address, the internal RAM address and clock generation are all controlled, as represented by the block diagram shown in Fig. 5.3, by the five following separate state machines.

1. RES_FRM_PROCESS state machine : resets the whole PICNIC array continuously, clocking lines from 0 to 127 and back to zero. This process is stopped when the start flag is asserted and the main process is idle.
2. MAIN state machine : schedules the N_LOOP_PROCESS state machine and increments the address of the instruction internal RAM which contains the readout sequence transferred from the CPU. It starts when the start bit of the control register is asserted ; it clears all registers and starts the loop state machine. It ends when the loop_tc semaphore is asserted.
3. N_LOOP_PROCESS state machine : is scheduled by the main process and decodes the instructions which then generate the detector clocks. These instructions are written in the internal RAM. The internal RAM is loaded by the CPU via the DAQ scheduler program. It schedules the SAMPLE_PROCESS and the SRAM_WR_PROCESS. The LINE, FSYNC, PIXEL and LSYNC clocks are generated by this state machine.
4. SAMPLE_PROCESS : sends start of conversion to the ADC, waits for the end of conversion signal from the ADC, and writes a word of data to the internal register corresponding to the pixel sampled. If the requested number of reads is greater than one, then the state machine reads the ADC several times and the values are accumulated in the corresponding pixel register.
5. SRAM_WR_PROCESS : executes the data transfer to SRAM from the internal registers when the requested loops and reads are completed. When the sequence starts again to sample a new data point it executes in parallel, transfers the data from the pixel registers to SRAM and sends an interrupt when the process is completed.

Micro-coded Instructions

Instruction	Hex Value	Action
fsync	02	FSYNC pulse generated
lsync	03	LSYNC pulse generated
line	00	LINE clock transition n-times
pixel	01	PIXEL clock transition n-times
jump	04	Jump to program location

Table 5.1: CPLD micro-coded instructions used to generate scanning sequences in interferogram readout mode.

It is highly desirable to have the flexibility of choosing which pixels are sampled in order to use different combiners. For this reason the scanning sequence has to be

alterable. This was solved by allowing the state machines to change state according to a program written into a RAM internal to the CPLD. Five instructions can be executed by the state machines as shown in Table 5.1. These instructions generate a clock sequence ; the LINE clock will change level n-times according to the value of the following byte in the program. The same happens with the PIXEL clock, but in this case every pixel is read n-times, according to the value written in the N_{reads} register. Loops are achieved through the jump instruction which permits branching back to a specific instruction in the program. The loop is executed n-times according to the content of register N_{loops}. Arbitrary code for generating a clocking sequence is given in Table 5.2.

Addr.	Hex Value	Mnemonic
0 :	203 ;	– fsync + line 3
1 :	302 ;	– lsync + pixel 2
2 :	103 ;	– pixel 3
3 :	004 ;	– line 4
4 :	302 ;	– lsync + pixel 2
5 :	103 ;	– pixel 3
6 :	400 ;	– jump 00

Table 5.2: Arbitrary clocking sequence written using the instruction described in Table 5.1. The first instruction (address "0") resets the line register and clocks three lines down. The second instruction resets the pixel register and clocks two pixels to the right. The third instruction clocks other three pixels to the right. Then the detector is clocked down of other four lines and at address "4" the pixel register is reset and the pixel clocked two positions to the right. Then the pixel is clocked other three positions to the right and at address "6" the program jumps back at instruction "0' to restart the whole cycle again.

Readout Parameters

In the interferogram readout mode a number of parameters are user-selectable, as follows.

1. T_{base} is the same as in Section 5.2.6 for quadrant mode.
2. T_{del} is the same as in Section 5.2.6 for quadrant mode.
3. N_{loops} is the number of times that the specified pixel group is read. These values are summed in the pixels' registers. A typical value is 4 loops.
4. N_{reads} is the number of times that a specific pixel is read, per loop. It sums the values for that pixel, and puts the resulting sum in the corresponding pixel register. A typical value is 4 reads.
5. Readout sequence. This vector contains the readout instructions used to sample the pixels. The vector contains instructions which assert the lines LSYNC or

FSYNC for the detector as well as the LINE and PIXEL lines. Line and pixel instructions have arguments which specify the number of lines or pixels to clock the detector.

6. $N_{samples}$ is the number of samples of each group of pixels acquired and stored into memory. A typical values is 256.

Integration Time

Loops \ Reads	1	2	3	4
1	340	510	670	830
2	660	990	1320	1640
3	980	1470	1960	2450
4	1300	1950	2610	3270

Table 5.3: The integration time (μs) as a function of the number of loops and reads derived from Equation (5.1). These values agree with the experimental data at about the 3% level.

The integration time per sample can be accurately calculated by inspecting the digital circuit in the CPLD. Equation 5.1 relates the integration time to the digital parameters passed to the circuit.

$$T_{int} = T_{base} \cdot (N_y + 1) + N_{loops} \cdot [T_{base} \cdot (N_x + 1) + T_s + (N_{pix} - 1) \cdot (T_{base} \cdot N_{skip} + T_s)] \quad (5.1)$$

where

$$T_s = (10\ \mu s + T_{del}) \cdot N_{reads} \quad (5.2)$$

$$T_{base} = N_{base} \cdot 0.0303\ \mu s \quad (5.3)$$

$$T_{del} = N_{del} \cdot 0.0303\ \mu s. \quad (5.4)$$

Here N_x and N_y are the coordinates of the first pixel to be read, measured from the corner of the quadrant where the first pixel is $(N_x, N_y) = (1, 1)$, and N_x corresponds to the PIXEL clock, and N_y corresponds to the LINE clock. N_{skip} contains the spacing between pixels illuminated from the beam combiner. N_{pix} is the total number of pixel sampled (six). T_{base} is the base clock used to generate all the timings for the detector, the ADC, and the CPU through the assertion of an interrupt. It is derived from the system clock period (0.0303 μs), multiplied by the digital register value N_{base}.

A delay introduced before sampling the pixel is also produced in the same way, multiplying the system clock by the variable N_{del}. Other parameters are listed in Section 5.2.7. The integration time as a function of the number of loops and reads, calculated from (5.1) is listed in Table 5.3. The parameters used were, $N_{del} = 506$ (corresponding to $T_{del} = 15.3\ \mu s$), $N_{base} = 85$ (so $T_{base} = 2.6\ \mu s$), $N_{skip} = 5$, $N_y = 8$, $N_x = 34$. Table 5.3 is consistent at the 3% level with experimental measured data.

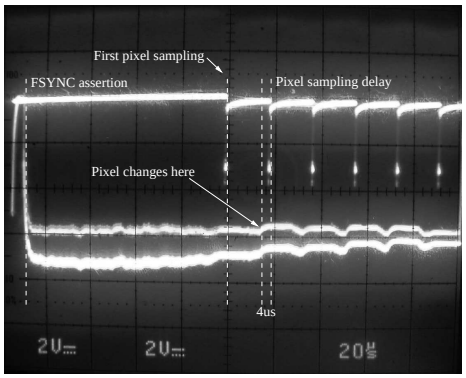

Fig. 5.4.— The sample command to the ADC and the analog output of the detector are shown in this oscilloscope plot. The time spent between the FSYNC assertion and the first sample signal is the time employed by the PIXEL clock to arrive to the designated pixel. The response of the detector is shown in the lower trace. Also shown is the delay time of 4 μs introduced to allow output settling prior to ADC sampling.

A typical clocking sequence is shown in Fig. 5.4. The oscilloscope traces show the sample commands to the ADC and the analog quadrant output. The settle and wait time T_{del} is also indicated.

5.3 Data Acquisition Software

The data acquisition software is composed of two main parts : (1) real time software running on the VME target CPU, written in C/C++, and (2) data visualization and command software, running on the SUN host computer, and written in IDL/C.

5.3.1 Real-time Software

This software comprises C libraries able to communicate with the CPLD device as well as software responsible for implementing data-acquisition and fringe tracking. The latter is also a new capability at the IOTA, responsible for sensing and servoing the delay locations of the fringe packets, which fluctuate rapidly with the atmospheric differential piston. The algorithm used to sense the fringe phase and the performance of this system will be described in detail in an upcoming publication (Pedretti et al. 2002, 2003)

The C libraries

The CPU is interfaced to the Altera CPLD using a PMC bus, as described earlier. The kernel of this library is given by the manufacturer of the card (Technobox). This is only an example which can be modified by the user according to the CPLD programming. The modules dealing with the PCI bridge and the remote programming

of the CPLD do not need any modification.

Two basic functions are associated with the library : (1) writing to the control register to modify the behavior of the CPLD, and (2) reading the static RAM and transferring its contents to a data buffer.

Fringe-tracking and Data Acquisition Software

The functions performed by this module are complex and numerous and they can be broken in these following groups.

1. Switch between quadrant acquisition and scan acquisition mode.
2. Transfer data from the CPLD SRAM to the target CPU RAM any time an interrupt is generated from the CPLD and the END_DATA flag is set in the CPLD control register, in quadrant or scan mode.
3. Generate the scanning ramp sent to the piezo mirrors through the programmable DAC card controlled by the target CPU ; every sample of the digitally generated sawtooth-like waveform is passed to the DAC card after an interrupt is received. Offsets generated by the fringe tracker are also added to this waveform.
4. Invoke the fringe tracker routine any time the data has been transferred to memory and send offsets to the delay line to compensate the slow drift of the optical path with time.

5.3.2 Data Display and Control Software

The main function of this software suite, written in the Interactive Data Language (IDL), is to provide a graphical interface to the user and send commands to the real-time system, in order to : (1) optimize the optical alignment of the system, (2) display in real time the data being acquired and the performance of the fringe-tracker, and (3) provide an interface for user selection of the parameters of the data acquisition and fringe-tracking systems.

An example of a frame acquired in quadrant mode is shown in Fig. 5.5, it depicts the six pixels illuminated by the IONIC-3T component outputs. Fig. 5.6 shows example interferograms obtained in fringe detection mode.

5.4 Detector Performance

5.4.1 Read Noise and Gain Measurements

The read noise was measured using the standard Poisson-statistics method (e.g., Millan-Gabet et al. (1999a)). A light source connected to an adjustable regulated DC power supply was used to provide varying degrees of illumination to the array. For each DC-voltage setting, we recorded scans identically as in science fringe acquisition mode, i.e., 1 loop, 1 read, 6 pixels, and 128 read cycles (129 samples). Two combinations of

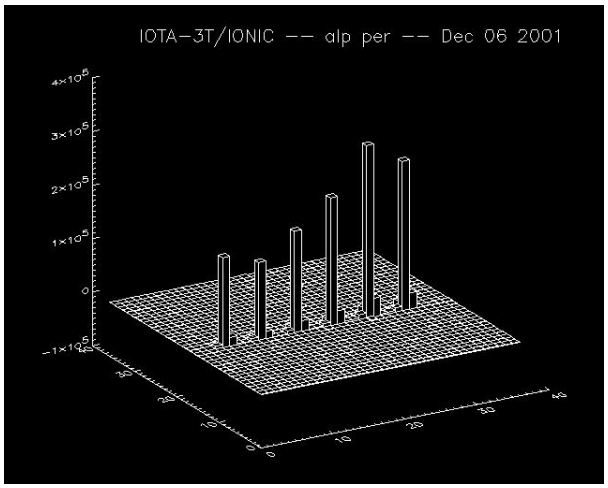

Fig. 5.5.— An example of frame showing the pixels illuminated by the six outputs of the IONIC-3T beam combiner, imaged in quadrant readout mode.

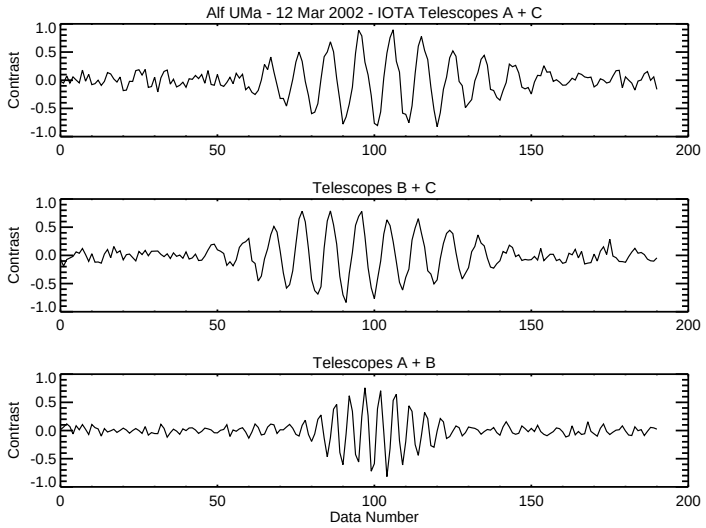

Fig. 5.6.— An example of H-band scans obtained using the CPLD interferogram readout circuit. These data were obtained using the IONIC-3T combiner (Berger et al. 2003). Complementary fringes for each telescope pair have been subtracted to enhance the SNR.

base clock speed (T_{base}) and pixel sample delay (T_{del}) were used, i.e., (2.5 μs, 15 μs) and (1.0 μs, 4 μs). The corresponding integration times are 310 μs and 130 μs per pixel. The 310 μs value was selected to be representative of a relatively slow readout ; on the other hand, the 130 μs value is the fastest readout speed that we have used, based on recommendations by Rockwell. The measured mean (adu) and variance σ^2 (adu^2) for each pixel are plotted in Fig. 5.7.

We assume that read noise from the detector and electronics, as well as the

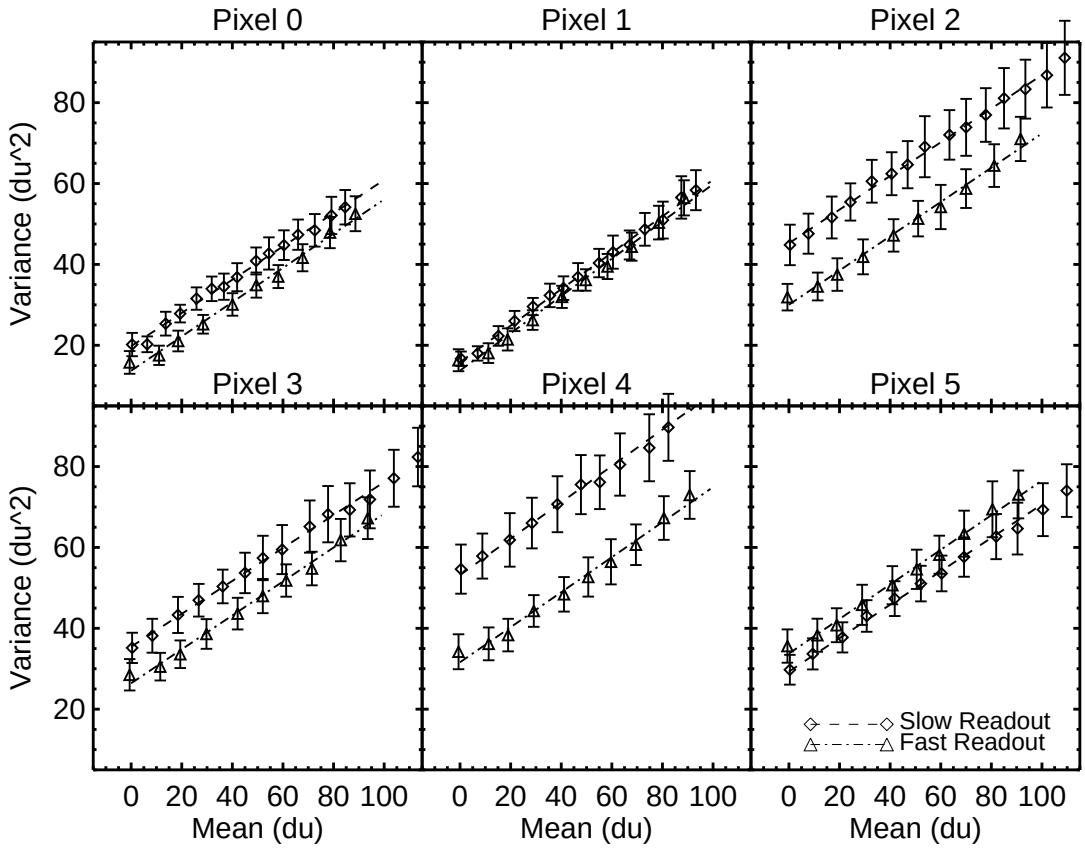

Fig. 5.7.— Variance vs. mean plot to measure system parameters. Data are plotted for six pixels sampled in interferogram mode. The two data sets in each plot were obtained for : (a) a slow readout mode (390 KHz PICNIC clock speed and 15 μs pixel sampling delay) and (b) fast readout (1 MHz clock speed and 4 μs pixel sampling delay). In each case, the slope provides the camera gain (elec/adu) and the y-axis intersect provides the read noise ; the resulting gain and read noise values are listed in Table 5.4.

photoelectron noise from the incident light beam, each have Poisson statistics. The gain g (elec/adu) is then the inverse of the slope of the variance vs mean curve. The read noise is derived from the variance intercept at zero mean. The results of these 12 experiments are shown in Table 5.4.

Gain

A number of conclusions on gain follow from Table 5.4. (1) The gain does not change significantly when the clocking speeds are changed, as might be expected for the reason given just above. (2) The gain values appear to vary slightly from pixel to pixel, with an rms scatter of 4% ; this is not too surprising, since the voltage change per electron at the detector pixel is the inverse of the capacitance, and this quantity could

Pixel	t_{int} (μs)	σ_{read} (elec)	g (elec/adu)
0	310	10.81 ± 0.26	2.43 ± 0.05
1	310	8.82 ± 0.17	2.22 ± 0.03
2	310	16.15 ± 0.27	2.40 ± 0.04
3	310	14.62 ± 0.25	2.46 ± 0.04
4	310	16.21 ± 310	2.22 ± 0.04
5	310	13.09 ± 0.24	2.42 ± 0.04

Pixel	t_{int} (μs)	σ_{read} (elec)	g (elec/adu)
0	130	8.74 ± 0.36	2.36 ± 0.08
1	130	8.04 ± 0.37	2.17 ± 0.07
2	130	12.93 ± 0.45	2.36 ± 0.08
3	130	12.25 ± 0.43	2.38 ± 0.08
4	130	12.98 ± 0.54	2.31 ± 0.09
5	130	13.58 ± 0.40	2.34 ± 0.07

Table 5.4: Results of read noise σ_{read} and camera gain g measurements. The noise is given per double read, given the differencing of consecutive samples intrinsic to our sampling method. Averaging over both integration times, the average read noise is $\sigma_{read} = 12.4 \pm 0.8$ elec and the average gain is $g = 2.34 \pm 0.03$ elec/adu.

easily vary slightly from pixel to pixel. (3) The gain values are nominally independent of pixel position, with a mean value of $g = 2.34 \pm 0.03$ elec/adu, where the uncertainty is the error in the mean.

Read noise

The corresponding conclusions on read noise are as follows. (1) The read noise is slightly higher for the longer integration time samples, i.e., 13.3 ± 1.1 elec for 310 μs integration, compared to 11.4 ± 0.9 elec for 130 μs; more experiments need to be done to see if this effect is real, and what its cause might be. (2) The read noise varies significantly from pixel to pixel, with an rms scatter of 22%; this suggests that it would be profitable to select an optimal set of pixels in future experiments, although in the present work no attempt was made to select particular pixels. (3) The read noise has a mean value of $\sigma_{\rm read} = 12.4 \pm 0.8$ elec, where the uncertainty is the error in the mean; the $\sigma_{\rm read}$ value refers to the rms variation in the difference of two successive reads, so the single-read rms value may be inferred to be smaller by $\sqrt{2}$, giving $\sigma_{\rm single-read} = 8.8 \pm 0.6$ elec.

5.4.2 NICMOS3 and PICNIC Comparison

Read noise

It is instructive to compare the performance of our previously-developed NICMOS3 system (Millan-Gabet et al. 1999a) with that of the PICNIC system as presented in this paper. When we embarked upon the upgrade from NICMOS3 to PICNIC, we did so in part because the latter was expected to have an unspecified but nevertheless somewhat smaller read noise than the former. We note that the amplifier electronics design is basically the same for both systems, although there are several small differences, and in any case, the readout systems are physically distinct, i.e., we use separate electronics. From the NICMOS3 paper we quote a read noise of 24.6 electrons per difference of two successive reads, in the readout mode normally used for fringe detection, i.e., using loops and reads to access the two output pixels. The corresponding read noise for the present PICNIC system, as discussed above, is 12.4 electrons per difference of two successive reads, in normal fringe-readout mode where loops and reads are used to access (in this case) six pixels. *Thus the PICNIC system has a smaller read noise by a factor of 2.0.* This improvement is likely due to the chip itself as well as improvements in our electronics, but since the chips are clocked differently, we could not use the same electronics for both chips, and therefore we cannot determine what part of the improvement is due to the chip itself and what part is owed to the electronics.

Clocking speed

PICNIC clocking is faster than NICMOS3 clocking, for several reasons. Faster clocking indirectly helps to reduce noise in a given amount of observing time because more reads per second (see Sec. 5.4.3) produces lower net noise per second. (1) The pixel clock in PICNIC triggers on both the rising and falling edges of the clock waveform, whereas in NICMOS3 the trigger was only single-edged. The gain is a factor of 2 in clocking along the pixel (x) direction. (2) The PICNIC clock is faster than the NICMOS3 clock, 1 MHz vs 0.3 MHz, giving an additional faster of 3 gain in speed.

5.4.3 Noise Reduction with Multiple Reads

We also measured the reduction of read noise with multiple sample averaging. We recorded 128-sample data sets with no illumination on the detector under various readout modes, from 1 to 16 reads per sample. Dark current as well as a possible background light leakage would contribute extra counts and associated variance to the data with longer integration times, so to remove this effect we computed the mean value (in electron units) of each scan, and subtracted this value from the variance (also in electron units) for each scan. The remaining amount of variance is then attributable only to the action of reading each pixel, and the square root of this value is the rms read noise.

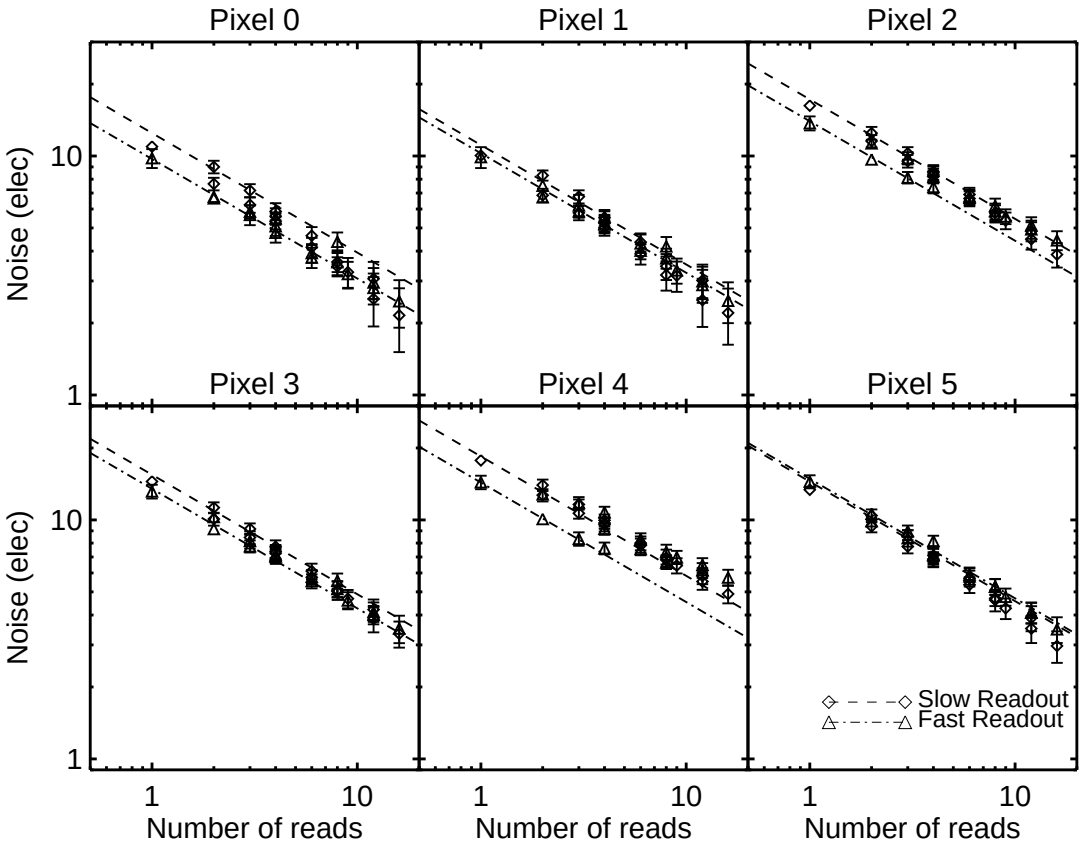

Fig. 5.8.— PICNIC camera measurements of scan rms versus number of reads, under zero illumination, for six pixels read in interferogram mode. As can be seen, noise reduction follows closely the ideal relation ($noise \approxeq 1/\sqrt{reads}$) plotted in dashed-lines.

In Fig. 5.8 we show these rms read-noise values as a function of the number of reads. Data for both the slow (310 μs) and fast (130 μs) readouts are shown, and both give similar results. For each data set, a linear fit with slope of $-1/2$ is shown, which is the slope expected if the rms read noise were to decrease as the inverse square root of the number of reads. Thus the data shows that the effective read noise can indeed be reduced by making more reads, and that this technique works well up to at least 16 reads. Therefore to improve the quality of a stellar observation, it is always best to make as many reads as possible, consistent with other constraints such as the atmospheric coherence time (for poor seeing conditions) and the saturation time of the detector (for bright stars). This result for our PICNIC detector is in agreement with that previously found for our NICMOS3 detector (Millan-Gabet et al. 1999a).

5.4.4 Magnitude Limit

Although the present paper is devoted to the PICNIC camera and electronics, it is nevertheless worthwhile mentioning briefly how the camera performs at the IOTA interferometer. A complete discussion of the performance of IOTA with IONIC-3T and PICNIC will be presented in a separate publication.

In (Millan-Gabet et al. 1999a) we demonstrated that IOTA was able to make useful measurements at H-band on a star with $H = 6.9$, which was effectively the limiting magnitude. The system components at that time were the IOTA 2-telescope interferometer, a classical beam combiner (i.e., no fibers), and our NICMOS3 camera.

Recently we made a comparable-quality measurement of simultaneous interferograms in H-band on a star with $H = 7.0$, which is very similar to our previous magnitude limit. The system components in this case were the IOTA 3-telescope interferometer, the IONIC-3T beam combiner (using single-mode input fibers), and the PICNIC camera described in the present paper.

Several gain and loss factors enter in to a comparison of limiting magnitudes in the two cases, as follows.

Regarding losses, the new system has only one-half the amount of light per detector pixel compared to the old system, owing to the extra split required in order to combine the light from a given telescope with that of two (instead of one) other telescopes. Another potential loss could occur with the new system because we are focusing the star onto a relatively small single-mode fiber instead of a relatively large detector pixel, a potential factor of about 0.7 reduction in star flux. Yet another loss might occur due to the finite transmittance of the new (IONIC-3T) beam combiner, which in the lab has a measured throughput of about 0.6.

Regarding gains, the new system has a measured noise level which is lower than in the old system by a factor of about 2.0 (cf. Sec. 5.4.2). Also, the new system can be clocked faster (cf. Sec. 5.4.2), so we can make up to about 6 times more reads per unit time, and therefore achieve up to a factor of 2.4 lower noise. In addition, in the new system we replaced the aging coatings on the siderostats and secondary mirrors of the two original telescopes, for an unknown gain, perhaps a factor of 1.5.

On balance, we see that the potential loss factor is roughly 0.2, but the gain factor is roughly 7, for a net gain factor of 1.4, although this value is relatively uncertain. In fact, we did achieve a slightly fainter limiting magnitude with the new system, so in a rough sense we have validated the gain calculations. More importantly, the value of this gain/loss calculation is that it points out areas where we might achieve yet further gains, for even fainter limiting magnitudes.

5.4.5 Non-standard Behaviors of Camera

There are several areas in which the camera system performs in a non-ideal fashion, as follows.

CPLD Spikes

We observed that our data had frequent and strong spikes superposed on it when the room air temperature near the CPLD was greater than about 70 F (21 C). The spikes were quasi-periodic, and their frequency of occurrence increased monotonically with temperature above this critical value. At worst, there was a spike for every few pixels. The temperature of the CPLD itself was well above room temperature, since it was mounted on top of the CPU of a single-board computer, and was in a card cage slot next to another CPU. The solution is simply to keep the room relatively cool.

Settling Time After Reset

After a frame reset, we found that the voltage on any pixel was not usable for photometry for a time period of about 50 ms. What we saw during this time was a voltage waveform which looked approximately like a capacitor charging curve, with a superposed oscillation of smaller amplitude. After this time, the pixel voltage followed the expected behavior, i.e., a nearly linear ramp, with slope proportional to incident light intensity. The settling time may be due to our electronics, but we have not yet located the root cause.

Pixel Interaction

We focused a bright star on a target pixel, and noted that the resulting signal was nearly constant in time, as expected, until the pixel well was depleted; after depletion the signal was essentially zero, again as expected. (In our case the full well was about 145,000 elec.) However when we sampled the adjacent pixel in the same row, we saw an opposite behavior, with a small constant signal prior to saturation of the target, followed by an increased constant signal after saturation. The magnitude of the increase was roughly 15% of the target signal. We did not explore this behavior thoroughly, but in the cases we did examine, it appeared to be robustly repeatable. The cause is not known.

5.5 Conclusion

We describe a new CPLD-controlled infrared camera for the IOTA interferometer. The CPLD architecture allows on-the-fly reconfiguration of the readout circuit to achieve different functions on the same hardware. Typical read-out modes include full quadrant, sub-array of quadrant, single pixel, a set of pre-selected pixels, etc., and all of these with a wide range of timing options. This architecture allows fast and stable clocking of the PICNIC array, resulting in faster and lower-noise readout. Faster readout has the significant advantage of being able to sample many more times for a given fringe frequency, thereby improving the readout noise, SNR, integrity of the interferograms in the presence of atmospheric piston, and ultimately the calibration of visibility amplitudes and phases.

In fringe detection mode, the measured rms readout noise for a single read of the detector is $\sigma_{\rm single-read} = 8.7 \pm 0.6$ electron. In normal readout mode the difference of two successive reads is larger by $\sqrt{2}$, giving $\sigma_{\rm read} = 12.4 \pm 0.8$ elec. With M multiple reads of a given pixel, the read noise averages down as $\sigma_{\rm M} = \sigma_{\rm read}/\sqrt{\rm M}$, for at least the range $1 \leq {\rm M} \leq 16$, showing that fast, multiple reads significantly improve performance in the PICNIC detector. Coupled to the recently-installed IONIC-3T integrated-optics three-beam combiner at IOTA, we have successfully measured triple interferograms on stars as faint as $H \simeq 7$. With this level of sensitivity, IOTA can extend its two-telescope programs, on evolved stars and young stellar objects, to imaging mode using three telescopes.

Acknowledgments

We thank the Altera Corporation for providing the CPLD development software through the Altera University Program. We are grateful to Kadri Vural, Craig Cabelli, and Mark Farris at Rockwell Scientific for their generous help with the NICMOS3 and PICNIC detectors. We thank Dr. Sebastien Morel for writing an early version of the data acquisition code. The IONIC project is a collaboration among the Laboratoire d'Astrophysique de Grenoble (LAOG), Laboratoire d'Electromagnetisme Microondes et Optoelectronique (LEMO), and also CEA-LETI and IMEP, Grenoble, France. The IONIC project is funded in France by the Centre National de Recherche Scientifique and Centre National d'Etudes Spatiales. This work was supported in part by grant NAG5-4900 from NASA, by grants AST-0138303 from the NSF, and by funds from the Smithsonian Institution. This research has made use of NASA's Astrophysics Data System Bibliographic Services.

Chapitre 6

Suivi de Paquet de Franges à IOTA

Pedretti, E., Millan-Gabet, R., Monnier, J. D., Traub, W. A., Carleton, N. P., Berger, J., Schloerb, P., Brewer, M. K., Ragland, S. & Lacasse, M. G., 2003, *à soumettre à PASP* .

Résumé

Nous décrivons le système de suivi de paquet de franges utilisé pour égaliser les chemins optiques des trois bases de l'interféromètre infrarouge IOTA (infrared optical telescope array). Les mesures de clôtures de phases, maintenant possibles avec trois télescopes, requièrent l'obtention simultanée de franges sur les trois bases. Ceci est accompli de la manière suivante : a) nous utilisons d'une part un nouvel algorithme basé sur l'interférométrie de Fourier double (DFI) pour obtenir la phase des franges en fonction de la longueur d'onde et d'autre part sur un algorithme de suivi de groupe pour déterminer la position du paquet de franges. Aucun matériel spécialisé n'est nécessaire pour opérer le suiveur de paquet de franges. Nous utilisons la caméra science comme senseur de franges ainsi que l'actuateur piezo et la ligne à retard pour minimiser la différence de chemin optique. b) Nous utilisons une technique appelée "baseline bootstrapping" laquelle permet de suivre en aveugle les franges très peu contrastées d'une des trois bases du moment que les franges détectées sur les deux autres bases présentent un bon rapport signal à bruit. c) Nous utilisons une simulation numérique pour montrer comment l'algorithme que nous utilisons peut retrouver un paquet de frange en dehors du domaine de balayage alors que seuls les lobes secondaires de l'enveloppe de cohérence sont visibles. d) Nous remarquons que le suiveur de paquet de franges est toujours capable de corriger la différence de chemin optique lorsqu'un filtre étroit est utilisé et que le paquet de frange est plus large que le domaine de balayage. Dans ce cas, une erreur additionnelle est introduite (aliasing). e) Nous confirmons que le bruit dans le spectre de puissance dans les données de la caméra infrarouge augmente avec la fréquence d'échantillonage et que cet effet est dû à la dérivation des données collectées appliquée pour l'extraction des interférogrammes.

Nous déterminons une expression pour ce bruit qui est utilisée pour le supprimer a posteriori pendant la réduction des données. f) Nous déterminons une expression qui relie l'erreur sur la mesure du chemin optique au nombre de photo-électrons détectés par la caméra infrarouge et au temps de cohérence de l'atmosphère, et comparons cette expression théoriques aux valeurs mesurées. g) Nous démontrons que l'algorithme de suivi de paquet de franges réduit efficacement les variations atmosphériques et instrumentales de chemin optique basses fréquences, laissant uniquement un bruit de phase qui sera traité a posteriori dans la réduction des données de clôture de phase. h) Nous montrons qu'il est possible d'estimer le temps de cohérence de l'atmosphère τ_0 lorsque le paquet de frange est balayé en un temps inférieur au temps de cohérence lui-même et que les données sont collectées en boucle servo ouverte.

Introduction

Les observations faites depuis la Terre, avec des interféromètres à longues bases, dans les longueurs d'onde visibles et infrarouges souffrent de la turbulence atmosphéri– que. La turbulence réduit le contraste des franges puisqu'elle module la phase des franges d'interférence de façon aléatoire.

Deux solutions permettent de corriger les chemins optiques altérés par l'atmosphère : le coherençage et le cophasage.

Il faut pour maintenir deux télescopes en cohérence que la différence de chemin optique entre ces deux ouvertures soit toujours plus petite qu'une fraction de la largeur de l'enveloppe de cohérence (rapport entre le carré de la longueur d'onde d'observation et la largeur de bande spectrale).

Le cophasage est un peu plus difficile à obtenir puisque pour maintenir deux télescopes cophasés, il faut que la différence de chemin optique soit de l'ordre d'une fraction de longueur d'onde. L'intérêt du cophasage est qu'il permet de longues poses pour l'acquisition de données, l'inconvénient est qu'il souffre d'un problème de saut de frange.

Dans cet article, je décris le suiveur de paquet de franges que j'ai développé pour l'interféromètre IOTA.

Après avoir étudié différents algorithmes pour le cophasage et le cohérençage d'interféromètres à plusieurs ouvertures, j'ai décidé d'appliquer l'expérience acquise au problème pratique du maintient de trois télescopes en cohérence. Lorsqu'IOTA ne possédait qu'une seule base, la position du paquet de franges était maintenue dans l'intervalle de cohérence manuellement par l'observateur. L'installation d'un troisième télescope a nécessité une augmentation du niveau d'automatisation de l'instrument puisqu'il devenait beaucoup plus difficile et quelques fois impossible d'assurer le suivi manuel des franges sur les trois bases simultanément.

Il ne m'a pas été possible d'appliquer directement mon travail sur le cophasage pour la construction d'un suiveur de franges pour l'interféromètre IOTA à cause d'une part du mode d'acquisition des données (IOTA est un interféromètre à recombinaison en plan pupille) et d'autre part du manque de moyen mécanique pour moduler

rapidement les franges.

J'ai conçu un nouvel algorithme qui apporte une solution fiable et efficace au problème de suivi de franges simultanément sur trois bases à IOTA, comme décrit dans l'article qui suit.

Fringe Packet Tracking and Coherence Time Measurement at the IOTA

Pedretti, E., Millan-Gabet, R., Monnier, J. D., Traub, W. A., Thureau, N. D., Carleton, N. P., Berger, J., Schloerb, P., Brewer, M. K., Ragland, S. & Lacasse, M. G.,
2003, *To be submitted to PASP* .

Abstract

We describe the fringe packet tracking system used to equalise the optical path lengths for the three baselines of the infrared optical telescope array (IOTA) interferometer. The measurement of closure phases, now possible with three telescopes, requires obtaining fringes on three baselines simultaneously. This is accomplished in the following way a) we use a novel algorithm based on double Fourier interferometry (DFI) for obtaining the phase of the fringes as a function of wavelength and a group delay tracking (GDT) algorithm for determining the position of the fringe packet. No specialised hardware is required to operate the fringe packet tracking subsystem. We use the science camera as a fringe sensor and the piezo scanners and the delay line to minimise the optical path difference (OPD). b) We use baseline bootstrapping, so that we are capable of blind-tracking fringes on a baseline when their signal-to-noise is very low, provided that fringes have good signal-to-noise on the other two baselines. c) We use numerical simulation to demonstrate how the algorithm can recover a fringe packet outside the scanning range when only the side lobes are visible. d) We remark that the fringe packet tracker is still capable of correcting the path when a narrow-band filter is employed during data acquisition and the packet is larger than the scanning range. In this case an additional error in the optical path is introduced, due to aliasing. e) We confirm that the noise in the power spectrum of the infrared camera data increases with frequency and that this effect is caused by the differencing of the collected data. We derive an expression for this noise which allows for the fitting and removal of it. f) We derive an expression which relates the error in the optical path to the photoelectrons detected by the infrared camera and to the coherence time of the atmosphere, and compare with the values obtained from experimental results.

g) We show that the fringe packet tracker algorithm effectively reduces the slowly varying atmospheric and instrumental-induced additional path, leaving the fast phase noise to be dealt within the post-processing closure-phase measurement. h) We show the ability of deriving the atmospheric coherence time τ_0 when the fringe packet is scanned in a time shorter than the coherence time itself and the data is collected with the servo-loop open.

6.1 Introduction

Observations performed with long-baseline ground-based optical/infrared interferometers are strongly affected by the turbulent atmosphere. Turbulence can reduce the visibility of fringes in many ways as described in Porro et al. (1999) for pupil-plane (or coaxial) beam combination and in Thureau (2001) for image-plane beam combination. Turbulence randomly modulates the phases of the fringes which can then become unusable for image reconstruction. Using three or more telescopes allows getting rid of the atmospheric phase contamination. This is done through the closure-phase technique pioneered in radio astronomy by Jennison (1958) and recently applied to long-baseline optical interferometry (Baldwin et al. 1996). The necessary condition for obtaining meaningful closure-phases is that the three fringe packets must be present in the same temporal interval. This is achieved by keeping the optical path difference (OPD) to a minimum.

There are two possible solutions for correcting the OPD in an optical or infrared interferometer affected by atmospheric and instrumental optical path errors : coherencing and cophasing. Coherencing relies on keeping the OPD between two telescopes within a fraction (about a wavelength) of the coherence envelope of the data (typically several to many wavelengths) and allows only short exposures to be taken. Cophasing intends to maintain the optical path within a fraction of a wavelength, allowing long exposures in the science beam ; however cophasing suffers from fringe jumps since it cannot find the position of the white fringe itself but needs a coherencing algorithm to know the central position in a fringe envelope.

IOTA has historically relied upon coaxial beam combination. With this method the optical path is temporally scanned through the fringe packet length. When IOTA only had two telescopes fringes were detected by a very sensitive single-pixel infrared detector or a detector array in which only two pixels were read (Millan-Gabet 1999; Millan-Gabet et al. 1999a). The number of pixels depends upon the beam combination scheme adopted. Several schemes are possible, and for IOTA, among others, we currently use the IONIC integrated-optics beam-combiner (Berger et al. 2003) which utilises six pixels of the detector for a three telescope beam combination. This technique as well as others used at IOTA, are discussed in Traub et al. (2003).

When IOTA relied on a single baseline the fringes were usually kept inside the scan interval manually by the observers. The installation of the third telescope at IOTA required an increase in the level of automation in the instrument, because manual tracking is not practical with three baselines to adjust. In particular the

requirement to measure closure-phases necessitated a system capable of keeping the fringe packets in the centre of the scan using the existing hardware dedicated to acquiring science data. Fringes must be acquired in the same coherence time in order to measure a closure-phase. A coherencing algorithm is very useful to localise the position of a fringe packet and correct the OPD in order to compensate metrology errors and atmospherically induced fluctuations in the optical path. This maximises the superposition of the fringe packets and the signal-to-noise-ratio (SNR) of the closure-phase signal when this is averaged in the complex plane as shown in Buscher (1988).

We present here a simple and fast algorithm, also independently discovered by Tubbs (1998), which uses DFI (Mariotti & Ridgway 1988) to extract wavelength dependent information from the fringe packet and calculate its group delay. This algorithm has the advantage of not requiring any extra hardware for providing fringe dispersion but utilises the science data as fringe sensor and uses the fringe-scanning piezo-mirrors for fast path correction. We can also use this algorithm for calculating the coherence time τ_0 of the atmosphere, when using the fringe sensor in open-loop mode. Other algorithms for fringe packet tracking which have been tested at IOTA are the subjects of separate publications (Thureau et al. 2003; Wilson 2003).

6.2 The Instrument

For an introduction to the IOTA interferometer and its recent science results see Traub et al. (2000, 2003), Mennesson et al. (2002), Chagnon et al. (2002), Berger et al. (2001), Kervella et al. (2001), Hofmann et al. (2002), Monnier et al. (2003a,b), Ohnaka et al. (2003), Millan-Gabet et al. (2003), and Weigelt et al. (2003).

The three beams arriving from the vacuum delay-line tank hit three dichroic mirrors which separate the visible and infrared light. The visible beam continues toward the star tracker servo system. The science infrared beam is reflected toward three flat mirrors and then three off-axis parabolas which focus the three beams on three single-mode (H-band) fibres feeding the IONIC-3T component.

Interference is achieved inside the integrated optics component, resulting in three output pairs π radians out of phase in intensity. The interference fringes are recorded while two of the dichroics are piezo-driven to scan a path of about 100 μm and 50 μm, respectively, in order to scan through the fringe packet in the three beams. The six combined beams are then focused on six separate pixels of the PICNIC array which serves as infrared science camera and fringe sensor for the fringe packet tracker. The path difference calculated by the packet-tracker is fed back to the piezo-scanning dichroics for a fast tracking response. The piezo scanners are off-loaded of their additional offsets every second, when a fraction of the error signal is sent to the short delay lines which are responsible for tracking the geometric delay caused by the rotation of the Earth.

6.3 Calculating the Fringe Position

6.3.1 Tracking the Fringe Packet Using Double Fourier Interferometry

Our method of fringe packet tracking at IOTA calculates the group delay of fringes dispersed with DFI, which is used to obtain the wavelength dependent phase from the fringe packet. This is done by scanning the fringe packet over an interval greater than the packet length, where the spectral resolution is proportional to the scan length. The GDT method has been applied to interferometry since the very beginning of the field, when Michelson & Pease (1921c) used a prism for dispersing and acquiring fringes visually at the 20-ft interferometer. Labeyrie (1975) used the same system and demonstrated fringe acquisition on a two-telescope interferometer. Several system have been proposed since then, for correcting the optical path (Vakili & Koechlin 1989; Rabbia et al. 1994). GDT (also called dispersed fringe tracking when applied to image plane interferometry) has been routinely used at several interferometric facilities (Robbe et al. 1994; Lawson 1995; Koechlin et al. 1996). In fact, at IOTA, GDT was selected as the original method of path difference monitoring, in the visible, but the system was set aside in favor of making infrared observations, and therefore was never extensively used (Nisenson & Traub 1987; Traub & Lacasse 1988; Traub 1990; Traub et al. 1990).

We will perform a derivation of the algorithm using the formalism used by Walkup & Goodman (1973). We can write the intensity as a function of the optical path ξ for a pupil plane interferometer as :

$$I(\xi) = I_s \left\{ 1 \pm V_s \frac{\sin\left[\pi\left(\xi - \xi_0\right)\Delta f\right]}{\pi\left(\xi - \xi_0\right)\Delta f} \sin\left[2\pi\left(\xi - \xi_0\right) f_0 + \phi\right] \right\} + I_b \tag{6.1}$$

where I_s and I_b are irradiances associated with the constant signal and background respectively, V_s is the signal-dependent contrast of the fringes, ϕ a generic phase, Δf the bandwidth of the used filter, f_0 the spatial frequency of the fringe, and ξ_0 is an additional optical path which shifts the fringes off-centre. This is the actual value we want to calculate in order to correct the optical path. It is more convenient to re-write Eqn. 6.1 as a function of the total intensity $I_t = I_s + I_b$ and the apparent visibility $V = I_s V_s / \left(I_s + I_b\right)$. The equation becomes :

$$I(\xi) = I_t \left\{ 1 \pm V \frac{\sin\left[\pi\left(\xi - \xi_0\right)\Delta f\right]}{\pi\left(\xi - \xi_0\right)\Delta f} \sin\left[2\pi\left(\xi - \xi_0\right) f_0 + \phi\right] \right\}, \tag{6.2}$$

which will be further simplified when the two complementary beams from the beam combiner are subtracted and divided by their sum, in order to reduce the photometric fluctuations, remove the constant intensity bias and normalise the intensity. The generic phase, ϕ is set to zero and the visibility to one, for sake of simplicity. After this operation we obtain,

$$I(\xi) = \frac{\sin\left[\pi\left(\xi - \xi_0\right)\Delta f\right]}{\pi\left(\xi - \xi_0\right)\Delta f} \sin\left[2\pi\left(\xi - \xi_0\right) f_0\right]. \tag{6.3}$$

We now need to estimate the phase of the fringes for the spatial frequencies in the bandpass. Our estimator will be the Fourier transform of the recorded-fringes temporal scan. Using the modulation theorem we obtain the Fourier transform $\widetilde{I}(f)$ as the convolution of two complex and opposite delta Dirac function $\pm\delta\left(f \pm f_0\right) i/2$ with the step function $\sqcap_{\Delta f}\left(f\right)$

$$\widetilde{I}\left(f\right) = \pm\frac{i}{2}\delta\left(f \pm f_0\right) * \sqcap_{\Delta f}\left(f\right) \exp\left(-i2\pi f\xi_0\right) \tag{6.4}$$

since the Fourier transform of a real function is Hermitian, the two sides of the transform are symmetrical. We can discard the negative part of the transform. The wavelength dependent phase is only meaningful inside the bandpass, where the signal-to-noise is high. We now select two frequencies, f_1, and f_2, both of which lie within the interval $\left(f_0 - \Delta f/2\,,\, f_0 + \Delta f/2\right)$. We can rewrite Eqn.6.4 as

$$\widetilde{I}\left(f\right) = \begin{cases} \frac{i}{2}\exp\left(-i2\pi f\xi_0\right) & f_0 - \frac{\Delta f}{2} \leq f \leq f_0 + \frac{\Delta f}{2} \\ 0 & otherwise \end{cases} \tag{6.5}$$

We multiply $\widetilde{I}\left(f_1\right)$ by the complex conjugate of $\widetilde{I}\left(f_2\right)$ and define this as the cross-spectrum $X(f_0, f_1)$

$$\begin{array}{rcl} X\left(f_1, f_2\right) & = & \left[\frac{i}{2}\exp\left(-i2\pi f_1\xi_0\right)\right] \cdot \left[\frac{i}{2}\exp\left(-i2\pi f_2\xi_0\right)\right]^* \\ & = & \frac{1}{4}\exp\left[-i2\pi\xi_0\left(f_1 - f_2\right)\right] \end{array} \tag{6.6}$$

We calculate the optical path from the argument of Eqn. 6.6

$$\xi_0 = \frac{1}{2\pi}\frac{\arg\left[X\left(f_1, f_2\right)\right]}{\left(f_1 - f_2\right)} \tag{6.7}$$

In practice we are dealing with the discrete intensities and finite series of data acquisition ; we can rewrite (6.2) as the discrete function $\overline{n}(j)$, which is the average detector count (noiseless case).

$$\overline{n}(j) = x_t\left\{1 \pm V\frac{\sin\left[\pi\left(j - J_0\right)\Delta m\right]}{\pi\left(j - J_0\right)\Delta m}\sin\left[\frac{2\pi\left(j - J_0\right)m_0}{N}\right]\right\} \tag{6.8}$$

where j is the sample number, m_0 the discrete spatial frequency (related to the frequency f_0), N is the number of samples, x_t the total discrete intensity related to I_t, V the apparent visibility, Δm the bandpass width and J_0 is the optical path that we want to calculate. The cross-spectrum X is now calculated for all the frequencies in the bandpass, in order to improve the signal-to-noise. The phases can in fact be averaged as vectors in the bandpass as shown by Buscher (1988).

$$X = \sum_{m_1}\left\{\left[\frac{i}{2}\exp\left(-i\frac{2\pi m_1 J_0}{N}\right)\right] \cdot \left[\frac{i}{2}\exp\left(i\frac{2\pi m_2 J_0}{N}\right)\right]^*\right\} \tag{6.9}$$

Here the sum is over all m_1 values within the bandpass, amd $m_2 = m_1 + \Delta m_{12}$, and Δm_{12} is a small integer. The phase noise is reduced by $\sqrt{N}$ if the noise is normally distributed, as it is the case for detector noise, which is dominant in near infrared.

$$J_0 = \frac{N}{2\pi} \frac{\arg\left(\overline{X}\right)}{\Delta m_{12}} \tag{6.10}$$

Then J_0 can be calculated from Eqn. 6.10, here the returned value is expressed in sample number, starting from the origin. The frequency difference Δm_{12} is usually kept to one sample, is $\Delta m_{12} = 1$.

6.3.2 The Algorithm

The algorithm derived from Eqn. 6.10 is computationally very simple. It boils down to four steps :

Take Fourier transform of the acquired scan.

Multiply the Fourier transform by its complex conjugate, retarded by one sample.

Add the resulting complex vectors within the bandpass.

Calculate the argument (phase) of the summed complex number and multiply the phase by the length N of the scan in samples, divided by 2π, in order to obtain the position J_0 expressed in samples.

6.3.3 Simulations

The linearity of the algorithm was tested in the absence of noise through simulations. It was found that the algorithm is capable of detecting the sign of the correction, necessary to bring back the fringes to the centre of the scan even if the main part of the fringe packet is outside the current scan. The necessary condition is to have enough signal-to noise so that the side lobes are detectable. This behavior is shown in the graph of Fig. 6.1. The returned position depends linearly on the fringe positions when the packet is inside the scan and becomes strongly non-linear (but with the correct sign) when the packet is outside the scan.

The non-linearity of the algorithm is influenced by the bandwidth and the length of the scan, as shown in Fig. 6.2. The main source of error is aliasing. In fact when the fringe envelope fits inside the scan, from zero to zero, in the cross-spectrum there are only two independent spatial frequencies which can be used for calculating the differential phase. When the envelope does not fit in the scan, the two spatial frequencies get aliased and finally merge. This could be one contribution to the excess noise found on experimental data and reported in this paper in Sec.6.4.7

6.3.4 Baseline Bootstrapping

With baseline bootstrapping we are capable of blind-tracking fringes on a baseline when the signal-to-noise of the fringes is too low, provided that good signal-to-noise is

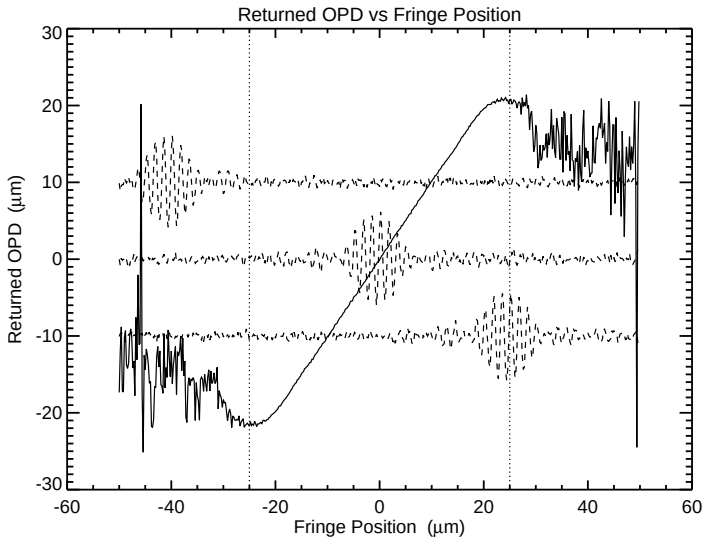

Fig. 6.1.— The optical path returned by the algorithm with respect to the fringe position (continuous-line plot). This simulation was performed in presence of photon and detector noise, with an average number of 300 photoelectron/sample for the fringe intensity (Poisson distributed), a fringe visibility of one and an additional 12-electron mean of Gaussian noise for the detector. The two vertical dotted-lines represent the interval inside of which the fringes are sampled. Three fringe packets (dashed-lines) mark three representative positions on the plot : outside the scan range (top), at the centre of the scan (centre) and half outside the scan range (bottom). Note that only the side lobes are visible in the scan range of the plot at the top. The returned position depends linearly on the fringe positions when the packet is inside the scan and becomes strongly non-linear when the packet is outside the scan. Nevertheless the information of the side lobes can still be used to bring the fringes back to the centre of the scan. The algorithm is sensitive to the slope of the phase across the bandwidth and the sign of the correction is preserved. The algorithm starts to fail at the limit of the range where the signal is too low and the side lobes not detectable for the given integration time.

available on the other two baselines. For this reason, we calculate the optical path J_0 for three baselines even if we correct the path for two baselines. We can express one optical path as the weighted average of the other two optical paths, the weights being equal to the SNR for the fringes obtained on those baselines. The signal-to-noise is calculated from the cross spectrum $|X(f_1, f_2)|^2$, dividing the averaged power inside the fringe peak by the averaged power outside the fringe peak. We then observe that the optical path, in a closed loop must be equal to zero :

$$J_0 1 + J_0 2 + J_0 3 = 0 \tag{6.11}$$

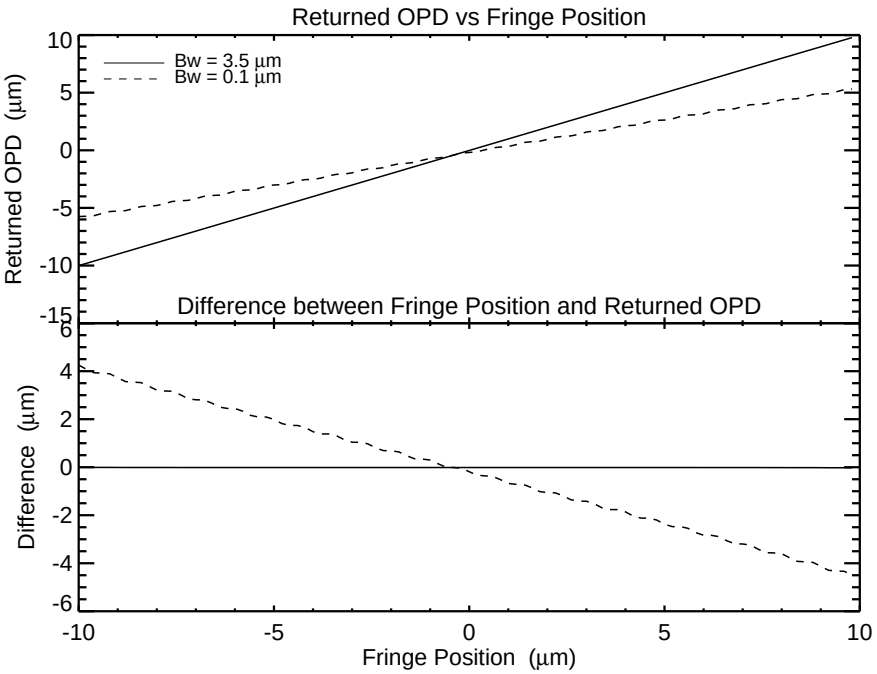

Fig. 6.2.— Linearity comparison for two different filter-widths. Top shows the optical path returned by the algorithm with respect to the fringe position for the two filters. Bottom shows the residuals obtained by subtracting the position of the fringes from the returned position. When the fringe packet is larger than the scan length the frequencies in the Fourier spectrum, from which we calculate the differential phase, start to be aliased. The returned position shows then an error, shown by the change in slope of the top graph.

where $J_0 1$ and $J_0 2$ are the optical path where the servo loop is acting, while $J_0 3$ is the reference optical path. To the path $J_0 1$, $J_0 2$ and $J_0 3$ are associated the weights $w1$, $w2$ and $w3$ respectively. We have two values for each optical path. One is the value obtained directly on that baseline (for example $J_0 1$ with weight $w1$), the other is the value calculated from the linear combination of the other two baselines (for example $J_0 1' = -J_0 2 - J_0 3$ with weight $w1' = (w2w3)/(w2 + w3)$). The weighted average of J_0 and J_0' can then be written as shown by Bevington & Robinson (1992) as :

$$\overline{J_0 1} = \frac{w1 J_0 1 + w1' J_0 1'}{w1 + w1'} \tag{6.12}$$

where $\overline{J_0 1}$ is the weighted-averaged path difference. Similarly for $\overline{J_0 2}$:

$$\begin{array}{rcl} \overline{J_0 2} & = & \frac{w2 J_0 2 + w2' J_0 2'}{w2 + w2'} \\ J_0 2' & = & -J_0 1 - J_0 3 \\ w2' & = & \frac{w1 w3}{w1 + w3} \end{array} \tag{6.13}$$

The advantage of using a weighting system is that we do not have to select the best baseline values a priori, but rather the weighting allows them to be selected automatically.

6.4 Variance of the Path Difference

6.4.1 Noise from the Infrared Detector

When taking the power spectrum of the acquired data we noticed the presence of noise increasing with frequency. The nature of this noise, as pointed out by Woillez (2003), must be found in the differencing process used to remove the discharge law of the pixel when processing raw data from the the PICNIC camera. The pixel of the PICNIC camera is a reverse-biased photodiode. The diode equivalent circuit includes a capacitor initially charged at the potential $V = V_0$. A charge $q_0 = V_0 C$ (where C is the capacity) is deposited on the two opposite sides of the junction in the diode. The photon-generated electrons deplete the capacitor, showing a change in the measured potential $V(t)$. In order to calculate noise we consider the simple case of a constant discharge of the capacitor caused by the average intensity incident on the diode

$$V(t) = V_0 - \frac{1}{C}\int_0^t \overline{q} t' dt' + \sigma_p(t) + \sigma_g(t). \tag{6.14}$$

Here $V(t)$ is a function of the photoelectrons generated at time t and the variable t' is the variable over which the function is integrated. The Gaussian noise σ_g is mostly added by the addressing and output electronics of the detector. The photon variance is $\sigma_p^2 = \frac{1}{C}\int_0^t \overline{q} dt'$. Two methods can be used for extracting the time-varying signal from the pixel : a) difference of adjacent samples (equivalent to a numerical derivative with respect to time), b) subtraction of a fit from the discharge law. When method a) is applied, Eqn. 6.14 can be differentiated analytically :

$$\begin{aligned} \frac{dV(t)}{dt} &= 0 - \frac{d}{dt}\left[\frac{1}{C}\int_0^t \overline{q}\,(t')\,dt'\right] + \frac{d}{dt}\left\{\left[\frac{1}{C}\int_0^t \overline{q}\,(t')\,dt'\right]^{\frac{1}{2}}\right\} + \frac{d}{dt}\left[\sigma_g(t)\right] \\ &= -\frac{1}{C}\overline{q}\,(t)\left[1 + \frac{1}{2\sigma_p(t)}\right] + \frac{d}{dt}\left[\sigma_g(t)\right] \end{aligned} \tag{6.15}$$

where

$$\sigma_p(t) = \left[\frac{1}{C}\overline{q}(t)t\right]^{\frac{1}{2}} \tag{6.16}$$

The initial voltage V_0 disappears and we obtain $-(1/C)\,\overline{q}(t)t$ plus an expression related to the photon noise σ_p plus the derivative of the Gaussian noise σ_g. This derivative is equivalent to a high pass filter since a derivative in the real plane is equivalent to a multiplication by $\omega = 2\pi f$ in the Fourier plane, as seen in Fig. 6.3. The shape of the power spectrum can be explained by the following discrete example with a running average of the detector voltage V_n written as :

$$V_n = V_0, V_1, V_2, ..., V_N \tag{6.17}$$

The running average is then :

$$\overline{V}_n = \frac{V_0 + V_1}{2}, \frac{V_1 + V_2}{2}, \cdots, \frac{V_{N-1} + V_N}{2} \tag{6.18}$$

Smoothing the original function with a two point running mean is equivalent to convolving it with a step function of width $\Delta t = 2$ (two samples). The Fourier transform of this function is

$$\widetilde{\overline{V_n}} = 1 - \frac{\sin(\pi f / f_{max})}{\pi f / f_{max}}, \tag{6.19}$$

a $1-$ sinc function where the sinc function has has a maximum value at zero frequency and zero value at maximum frequency. If we subtract $\overline{V}_n$ from the original function V_n we obtain :

$$\begin{aligned} V'_n &= V_0 - \tfrac{V_0}{2} - \tfrac{V_1}{2}, V_1 - \tfrac{V_1}{2} - \tfrac{V_2}{2}, \cdots, V_{N-1} - \tfrac{V_{N-1}}{2} + \tfrac{V_N}{2} \\ &= \tfrac{1}{2}(V_0 - V_1), \tfrac{1}{2}(V_1 - V_2), \cdots, \tfrac{1}{2}(V_{N-1} - V_N) \end{aligned} \tag{6.20}$$

which is the discrete equivalent of the differential equation (6.15) times a constant (1/2). Let the Fourier transform of V'_n be $\widetilde{V'_n}$. Then, since the Fourier transform is additive, the noiseless power spectrum of the difference data V'_n will be $|V'_n$ - sinc$|^2$. Thus, CDS samples will have a PSD which is the absolute value squared of the Fourier transform of the signal minus a sinc function, plus of course noise. This is illustrated in Fig. 6.15

We also investigated a different way (method (b)) of removing the discharge law of the pixel. In this second method we fit the discharge law with a line plus a constant and subtract it from Eqn. 6.14. If we consider the removal of the discharge voltage to be perfect then the only source of noise left is the Gaussian noise $\sigma_g(t)$ and the photon noise $\sigma_p(t)$. The total noise $\sigma_t(t)$ will be then

$$\begin{aligned} \sigma_t(t) &= \sigma_p(t) + \sigma_g(t) \\ &= \left[\tfrac{1}{C}\int_0^t \overline{q} dt'\right]^{\frac{1}{2}} + \sigma_g(t) \end{aligned} \tag{6.21}$$

and the total noise σ_t will be

$$\sigma_t(t) = \left(\frac{1}{C}\overline{q}t\right)^{\frac{1}{2}} + \sigma_g(t) \tag{6.22}$$

Now we have obtained a formula where the noise is time-dependent, the amplitude increasing with the square root of time. In Fourier space the integral of this noise becomes a division by $\omega = 2\pi f$. This is a low pass filter, the noise decreasing with frequency. Fig. 6.3 shows the results obtained in this section through simulations. To summarise, we discovered that the differencing process adds noise proportional to the frequency in the shape of a $(1-\text{sinc}^2$ function. The linear fit method returns a $1/f$ type of noise which is larger and more problematic to remove for data analysis.

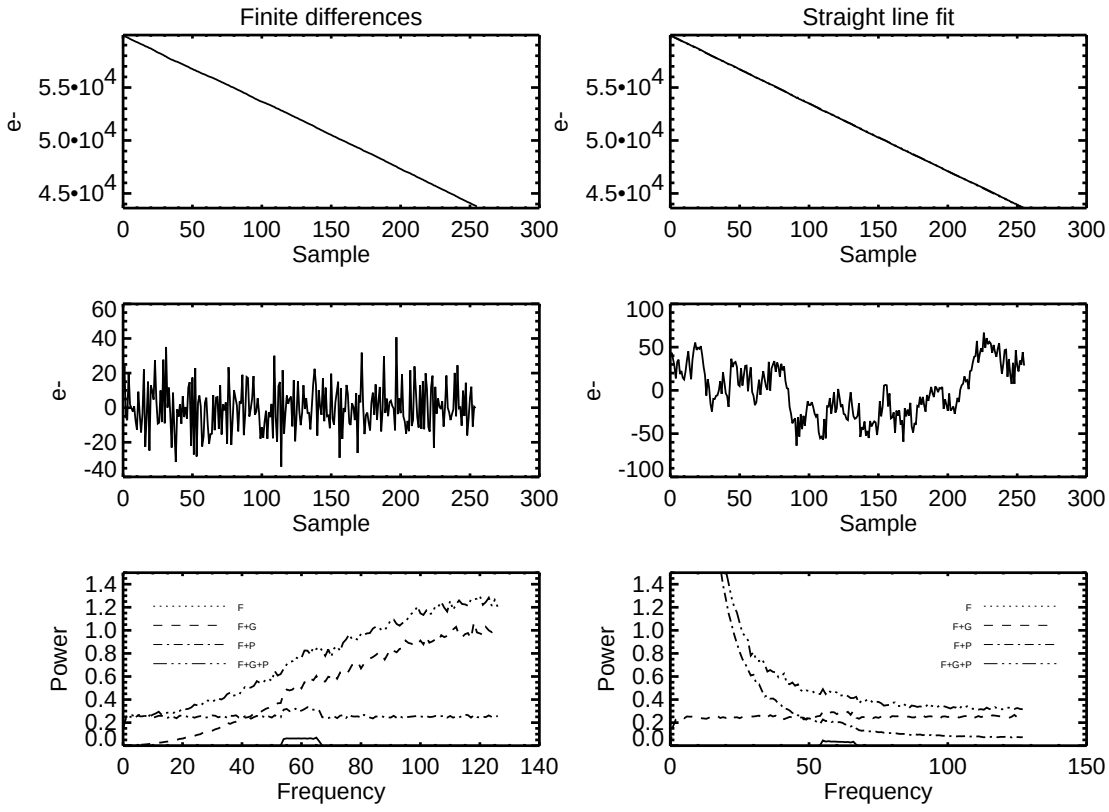

Fig. 6.3.— Simulated camera data (top). Top-left shows the discharge law of the pixel, top-right the discharge law compared to its linear fit (the two plots are undistinguishable). Centre-left shows the differentiation of the top waveform, showing the high frequency noise caused by the differencing. Centre-right shows the difference between data and linear fit. It can be observed that low frequency noise is mostly present. Bottom-left shows the power spectra of the data simulated with photon noise (P), Gaussian noise (G) and in absence of noise (F only), for the differencing method. The bottom-right panel shows the same plots as the left panel but for data processed using a linear fit to the data. Bottom-left shows that the greatest noise contribution to the power spectrum is the derivative of the Gaussian noise from the detector $|1-\mathrm{sinc}|^2$ function) which is an f type noise (noise increasing with frequency). The bottom-right panel shows that the largest contribution to noise is due to the integration of Poisson noise, which is a $1/f$ type of noise, which decreases with frequency.

6.4.2 Photon and Detector Noise for a Single Wavelength Fringe

Walkup & Goodman (1973) showed that the error in the discrete Fourier transform, used for estimating the phase of a periodic waveform, is proportional to the inverse of the signal-to-noise ratio (SNR). In our case the signal is the temporally-

modulated fringe obtained by changing the optical path among telescope pairs by means of a piezo-electrically-operated delay lines, driven by a sawtooth signal. The noise is the statistical fluctuation caused by the arrival of discrete photons on the detector. These quantities can be directly derived from the acquired data and are the base of our phase noise estimator. In their derivation Walkup and Goodman used the simplifying hypothesis of using a single-wavelength sinusoidal function, comprising of an integer number of periods, filling the sample space. From Walkup & Goodman (1973) the variance of the phase $\sigma^2(m_0)$ for this wave is :

$$\sigma^2(m_0) = \frac{2\left(1+\frac{x_b}{x_s}\right)}{V_s^2 N_s}, (rad^2) \tag{6.23}$$

where x_s is the detector count per sample produced by the intensity I_s, x_b the background count per sample of the intensity I_b, V_s is the visibility and $N_s = N\,x_s$, with N equal to the number of samples. Thus N_s is the total number of counts from all samples. Eqn. 6.23 can be conveniently rewritten in term of the total intensity x_t, which contains the background term x_b ($x_t = x_s + x_b$) and the apparent visibility $V = V_s I_s/(I_s + I_b)$. Eqn. 6.23 becomes the simplified expression :

$$\sigma^2(m_0) = \frac{2}{V^2 N_t}, \tag{6.24}$$

where $N_t = N \cdot x_t$. The apparent visibility V contains the background and it is equal to the visibility V_s when the background x_b is zero. Eqn. 6.23 gives an expression for the variance of the noise (in rad^2) which depends solely on photon and background noise. The term $\frac{1}{N_t}$ is the inverse of the SNR^2. We modify Eqn. 6.24 and include the detector noise term x_d. (See Appendix B for derivation).

$$\sigma^2(m_0) = \frac{2\left(1+\frac{x_d^2}{x_t}\right)}{V^2 N_t}. \tag{6.25}$$

6.4.3 Effect of Finite Bandwidth

In reality the interferometric signal has a finite bandwidth and the fringe is not a continuous wave-train but has an envelope term which depends on the shape of the filter. This bandwidth effect can be taken into account by revising the SNR expression and considering that the noise will be the same but the signal will be lower, since the fringes appear only in one part of the scan, due to the envelope function. If the scan total length is N and the envelope length is N_0 the SNR for a single-wavelength case will be corrected by the ratio of the number of points N/N_0 and the variance in rad^2 will be

$$\sigma^2(m_0) = \frac{2}{V^2\,(SNR_N)\,\frac{N_0}{N}} \tag{6.26}$$

This can be expressed more conveniently as a function of the bandwidth of the filter. The filter is a top–hat function and its Fourier transform a sinc function. We know

then that $N_0/N = (\lambda^2/\Delta\lambda)/\Delta j$ where λ is the centre-band wavelength, $\Delta\lambda$ the bandpass width, and Δj the optical path modulation or "scan length". We substitute this expression in Eqn. 6.26 and obtain a variance in rad^2 which depends on the filter-width.

$$\sigma^2(m_0) = \frac{2}{V^2\,(SNR_N)\,\frac{\lambda^2 d}{\Delta\lambda}} \tag{6.27}$$

Expressing the variance in μm^2 will simplify Eqn. 6.27. The variance in μm^2 is then :

$$\sigma^2(m_0) = \frac{2}{V^2\,(SNR_N)}\frac{\Delta\lambda\,\Delta j}{4\pi^2}, \tag{6.28}$$

where wavelength and bandwidth are expressed in μm.

6.4.4 Variance of the Atmosphere

An effect which we did not take into account yet is the fact that, while we are acquiring our interferogram, the optical path is continuously changing through the turbulent atmosphere. This effect can be more important than the noise introduced by detector and photon noise. The variance of the phase, in rad^2, for the turbulent atmosphere in the interval time τ can be written as (Roddier 1999)

$$\sigma_a^2 = \sigma_0^2 + \left(\frac{\tau}{\tau_0}\right)^{\frac{5}{3}}, \tag{6.29}$$

where σ_0 is the noise from the detector, from photon statistics and from photometric fluctuation, τ_0 is the the coherence time and σ_a is in radians. In the case of long baseline interferometry, the covariance $\sigma\,(x_1, x_2)$ of the phase perturbations for separate apertures is zero. The variance of their phase is then uncorrelated. The total variance of the piston acting on the interference fringes (in μm^2 if λ is in μm) is then twice the variance of a single aperture and can be written as :

$$\sigma_m^2 = 2\frac{\lambda^2}{4\pi^2}\left[\sigma_0^2 + \left(\frac{\tau}{\tau_0}\right)^{\frac{5}{3}}\right]. \tag{6.30}$$

6.4.5 Latency of the Measurement

The fringe packet is acquired, in servo mode, by scanning the optical path up to 100μm and the path correction is applied at the end of the scan. We call $\Delta t_p = \tau + \tau_{fb}$ the time between two corrections (τ_{fb} is the fly-back time when the piezo scanner is resetting to the initial position and is typically 1/3 of τ). By that time the atmosphere has changed and the total variance of the phase can be calculated using (6.30). The total atmospheric phase variance is then :

$$\sigma_m^2 = 2\frac{\lambda^2}{4\pi^2}\left[\sigma_0^2 + \left(\frac{\tau}{\tau_0}\right)^{\frac{5}{3}} + \left(\frac{\Delta t_p}{\tau_0}\right)^{\frac{5}{3}}\right]. \tag{6.31}$$

6.4.6 Total Phase Variance

The total phase variance (μm^2) of the fringe packet measurement is simply the sum in quadrature of all the contributions, notably the detector noise, photon noise photometric fluctuations and atmosphere turbulence. Since we calculate a differential phase across the bandwidth (see Sec. 6.4.2 - 6.4.3), the variance will be twice as bad as the error on the phase. Eqn. 6.32 is then multiplied by two, giving

$$\sigma^2_{tot} = \frac{2}{V^2(SNR_N)}\frac{\Delta\lambda\,\Delta j}{\pi^2} + \frac{\lambda^2}{\pi^2}\left[\left(\frac{\tau}{\tau_0}\right)^{\frac{5}{3}} + \left(\frac{\Delta t_p}{\tau_0}\right)^{\frac{5}{3}}\right]. \tag{6.32}$$

6.4.7 Determination of the Coherence Time τ_0

In order to calculate the error in the estimated fringe position it is necessary to know the coherence time τ_0. This could be estimated by recording the correction commands sent to the piezo scanners and short delay lines. This methods implies a good understanding of the servo system, which we currently do not have. An alternative and easier way of determining τ_0 is to record the correction commands that would be sent, in an open-loop configuration. For this purpose we acquire fringes and allow them to drift, recording their positions.

The variance of the difference of recorded positions of fringes is calculated for all the data points. The calculation is repeated on the same data-set but, this time, the difference is performed every other data point, then every two and so on. In practise, we increase the delay in sampling data points and we build a plot of the variance with respect to the time delay.

We can now use some results from adaptive optics (Roddier 1999) to estimate τ_0 from the phase variance measured at each aperture (the phase variance is doubled when we measure the phase variance associated with two interfering light beams coming from separate apertures, since the variance of the two apertures is assumed to be non-correlated). A pure time delay τ in the control loop produces a mean square wave-front error, derived from the phase structure function $D_\varphi(\tau)$, given by

$$\sigma^2(\tau) = 6.88\,(\bar{v}\tau/r_0)^{\frac{5}{3}}. \tag{6.33}$$

Comparison with Eqn. 6.29

$$\tau_0 = (6.88)^{-\frac{3}{5}}\left(\frac{r_0}{\bar{v}}\right). \tag{6.34}$$

When we combine Eqn. 6.33 with 6.34 we obtain

$$\tau_0 = \tau\left[\sigma^2(\tau)\right]^{-\frac{3}{5}}. \tag{6.35}$$

We can measure τ_0 by fitting a line to the open-loop data, as shown in Fig. 6.4, and determining the intercept $\sigma^2(\tau_0)$ and the slope $\sigma^2(\tau)$. In this way Eqn. 6.35 becomes

$$\tau_0 = \tau\left\{\frac{1}{4}\left[\sigma^2(\tau) - \sigma^2(\tau_0)\right]\right\}^{-\frac{3}{5}}.$$

The 1/4 term derives from adding the variance of two apertures and adding the variance of data points when performing the difference of fringe positions. Fig. 6.4 shows the line fit to the data from which a coherence time $\tau_0 = 133$ ms was calculated. Table 6.1 summarises results obtained at IOTA the night of the 12th of March 2003.

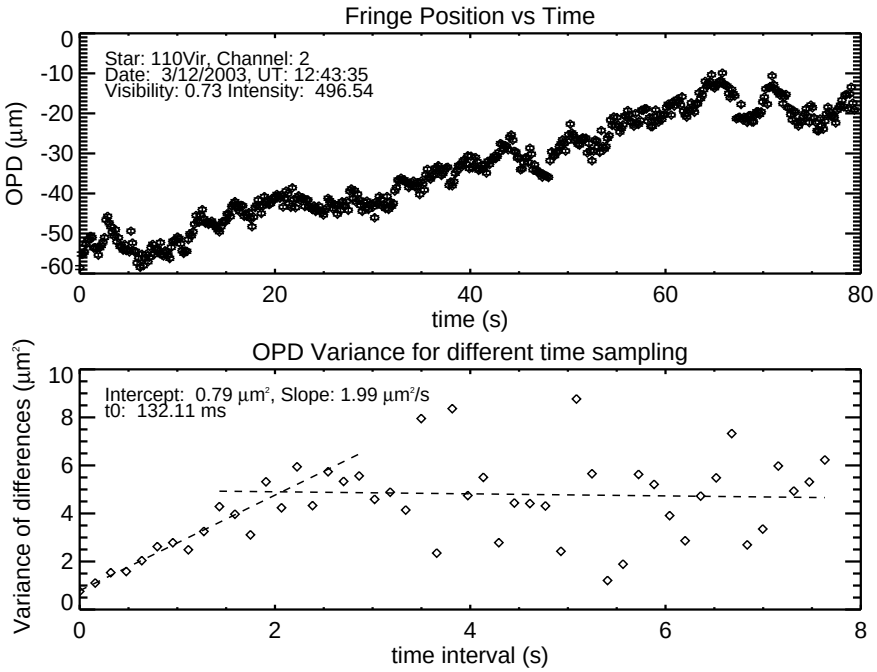

Fig. 6.4.— Variance versus time-delay plot. The top panel shows the the correction commands that would be sent, in an open-loop configuration in function of time, when fringes are left drifting. The variance of the difference of recorded positions of fringes is calculated for all the data points and re-sampled at different time intervals (bottom panel). The intercept of the line fit to the experimental data delivers the phase variance at time zero which is caused by the intensity fluctuations. The slope of the line yields the variance of the atmosphere from which the coherence time τ_0 can be derived.

The experimental data presented in this paper was recorded with a 0.1 μm band-pass filter which caused the fringe envelope to be larger than the scan length. As reported in Sec.6.3.3 In this table the phase noise is derived from the intensity fluctuations and compared with the values obtained from the intercept of the linear fit used to calculate the parameter τ_0. The calculated phase variance is somewhat smaller than the value obtained experimentally, indicating that some other noise source has been neglected. Fig. 6.5 shows the reduction of tracking residuals operated by the algorithm. An improvement of a factor 2 RMS can be shown from the recorded data. This lies mostly in the lower frequency zone because of the limited bandwidth of the combined fringe-sensor, fringe-actuator. For the IOTA interferometer this is a

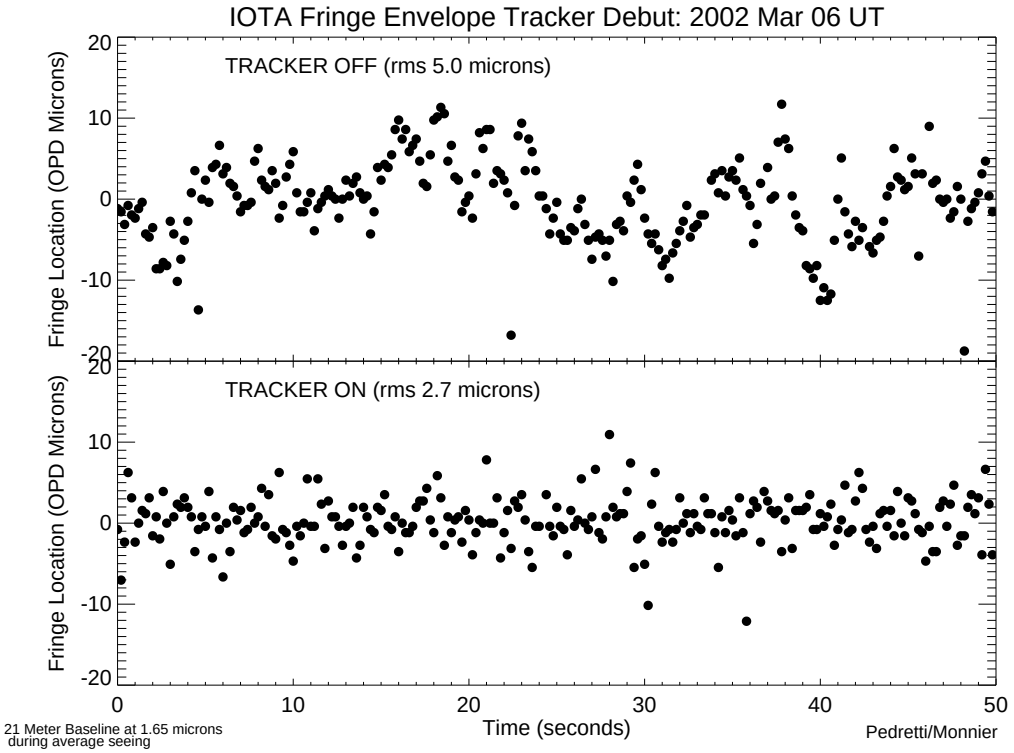

Fig. 6.5.— The change of the OPD with the fringe tracker turned off (top) and on (bottom). We measure a factor 2 reduction in the RMS change in optical path.

significant improvement, since the high frequency phase noise is dealt within post-processing using the closure-phase information. It is then more important to be able to maintain the fringe packet superposed and being able to do so for faint sources rather than reduce the residuals of the OPD to a smaller value.

6.5 Conclusions

We have described the fringe packet tracking system now routinely in use at the IOTA interferometer. The packet tracker uses existing hardware to perform its functions, notably the science camera as a fringe sensor and the fringe scanning platforms combined with the delay lines, for correcting the optical path. It is based on a novel algorithm which exploits the wavelength-dependent information contained in the fringe packet, which is extracted using double fourier interferometry. The phase of the fringes obtained for different frequencies is used for calculating the group delay of the fringe packet. Since we use baseline bootstrapping we are capable of blind-tracking fringes on a baseline when their signal-to-noise is very low, provided that the fringes have a good signal-to-noise on the other two baselines of the interferometer. We use numerical simulation to model the case of a fringe packet outside the scanning range,

Visib.	Intens. (e)	Noise (e)	Phase Noise (μm)	Atm. Noise (μm)	Interc. (μm)	τ_0 (ms)
0.63	575.64	98.75	0.18	0.60	1.15	290.76
0.54	575.29	114.42	0.24	0.66	1.12	259.93
0.68	570.57	87.18	0.15	0.65	1.03	268.02
0.53	569.62	114.76	0.25	0.77	1.12	218.92
0.63	583.14	100.32	0.18	0.21	1.52	1026.78
0.63	562.00	99.26	0.18	0.46	1.30	403.68
0.63	583.56	98.62	0.17	0.37	1.30	522.30
0.63	582.84	98.48	0.17	0.49	1.02	376.74

Visib.	Intens. (e)	Noise (e)	Phase Noise (μm)	Atm. Noise (μm)	Interc. (μm)	τ_0 (ms)
0.84	671.06	101.25	0.26	0.12	0.89	167.49
0.82	663.72	103.03	0.27	0.12	0.93	177.55
0.86	660.16	106.49	0.27	0.12	1.29	425.30
0.81	661.16	115.69	0.31	0.14	1.44	363.57
0.87	673.56	89.68	0.22	0.10	1.45	204.87
0.87	663.18	95.98	0.24	0.11	1.12	199.64
0.85	670.02	100.10	0.25	0.11	1.22	217.11
0.86	679.02	105.86	0.26	0.12	1.43	387.88

Visib.	Intens. (e)	Noise (e)	Phase Noise (μm)	Atm. Noise (μm)	Interc. (μm)	τ_0 (ms)
0.71	496.54	120.91	0.49	0.32	0.89	132.45
0.62	496.59	116.75	0.57	0.37	1.01	184.58
0.74	496.38	124.61	0.48	0.31	1.13	162.63
0.53	498.61	109.35	0.60	0.38	0.89	209.67
0.75	502.13	124.93	0.47	0.30	0.93	248.36
0.73	499.55	123.81	0.48	0.31	0.96	182.52
0.72	496.65	122.86	0.49	0.31	0.86	201.32
0.72	506.83	123.07	0.48	0.31	0.84	165.94

Table 6.1: Experimental results are summarised in this table for the three baselines and for different observations performed during the same night. The top panel gives results for baseline AB, the centre panel for baseline BC and the bottom panel for CA. Each row in each panel lists averaged quantities from a set of 256 individual fringe-packet scans. Column one lists the average fringe-packet visibilities. Column two lists the average intensity (in electrons) of the fringes. Column three is the average RMS noise in a scan (in electrons) calculated by removing the signal (fringes) from the scan. Column four lists the RMS noise (in microns) calculated from Eqn. 6.28. Column five shows the RMS noise added by the atmosphere, in microns (Eqn. 6.30). Column six gives the RMS noise (in microns) obtained by a linear fit to optical path variance in function of time sampling (one example listed in Fig. 6.4). The intercept is the atmospheric noise extrapolated to time zero where only the other noise contributions are present (eg. photon and detector noise). Column seven shows the parameter τ_0 calculated from the slope of the linear fit of Fig. 6.4.

operated by the algorithm, when only the side lobes of the fringe packet are visible. We also remark that the fringe packet tracker is still capable of correcting the optical path succesfully when a narrow-band filter is employed during data acquisition and the packet is larger than the scanning range. In this case an additional error of about half-fringe is introduced in the optical path. This error is caused by the aliasing of the frequencies in the band-pass used to calculate the OPD. We confirm that correlated double sampling causes the noise to increase with frequency, as seen in the power spectrum of the infrared camera data, and that this is caused by the differencing of the collected data. This operation of taking differences of the data is necessary for removing the discharge law of the pixels of the camera. We derive an expression for this noise allowing the fitting and removal of it. We derive an expression which relates the error on the optical path to the photoelectrons detected by the infrared camera

and to the coherence time of the atmosphere. We compare this noise with the one obtained from experimental results. We show that the fringe packet tracker algorithm effectively reduces the slowly varying atmospheric and instrumental-induced additional path, leaving the fast phase noise to be dealt with post-processing closure-phase measurement. We also show that the coherence time τ_0 can be derived from the experimental data. This parameter is obtained by running the fringe packet tracker in open-loop mode and scanning the fringes in a time shorter than the coherence time itself. This parameter is very useful for calculating the residual error introduced by the fringe packet tracker and for optimally sampling the fringe packet according to the seeing conditions.

6.6 Acknowledgements

The IONIC project is a collaboration among the Laboratoire d'Astrophysique de Grenoble (LAOG), Laboratoire d'Electromagnetisme Microondes et Optoelectronique (LEMO), and also CEA-LETI and IMEP, Grenoble, France. The IONIC project is funded in France by the Centre National de Recherche Scientifique and Centre National d'Etudes Spatiales. The work and the fringe packet tracker were supported in part by grant NAG5-4900 from NASA, by grants AST-0138303 from the NSF, and by funds from the Smithsonian Institution.This research has made use of NASA's Astrophysics Data System Bibliographic Services.

Chapitre 7

Le Diamètre Multi-couleur des Étoiles Miras dans l'Infrarouge Proche

Pedretti, E., Millan-Gabet, R., Schloerb, F. P., Traub, W. A., Monnier, J. D., Ragland, S., Lacasse, M. G., & Carleton, N. P. 2001, paru dans *American Astronomical Society Meeting*, **199**, 9216

Résumé

Au cours d'une campagne d'observation entre 1997-1999, l'interféromètre infrarouge IOTA (Infrared Optical Telescope Array) obtint des mesures interférométriques dans le proche infrarouge pour un grand échantillon d'étoiles variables Mira de longues périodes. Ce domaine spectral est important pour obtenir des contraintes sur la physique de l'atmosphère de ces étoiles. Nos résultats préliminaires, sous la forme de mesures de diamètres stellaires dans chacune des bandes spectrales J, H, et K, sont présentés pour un sous-échantillon de Miras qui ont été mesurées dans ces trois bandes spectrales. L'ensemble des données sur les Miras, contenant d'autres étoiles mesurées dans deux bandes spectrales seulement, est en cours d'analyse et sera ajouté à une publication en cours de préparation, basée sur ce travail. Nous avons déterminé les rapports des diamètres moyens entre ces trois bandes spectrales, et mesuré une corrélation avec la phase des pulsations de ces étoiles.

Introduction

Au cours de l'année 2000, j'ai participé au travail de réduction de données, obtenues pour un grand échantillon d'étoiles variables Mira, collectées par Rafael Millan-Gabet avec l'interféromètre IOTA.

En collaboration avec Rafael Milla-Gabet, j'ai réduit les visibilités brutes et je les ai calibrées en utilisant les logiciels de réduction de données d'IOTA.

En plus de ma contribution au travail de réduction de données, j'ai écrit un logiciel qui permet de calculer le diamètre angulaire des étoiles à partir des visibilités calibrées. Ce logiciel réalise l'ajustement d'un modèle de disque uniforme sur les mesures de visibilités calibrées et produit les courbes de visibilités des modèles correspondant le mieux aux données.

J'ai présenté les résultats obtenus au cours de cette collaboration à la conférence de la société astronomique américaine (AAS) à Washington en 2001.

Multi–color Diameters of Mira Stars in the Near Infrared

Pedretti, E., Millan-Gabet, R., Schloerb, F. P., Traub, W. A., Monnier, J. D., Ragland, S., Lacasse, M. G., & Carleton, N. P. 2001, *American Astronomical Society Meeting*, **199**, 9216

Abstract

In an observing campaign between 1997-1999, the Infrared Optical Telescope Array (IOTA) obtained interferometric measurements in the near-infrared of a large sample of long period variable (Mira) stars. This spectral coverage is important in order to constrain the atmospheric physics in these stars. Our preliminary results, in the form of stellar diameter estimates at each band are presented, for the subset of Mira stars which were measured at all three J, H and K′ bands. The full set of Mira data, containing additional stars observed only at two bands, is currently being analysed and will be added to a publication based on this work currently in preparation. We have established the mean diameter ratios at these three bands, and measured a correlation with pulsational phase of the stars.

7.1 Introduction

Mira stars are highly evolved cool giants. They are very large - several hundred times the radius of the Sun, and very luminous - several thousand times the luminosity of the Sun. Miras pulsate with a period of about one year. As they expand, Miras become visually fainter, their spectrum shifts to later types, and the properties of molecule and dust formation in their extended cool atmospheres change.

Despite much observational and theoretical work, many fundamental aspects of Mira atmosphere physics remain unknown. The determination of their sizes and shapes, and the variation of these quantities over time and wavelength are of fundamental importance, and can be directly measured with long baseline interferometers.

7.2 Observations

The observations presented here were carried out at the IOTA interferometer over the period 1997-1999. In this experiment, IOTA was operated in its two-telescope configuration, using two different baselines of approximate lengths 21 m and 38 m. Our full sample to date consists of 28 Mira stars, of which we present here results for a subsample of 13 stars measured at all three J, H and K′ bands. The list of the observed sources and calibrators is given in Table 7.1. The uniform disk fit to the visibility data, from the observations, is shown in Fig. 7.1 and the diameters measured with the uniform disk fit are listed in Table 7.2.

Fig. 7.2 shows a representative spectra for Mira stars (Lançon & Wood 2000) where the broad filters encompass strong molecular bands of species such as H_2O, CO, TiO, VO and OH. This figure also illustrates how the amount of molecular absorption changes strongly as a function of pulsational phase. We aim to detect any diameter changes associated with this absorption.

Target	Sp. Type	Calibrator	Cal. Diam.
R And	Se ...	HR175	1.14 ± 0.04
Z Cet	M6e	HR353	1.48 ± 0.05
U Per	M6e	HR787	1.18 ± 0.01
R Per	M4e	HR876	1.09 ± 0.01
R Aur	M7III	HR1866	2.52 ± 0.42
X Aur	K2	HR2338	1.69 ± 0.21
R Lmi	M7e	HR4081	1.19 ± 0.08
R Hya	M7IIIe	HR4958	1.58 ± 0.07
R Ser	M7IIIe	HR5940	1.55 ± 0.09
S Crb	M7e	HR5674	2.92 ± 0.87
RS Lib	Me	HR5824	2.29 ± 0.15
S Peg	M6e	HR8916	2.30 ± 0.03
R Aqr	M7III	HR8980	3.10 ± 0.45

Table 7.1: Observed targets and calibrators list for the Mira sample.

7.3 Results

We have performed the first simultaneous measurements of J, H, and K′ band Mira star diameters using a long-baseline interferometer. We have obtained the first measurements of their mean diameter ratios at those bands, critical information for modelers of stellar atmospheres. For Mira stars of M6/M7 spectral type we find that the J diameter is less then the H diameter and that the H diameter is less than the K diameter. On average we find the J-band to H-band diameter ratio to be about 0.95 and the H-band to K-band diameter ratio to be about 0.86.

Fig. 7.1.— Uniform disk visibility plots at J, H and K' band for a sample of 16 stars.

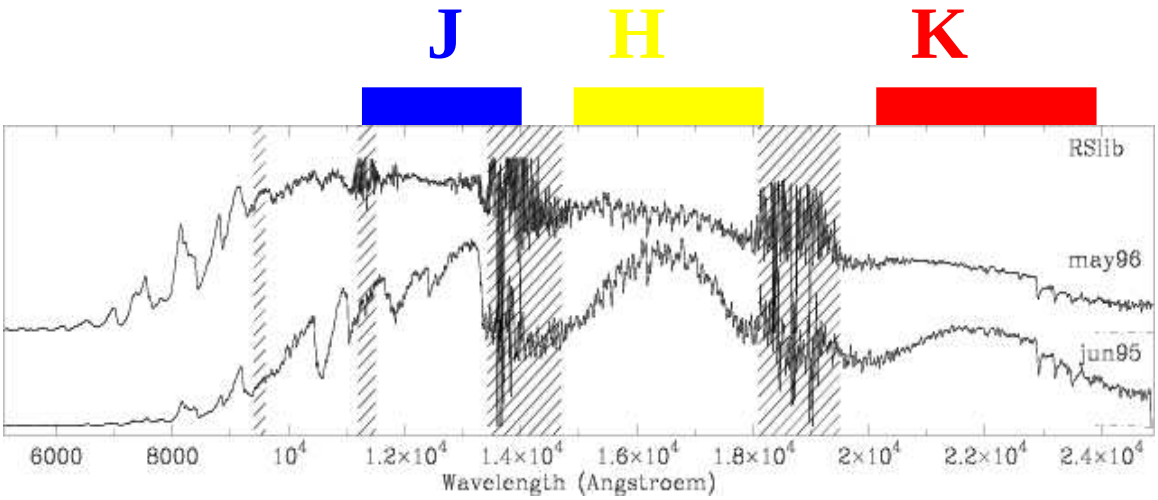

Fig. 7.2.— Spectrum of the star RS Lib. Top shows the spectrum at maximum light, and bottom the spectrum at minimum light. From Lançon & Wood (2000).

It has not been previously well-established that the near-IR band diameters change coherently with the pulsational period. We see evidence for this in our data, using diameter ratios which are relatively insensitive to sources of systematic error like

Target	Epoch	U.D. J	σ	U.D. H	σ	U.D. K	σ
R And	2450774.0	6.68	0.0	6.65	0.2	5.76	0.3
Z Cet	2451122.0	2.61	0.1	3.48	0.1	3.12	0.4
U Per	2450772.0	4.99	0.1	5.38	0.1	6.51	0.2
U Per	2451088.0	2.13	0.6	3.88	0.3	5.44	0.4
R Per	2451089.0	< 0.00	—	< 0.00	—	< 0.00	—
R Per	2451123.0	< 0.00	—	1.14	0.5	< 1.00	—
R Aur	2450734.0	11.06	0.1	10.49	0.2	16.18	0.2
X Aur	2450736.0	< 1.00	—	< 0.00	—	< 3.00	—
R Lmi	2450873.0	12.49	0.0	12.85	0.2	14.12	0.2
R Hya	2450873.0	18.84	0.1	20.13	0.3	25.41	0.2
R Hya	2450875.0	20.32	0.1	22.04	0.3	27.40	0.2
R Ser	2450875.0	7.50	0.1	8.40	0.7	10.39	0.4
S Crb	2450874.0	9.24	0.2	8.95	0.4	9.30	0.4
RS Lib	2450873.0	9.85	0.4	9.07	0.8	9.22	1.1
S Peg	2451087.0	4.09	0.1	5.07	0.3	4.87	0.5
R Aqr	2450739.0	17.69	0.2	17.78	0.1	20.80	0.2

Table 7.2: Uniform disk (UD) diameter results for each star, at each band and epoch.

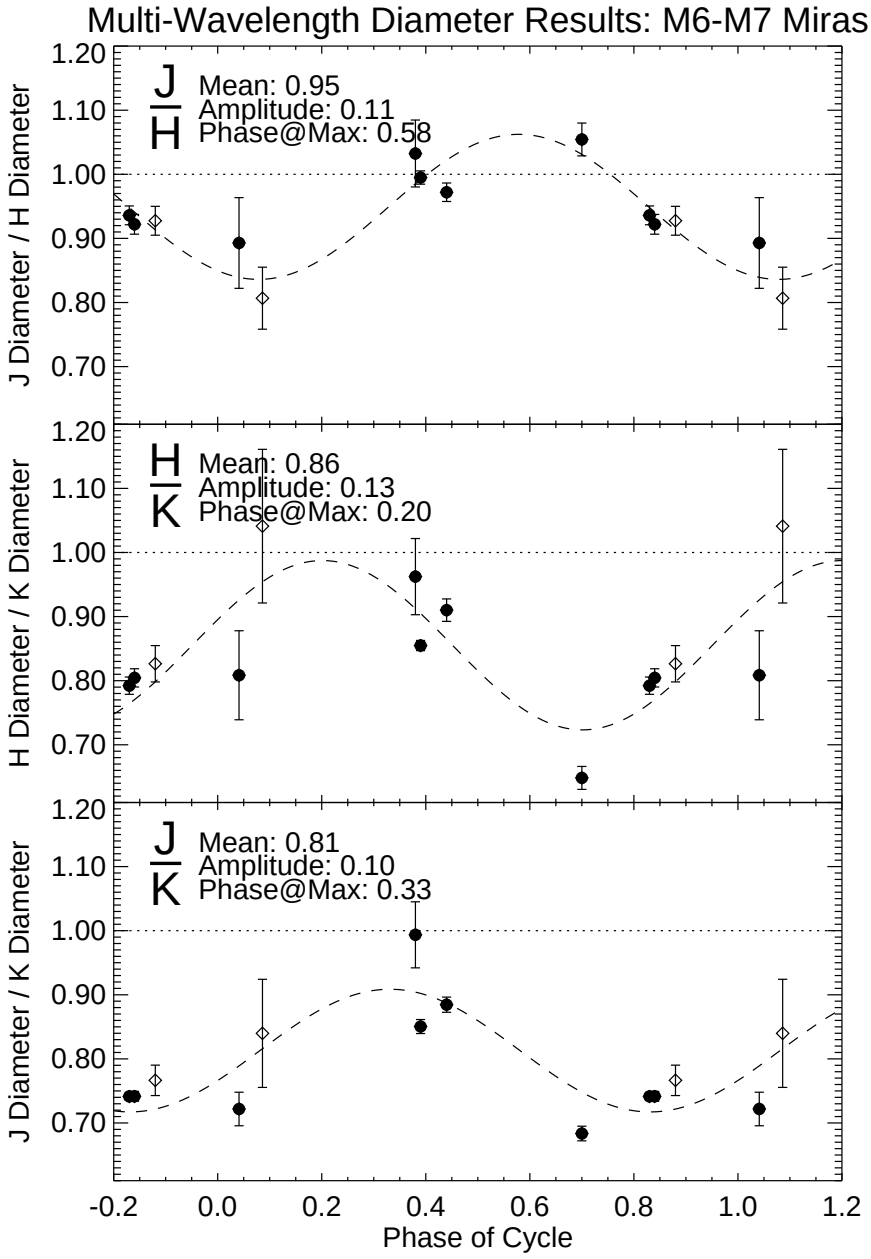

Fig. 7.3.— Diameter ratios for three different wavelengths versus phase of the light curve. The data points of different shape represent different spectral types. The plots show a correlation with pulsational phase of the stars

the wrong size of the calibrator stars, drifting optical alignement in the interferometer and atmospheric dispersion (Fig. 7.3). Statistically, the diameter ratios are seen to vary with amplitudes of 12%, 15% and 12% for J/H, H/K′ and J/K′ diameter ratios respectively. This variation suggests that the dominant molecular absorption features are located at different heights in the atmosphere and respond to the pulsation at

different times.

Infrared interferometry is providing a diverse set of multi-wavelength diameter measurements in the visible (Lattanzi et al. 1997; Young et al. 1999), near-infrared (Thompson et al. 2003), and mid-infrared (Weiner et al. 2003). Current atmospheric models do not quantitatively agree with well-established measurements (Mennesson et al. 2002), and it is important to establish stronger collaborations between experimentalists and modelers in order to interpret these data and optimize the observing strategies. It is to be expected that through these collaborative efforts important advances in the stellar models will be made.

Acknowledgments

We acknowledge Andy Boden and the Interferometer Science Center (ISC) for providing the calibrator diameters using their GetCal software.

Chapitre 8

Conclusions

J'ai exploré des techniques pour obtenir des images à haute résolution angulaire avec un interféromètre stellaire. Deux méthodes sont envisagées pour la prochaine génération d'interféromètres : l'imagerie directe, où l'interféromètre est utilisé comme équivalent d'un télescope géant où les faisceaux sont recombinés et cophasés dans le plan focal commun, et l'imagerie indirecte où l'interféromètre est utilisé comme un corrélateur, une méthode largement utilisée en interférométrie radio.

L'imagerie directe nécessite le cophasage de toutes les ouvertures utilisées dans l'interféromètre, similairement aux systèmes d'optiques adaptatives installés sur les télescopes monolithiques. Les techniques traditionnelles utilisées pour cophaser de grands miroirs ne sont pas utilisables pour des télescopes indépendants à cause de la discontinuité et de la décorrélation dans le front d'onde reconstruit. Avec mon directeur de thèse à l'Observatoire de Haute Provence j'ai conçu une méthode hiérarchique qui utilise des triplets d'ouvertures, capable de cophaser de grands interféromètres.

La simulation de cet algorithme de cophasage, qui utilise une hiérarchie de triplets, montre une convergence à la fois pour des objets résolus ou non-résolus. Lorsque trois différentes longueurs d'onde sont utilisées, l'égalisation des chemins optiques peut être obtenue avec des erreurs initiales de l'ordre de 10 μm. Des simulations utilisant des nombres de photons limités ont montré que des images résolues d'étoiles brillantes sont réalisables avec des ouvertures de 10 cm, aux longueurs d'onde visibles, en utilisant un phasage adaptatif.

J'ai réalisé, avec l'aide de mes collaborateurs de l'Observatoire de Haute Provence, les premières images directes obtenues sur le ciel avec un interféromètre à plusieurs ouvertures. L'instrument était une version miniaturisée d'interféromètre où la plus grande longueur de base était inférieure à 10 cm, afin d'éviter la dégradation de phase due à la turbulence atmosphérique. Ce travail a montré que des réseaux d'ouvertures où la pupille d'entrée et de sortie ne sont pas homothétiques, contrairement à ce qui est généralement pensé, peut former des images directes. J'ai observé un gain en intensité de $24 \pm 3\times$ par rapport à un réseau équivalent de type Fizeau. Ce résultat vient en support de la théorie, laquelle prévoit un gain en intensité de $100\times$ pouvant être obtenue pour un réseau d'ouverture parfaitement en phase.

Mes travaux à IOTA permettent de désormais obtenir des images indirectes par la mesure des visibilités et clôtures de phase (Traub et al. 2003). Mesurer des clôtures de phase est moins contraignant que l'obtention d'images directes. Les faisceaux arrivant depuis différents télescopes ne nécessitent pas d'être cophasés. Il faut néanmoins que ces faisceaux soient en cohérence, puisque les phases des franges pour toutes les bases doivent être mesurées simultanément.

Ma contribution au projet IOTA était la construction d'un contrôleur pour la caméra proche infrarouge basé sur des modules CPLD, capables d'être reconfigurés en temps réel pour les différents modes de lecture envisagés pour la caméra. Nous avons, à IOTA, mesuré avec succès des interférogrammes triples (trois bases simultanément) pour des étoiles de magnitudes aussi faibles que $H \simeq 7$. Avec ce niveau de sensibilité, IOTA peut étendre son programme de recherche sur les étoiles évoluées et les objets stellaires jeunes en mode imageur avec l'utilisation des trois télescopes.

J'ai également réalisé, avec mes collaborateurs à IOTA, un suiveur de paquet de franges capable de maintenir les faisceaux en cohérence pour trois bases simultanément. Ce nouvel algorithme exploite l'information chromatique contenue dans le paquet de franges, qui est extraite par double interférométrie de Fourier. L'algorithme est capable de suivre en aveugle les franges sur une longueur de base avec un bas signal à bruit si les franges sur les autres bases de l'interféromètre ont un bon signal à bruit.

Le temps de cohérence τ_0 peut être déduit des données expérimentales. Ce paramètre est obtenu lorsque le suiveur de franges fonctionne en boucle ouverte et que les franges sont scannées dans des temps plus courts que la cohérence temporelle-même. Cela est très utile pour calculer l'erreur résiduelle introduite par le suiveur de paquet de franges et pour échantillonner le paquet des franges de manière optimale en accord avec les conditions de turbulence atmosphérique.

Finalement, j'ai participé à la réduction de données sur un échantillon d'étoiles Mira. L'interféromètre IOTA a obtenu des mesures de diamètres d'un grand échantillon d'étoiles variables de grandes périodes (Mira) dans l'infrarouge proche. Nous avons établi le rapport moyen des diamètres dans les bandes spectrales J, H et K et nous avons détecté une corrélation avec la phase de pulsation de ces étoiles.

Annexe A

Algorithmes de Phasage pour les Interféromètres à Plusieurs Éléments

Pedretti E. 1999, paru dans ASP Conf. Ser. **194** : *Working on the Fringe : Optical and IR Interferometry from Ground and Space*, 271

Résumé

L'interféromètre "Optical Very Large Array" (OVLA) et son précurseur , Micromegas, seront composés de 27 télescopes. Des images instantanées seront formées directement au foyer recombiné. Cela requerra une pupille de sortie densifiée et des faisceaux phasés pour toutes les longueurs d'onde utilisées. Je décris trois nouveaux algorithmes qui peuvent, en principe, phaser un interféromètre de ce type ; tous impliquent une hiérarchie de triplets d'ouvertures, mais utilisent des critères de phasage différents. Je compare ici leurs performances au moyen de simulations numériques qui prennent en compte le bruit de photons.

Mots clé : Interférométrie, co-phasage, traitement d'image .

Introduction

Cette publication est le résultats d'une présentation orale que j'ai donnée au colloque "Working on the Fringe", à Dana Point en Californie en Mai 1999. Cette conférence d'une semaine, sponsorisée par le JPL (Jet Propulsion Laboratory) et l'univeristé de Caltech, fut entièrement dédiée à l'interférométrie.

Cet article, similaire à celui présenté au chapitre 2 de ma thèse, est basé sur des logiciels de simulation identiques. La nouveauté de cet article est qu'il présente des estimateurs de phases différents, que j'ai également simulés. Je compare les résultats

de ces simulations avec ceux obtenus en utilisant les algorithmes hierarchiques pour un même ensemble de paramètres d'entrée.

Phasing algorithms for multi–element optical interferometers

Pedretti E. 1999, ASP Conf. Ser. **194** : *Working on the Fringe : Optical and IR Interferometry from Ground and Space*, 271

Abstract

The Optical Very Large Array (OVLA) and its precursor, Micromegas, will be composed of 27 telescopes. Snapshot images will be formed directly at the combined focus. This will require a densified exit pupil and phased beams for all the wavelengths used. I describe 3 novel algorithms which can, in principle, phase such an interferometer ; they all involve a hierarchy of aperture triplets but use different phasing criteria. I compare here their performance through numerical simulations and in the presence of photon noise.
keywords : Interferometry, co–phasing, image processing.

A.1 Introduction

New interferometry projects composed of several diluted apertures have been recently proposed ; they use phase closure, a technique widely applied in radio interferometry. Filled pupil interferometers like the Keck telescope obtain images in their recombined focus and use active and adaptive optics to phase the different elements (Chanan & Troy 1999). Instead, OVLA (Labeyrie et al. 1986) and Micromegas (Labeyrie 1998) will be diluted aperture interferometers, but will use adaptive optics to obtain images in the recombined focus using the "densified pupil" imaging technique (Labeyrie 1996).

Although it can work in speckle interferometry mode, a densified pupil interferometer will preferably need to be adaptively phased. The "hierarchical algorithm" (Pedretti & Labeyrie 1999) is possibly well suited for this purpose. In §2 I describe 3 methods which utilize different tests to achieve co–phasing. In §3 I compare the

performance of the 3 algorithms through numerical simulation. §4 provides a brief summary.

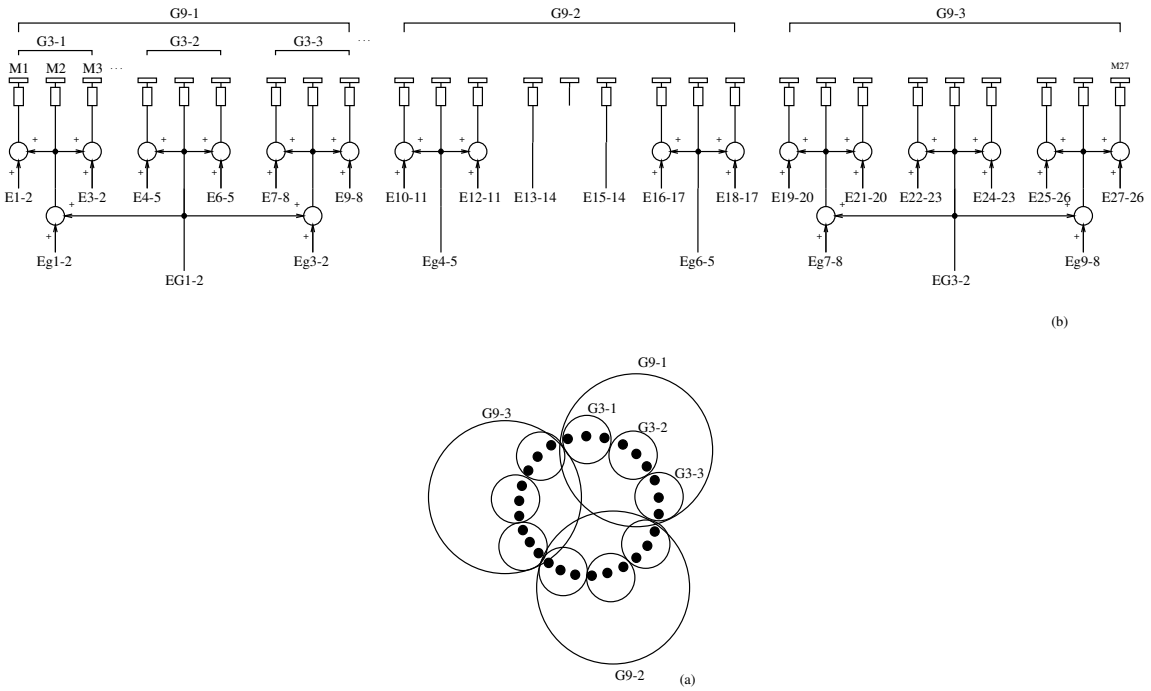

Fig. 1.1.— Hierarchical arrangement of actuators carrying 27 mirrors for phasing according to the triplet algorithm.

A.2 Algorithms

A.2.1 Image Sharpness Method

The hierarchical algorithm uses triplets of apertures as shown in Fig. 1a. For clarity, the system is sketched as a line array, with each mirror element mounted on an actuator, in Fig. 1b. The 27 mirrors are divided in triplets as 9 separate interferometers. In each triplet the phase of 2 apertures (eg. M1 and M3) is adjusted through the error signals (eg. E1-2 and E3-2) until the 3 apertures have the same phase. If the star is unresolved, centering the honeycomb fringe patterns, produced by the interference of 3 apertures, suffice for phasing each mirror triplet. The finer honeycomb from the triplet of triplets needs a different criterion : maximizing image sharpness (Muller & Buffington 1974). For example, G3-1 and G3-3 can be phased with G3-2 using the error signals Eg1-2 and Eg3-2, which are common to each actuator of the group. Once 3 groups of 9 mirrors are independently phased, the global phasing of 27 mirrors can be similarly obtained by applying piston corrections to both lateral groups of 9 mirrors, using the error signals EG1-2 and EG3-2. Phasing is achieved modulo 2π. This method, utilizing image sharpness, will be defined as “method 1”.

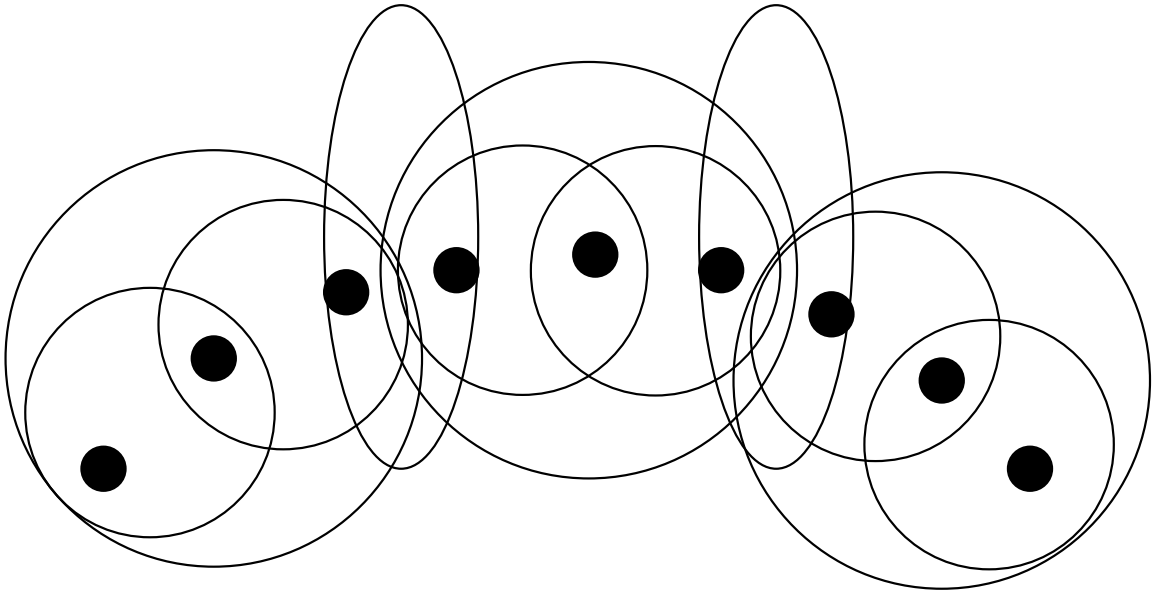

Fig. 1.2.— Each triplet is divided in 2 groups where beams are combined pairwise (small circles). Two different triplets are phased using the two boundary apertures (ellipses). The same concept is applied to co-phase the groups of 9 apertures (not shown).

A.2.2 Two-beam Combination

There are alternative criteria which can replace image sharpness in the hierarchical algorithm. In a triplet, 2 beams can be combined separately as shown in Fig. 1.2 in order to obtain fringes. Modulo 2π phases can be obtained measuring the shift of the monochromatic images of the fringes at different wavelengths.

Also established techniques such as dispersed fringe tracking (Koechlin et al. 1996) could, in principle, be used to co–phase couples of apertures, although a large optical bandwidth is necessary to obtain enough precision for phasing.

Once all the triplets are phased two nearby groups of 3 apertures can be phased using the fringes obtained from 2 adjacent apertures, which are part of different triplets (apertures enclosed by the ellipses in Fig. 1.2). The same method is repeated for the groups of 9 apertures. Again the adjacent apertures of 2 groups of 9 are combined to obtain the phase difference between different groups. I will call this "method 2".

A.2.3 Fourier Transform Method

The Fourier transform of the globally combined monochromatic image of a densified pupil (which is the autocorrelation function, ACF, of the pupil) can also be

used in order to measure the phase difference between couples of apertures if the apertures are non–redundant. If the object is not resolved (Fig 1.3a), the system is fully determined and the correlation peaks contain the information of the difference between each combination of 2 apertures. When the object is resolved (Fig 1.3b), the

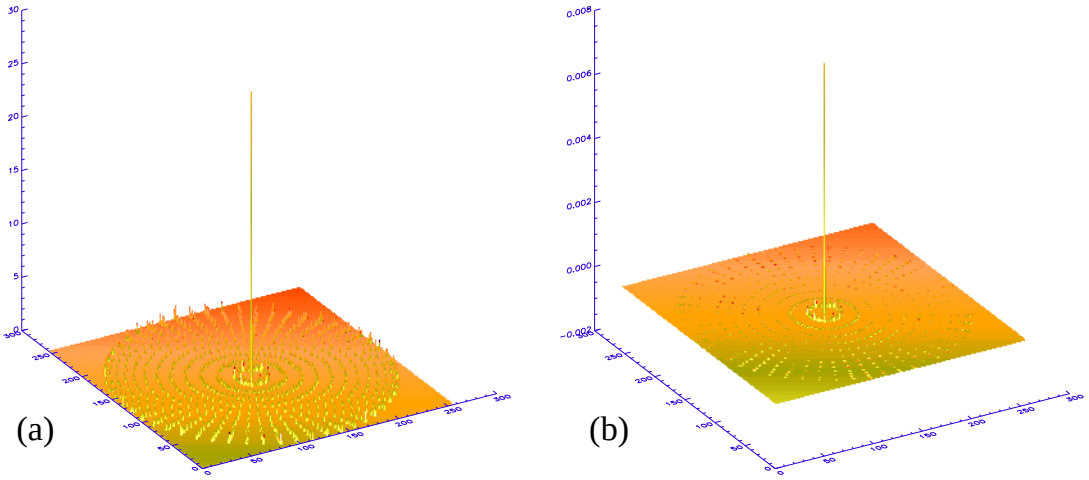

Fig. 1.3.— The ACF of a 27 aperture diluted interferometer when (a) the object is unresolved and (b) the object is resolved. Note that in the case of a resolved object only the smallest ring of correlation peaks is visible.

more external peaks are less visible, depending on how resolved the object is. At the limit only the central ring, containing the difference between nearby apertures, can be exploited. This can be used for the hierarchical algorithm in the same way as the autocorrelation of 2 apertures.

A Fourier transform of the image would suffice to obtain the phases. A densified pupil configuration is not usable here since the correlation peaks would be too large and would superpose, causing the phase information to become unreadable. In this case another camera should be used for phasing. In such a camera the pupil should be re-imaged to be non-densified. I will call this "method 3".

A.2.4 Optical path calculation

Once monochromatic phases are obtained the optical path difference (OPD) can be calculated for each different wavelength. One needs to solve for the value of the integer k in Eq. A.1 to calculate the path difference in white light.

$$\delta_n = (k + \epsilon_n)\lambda_n, \tag{A.1}$$

where $\epsilon_n = \phi_n/2\pi$, λ_n is the wavelength and ϕ_n the monochromatic phase. The integral fringe k is varied until the OPDs δ_n are the same for all wavelengths.

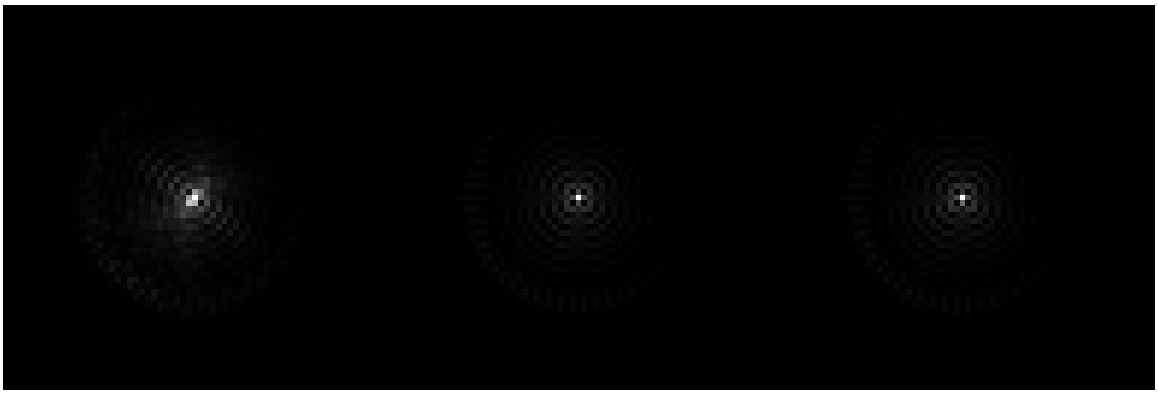

Fig. 1.4.— With a high photon count (30,000,000 for 8 wavelengths and a bandwidth of $10nm$) method 1 produced a Strehl ratio of 0.52 (left), while method 2, a Strehl of 0.99 (centre) and method 3 (right), a Strehl of 0.98.

A.3 Comparison

I compared, through numerical simulation, method 1, 2 and 3. The simulation was performed in identical conditions of object, phase distribution, number of photons, etc. Photon noise was also added to the simulations in order to test the convergence of the algorithms when the photon count is low. I performed a test using an unresolved

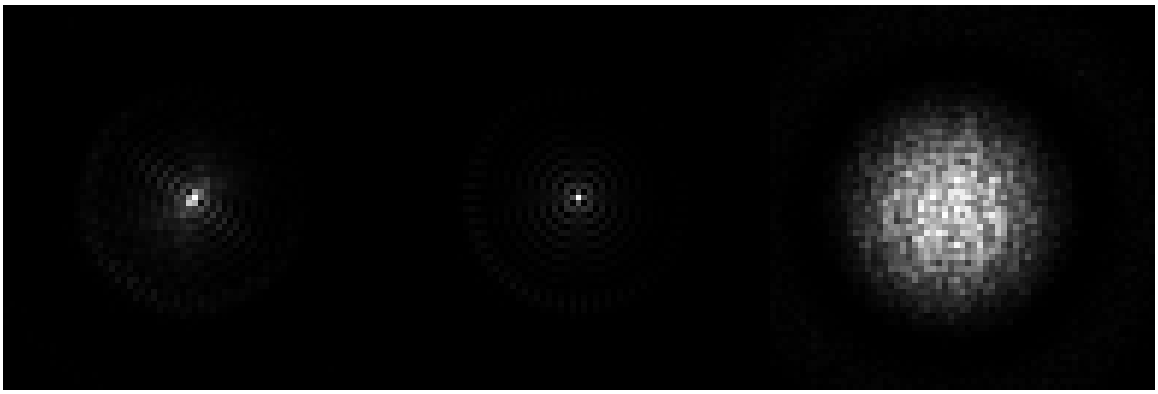

Fig. 1.5.— The photon count is reduced to 30,000. The performance is un-affected for method 1 and 2, but drops to a Strehl of 0.06 for method 3.

object and running the algorithm for 8 different wavelengths and for different photon counts (Figs. 1.4 & 1.5).

When the test was performed at low photon counts (Fig. 1.5), method 3 produced a Strehl ratio of 0.06, very different from the value obtained with 30,000,000 photons (Strehl = 0.98). These results can be qualitatively explained by comparing the distribution of energy in the ACF of 2 apertures and 27 apertures. If an array is composed of n non-redundant apertures, the autocorrelation peak will be composed of a central peak n times the height of the side peaks with $n(n-1)$ side peaks. If the

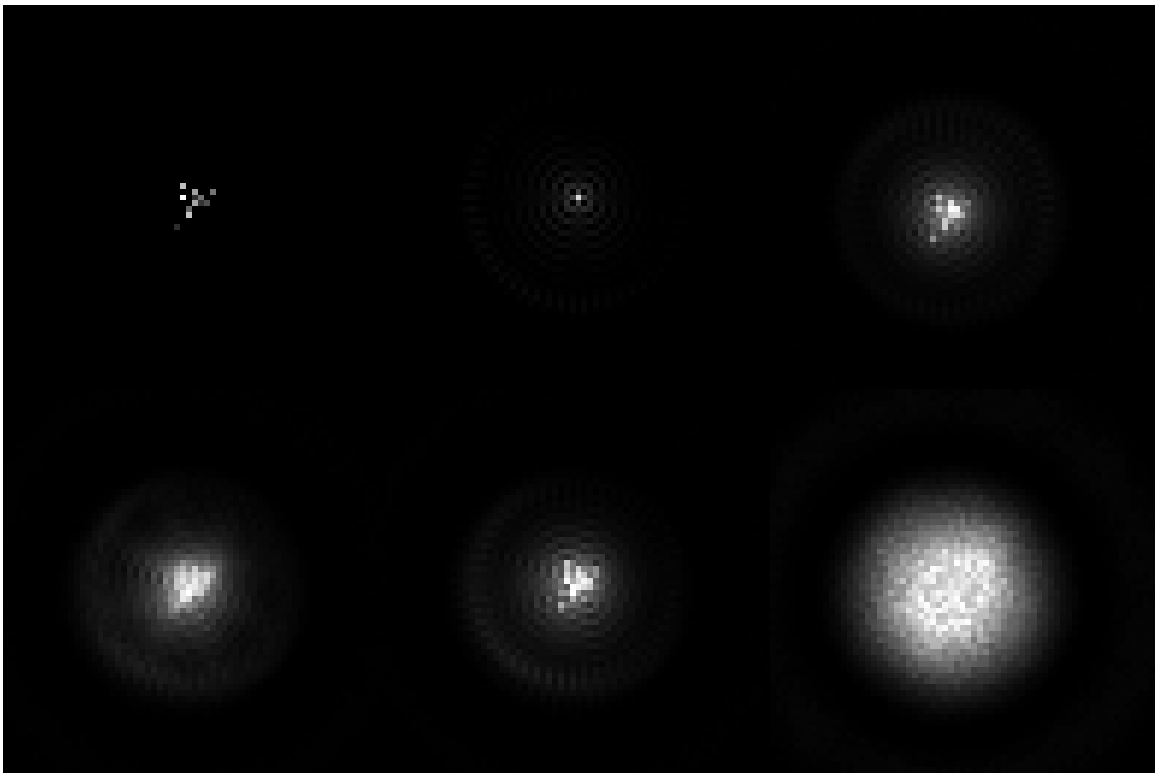

Fig. 1.6.— Simulation of a "star cluster" (top–left) composed of 13 stars of different magnitudes and spectral distributions. From left to right (top) shows the response of the interferometer to a point object (center) and the image obtained at the output of the interferometer (right), when the apertures are co–phased. Method 1 produced a Strehl ratio of 0.31 (bottom–left), while method 2, a Strehl of 0.62 (center) and for method 3 (right), a Strehl of 0.07.

sum of all the energy in the ACF is a constant k there will be k/n^2 of this energy in the side peaks and k/n in the central peak. For 2 apertures there will be $k/4$ on the side peaks and $k/2$ in the central peak. With 27 apertures, only $k/729$ energy will be present in the side peaks and $k/27$ in the central peak.

The limiting magnitude can be calculated (Muller & Buffington 1974). With p photons received from the N–element aperture in time τ, corresponding to the seeing time scale, the incident photon flux per square centimeter is $B = 4p/(\pi d^2 \tau N \eta)$ and the stellar magnitude is $m_v = 2.5 \log(734\ \delta\lambda/B)$. d is the size of the sub–aperture elements in centimeters, η the overall quantum efficiency, and $\delta\lambda$ the bandwidth in Angström units. The limiting magnitude found with 27 apertures of 10cm, a seeing time scale of 0.02s, $\eta = 0.1$ and 300nm optical bandwidth is 7 mag, with $p = 14000$, for method 1. For method 2, a more sensitive limiting magnitude of 8 mag is obtained, with $p = 5500$.

It should be noted that the OPD can be calculated from Eq. A.1 with just 3 broad-band wavelengths, achieving much higher sensitivity due the large number of

photons involved. Coherence can be achieved using a larger number of wavelengths and integrating for a time longer than τ. The different wavelengths can then be binned to 3 broad-band wavelengths, which will achieve phasing with higher sensitivity.

An object simulating a cluster of 13 stars composed of a random distribution of 8 wavelengths was also tested (Fig. 1.6). For resolved objects the phasing is also achieved but a larger number of photons is required.

A.4 Conclusions and Future work

Although all the algorithms tested converge to equalized phases the comparison shows that the algorithm employing method 2 produces a gain of at least one magnitude with respect to image sharpness. This is obtained with an increase in the complexity of the optical system. The Fourier transform of the direct combined image (method 3) is easier to implement but comparison showed poor performance in terms of photon efficiency. An optical phasing simulator is under construction at Haute Provence in order to test these results and to show images obtained by a densified pupil imaging system.

Acknowledgments

I would like to thank Antoine Labeyrie for many useful comments and fruitful discussion during the preparation of this manuscript. I thank Lisa Prato for her kind offer to proof read the final version of this paper.

Annexe B

Dérivation de l'Équation 7.25

Je dérive ici la variance de la phase pour une frange en présence de bruit de détecteur en accord avec la dérivation de Walkup & Goodman (1973) et je rajoute une composante due au bruit de détecteur x_d dans la dérivation. Les hypothèses de départ sont que nous travaillons avec une frange monochromatique qui comprend plusieurs périodes entières. Je réécris Eqn. 6.1 pour le cas monochromatique (j'enleve le terme en sinc) et pour une série temporelle discrète de données.

$$\overline{n}(j) = x_s \left[1 + V_s \sin\left(\frac{2\pi j m_0}{N} + \phi\right)\right] + x_b \tag{B.1}$$

où $\overline{n}(j)$ est le nombre moyen de photo-évènements enregistrés par le photo-détecteur, j est le nombre d'échantillons , m_0 la fréquence spatiale discrète , N le nombre d'échantillons, x_s l'intensité discrète qui dépend de I_s, V_s la visibilité et x_b le bruit de fond. Il est plus approprié de réécrire Eqn. B.1 comme fonction de l'intensité totale $x_t = x_s + x_b$ et la visibilité apparente $V = x_s V_s / (x_s + x_b)$. L'équation devient

$$\overline{n}(j) = x_t \left[1 + V \sin\left(\frac{2\pi j m_0}{N} + \phi\right)\right]. \tag{B.2}$$

L'erreur sur la phase est donnée avec une bonne approximation par l'inverse du rapport signal à bruit de l'estimateur de phase, qui est la transformée de Fourier des données acquises comme série temporelle. Je calcule le signal à partir de la partie réelle et de la partie imaginaire de la transformée de Fourier de $n(j)$:

$$\begin{array}{ll} \overline{R}(m_0) & = \frac{1}{N} \sum_{j=0}^{N-1} \overline{n}(j) \cos\left(\frac{2\pi j m_0}{N}\right) \\ \overline{I}(m_0) & = \frac{1}{N} \sum_{j=0}^{N-1} \overline{n}(j) \sin\left(\frac{2\pi j m_0}{N}\right) \end{array} . \tag{B.3}$$

Je substitue $n(j)$ pour une seule longueur d'onde dans la transformée de Fourier réelle :

$$R(m_0) = \frac{1}{N} \sum_{j=0}^{N-1} x_t \left[1 + V \sin\left(\frac{2\pi j m_0}{N} + \phi\right)\right] \cos\left(\frac{2\pi j m_0}{N}\right) \tag{B.4}$$

Je développe Eqn. B.4 sachant que $\sum_{j=0}^{N-1} x_t \cos\left(\frac{2\pi j m_0}{N}\right)$ pour un nombre entier de longueur d'onde est équivalente à l'intégrale continue dans sur la période $\int_0^{2\pi} x_t \cos\left(\frac{2\pi j m_0}{N}\right) dm_0$ qui est égale à zéro.

$$\begin{aligned}
\overline{R}(m_0) &= \tfrac{1}{N}\sum_{j=0}^{N-1} x_t \cos\left(\tfrac{2\pi j m_0}{N}\right) + x_t V \cos\left(\tfrac{2\pi j m_0}{N}\right)\sin\left(\tfrac{2\pi j m_0}{N}+\phi\right) \\
&= \tfrac{1}{N}\sum_{j=0}^{N-1} x_t V \sin\left(\tfrac{2\pi j m_0}{N}\right)\cos\left(\tfrac{2\pi j m_0}{N}\right)\cos(\phi) + x_t V \cos\left(\tfrac{2\pi j m_0}{N}\right)\cos\left(\tfrac{2\pi j m_0}{N}\right)\sin(\phi) \\
&= \tfrac{1}{N}\sum_{j=0}^{N-1} x_t V \tfrac{1}{2}\sin\left(\tfrac{4\pi j m_0}{N}\right)\cos(\phi) + x_t V\left[\tfrac{1}{2}+\tfrac{1}{2}\cos\left(\tfrac{4\pi j m_0}{N}\right)\right]\sin(\phi)
\end{aligned} \tag{B.5}$$

J'obtiens à nouveau des fonctions sinus et cosinus de périodes entières dont la somme est égale à zéro, ce qui simplifie la partie réelle maintenant égale à :

$$\begin{aligned}
\int_0^{2\pi} \sin\left(\tfrac{4\pi j m_0}{N}\right) dm_0 &= 0 \\
\int_0^{2\pi} \cos\left(\tfrac{4\pi j m_0}{N}\right) dm_0 &= 0 \\
\overline{R}(m_0) = \tfrac{1}{2} x_s V_s \sin(\phi)
\end{aligned} \tag{B.6}$$

de la même manière, j'obtiens pour la partie imaginaire :

$$\overline{I}(m_0) = \frac{1}{2} x_s V_s \cos(\phi) \tag{B.7}$$

J'ai calculé le signal pour l'estimation du signal à bruit (SNR), je dois maintenant calculer le bruit. La variance de la partie réelle est égale à la variance de la partie imaginaire. Dans ce cas cette variance contient une composante due à la statistique de Poisson, $\sqrt{\overline{n}_j}$ et une composante due au bruit de détecteur x_d. J'écris le bruit σ comme racine carrée de la somme quadratique de la variance du bruit de Poisson, qui est le nombre moyen de photo-électrons $\overline{n}(j)$, et x_d^2, la variance du bruit de détecteur. Je prends ensuite le carré de la partie réelle de la transformée de Fourier $\sigma^2[\overline{R}(m_0)]$ du bruit afin d'obtenir la variance :

$$\begin{aligned}
\sigma &= \sqrt{x_d^2 + \overline{n}(j)} \\
\sigma^2[R(m_0)] &= \sigma^2[I(m_0)] \\
\sigma^2[R(m_0)] &= \tfrac{1}{N^2}\sum_{j=0}^{N-1}\left[\sqrt{x_d^2+\overline{n}(j)}\cos\left(\tfrac{2\pi j m_0}{N}\right)\right]^2
\end{aligned} \tag{B.8}$$

je développe Eqn. B.8 en rappelant que $\cos^2\left(\frac{2\pi j m_0}{N}\right) = \frac{1}{2} + \frac{1}{2}\cos\left(\frac{4\pi j m_0}{N}\right)$:

$$\begin{aligned}
\sigma^2[R(m_0)] &= \tfrac{1}{N^2}\sum_{j=0}^{N-1} x_d^2 \cos^2\left(\tfrac{2\pi j m_0}{N}\right) + \tfrac{1}{N^2}\sum_{j=0}^{N-1}\overline{n(j)}\cos^2\left(\tfrac{2\pi j m_0}{N}\right) \\
&= \tfrac{1}{2N}x_d^2 + \tfrac{1}{2N^2}\sum_{j=0}^{N-1} x_d^2 \cos\left(\tfrac{4\pi j m_0}{N}\right) + \tfrac{1}{2N}x_t \\
&= \tfrac{1}{2N}x_d^2 + \tfrac{1}{2N}x_t
\end{aligned} \tag{B.9}$$

sachant que :

$$\frac{1}{N^2}\sum_{j=0}^{N-1}\overline{n}(j)\cos^2\left(\frac{2\pi j m_0}{N}\right) = \frac{1}{N^2}\sum_{j=0}^{N-1}\frac{1}{2}\overline{n}(j) \tag{B.10}$$

et :

$$\frac{1}{N^2}\sum_{j=0}^{N-1}\frac{1}{2}\overline{n}(j) = \frac{1}{N^2}\sum_{j=0}^{N-1}\frac{1}{2}x_t + \frac{1}{2}x_t V \sin\left(\frac{2\pi j m_0}{N}+\phi\right). \tag{B.11}$$

la somme des fonctions $\sin\left(\frac{2\pi jm_0}{N}+\phi\right) = \sin\left(\frac{2\pi jm_0}{N}\right)\cos(\phi) + \cos\left(\frac{2\pi jm_0}{N}\right)\sin(\phi)$ en Eq. B.11 est égale à zéro.

$$\frac{1}{N^2}\sum_{j=0}^{N-1}\overline{n}(j)\cos^2\left(\frac{2\pi jm_0}{N}\right) = \frac{1}{2N}x_t. \tag{B.12}$$

Le rapport signal à bruit (SNR) est donc :

$$\begin{aligned} SNR &= \left[\frac{\overline{Re^2(m_0)}+\overline{Im^2(m_0)}}{\sigma^2(m_0)}\right]^{\frac{1}{2}} \\ &= \sqrt{\frac{Nx_t}{2}}\frac{x_t V\left[\cos^2(\phi)+\sin^2(\phi)\right]^{\frac{1}{2}}}{x_d+x_t} \\ &= \sqrt{\frac{Nx_t}{2}}\frac{V}{\left(1+\frac{x_d^2}{x_t}\right)} \end{aligned} \tag{B.13}$$

L'erreur au carré moyenne sur la phase $\langle\Delta\phi^2\rangle$ est approximativement égale à $1/SNR^2$

$$\left\langle\Delta\phi^2\right\rangle \cong \frac{2\left(1+\frac{x_d^2}{x_t}\right)}{V^2Nx_t}. \tag{B.14}$$

Bibliographie

Angel, J. R., Burge, J. H., & Woolf, N. J. 1997, Proceedings of SPIE, 2871, 516

Bacon, R., Adam, G., Baranne, A., Courtes, G., Dubet, D., Dubois, J. P., Emsellem, E., Ferruit, P., Georgelin, Y., Monnet, G., Pecontal, E., Rousset, A., & Say, F. 1995, A&AS, 113, 347

Baldwin, J. E., Beckett, M. G., Boysen, R. C., Burns, D., Buscher, D. F., Cox, G. C., Haniff, C. A., Mackay, C. D., Nightingale, N. S., Rogers, J., Scheuer, P. A. G., Scott, T. R., Tuthill, P. G., Warner, P. J., Wilson, D. M. A., & Wilson, R. W. 1996, A&A, 306, L13+

Baldwin, J. E., Haniff, C. A., Mackay, C. D., & Warner, P. J. 1986, Nature, 320, 595

Baldwin, J. E., Tubbs, R. N., Cox, G. C., Mackay, C. D., Wilson, R. W., & Andersen, M. I. 2001, A&A, 368, L1

Baldwin, J. E. & Warner, P. J. 1987, Nature, 328, 694

Beckers, J. M. 1986, Proceedings of SPIE, 628, 255

—. 1993, ARA&A, 31, 13

Berger, J. P., Haguenauer, P., Kern, P., Perraut, K., Malbet, F., Schanen, I., Severi, M., Millan-Gabet, R., & Traub, W. 2001, A&A, 376, L31

Berger, J. P., Haguenauer, P., Kern, P. Y., Perraut-Rousselet, K., Malbet, F., Gluck, S., Lagny, L., Shanen, I., E., L., Delboulbe, A., Tatulli, E., Traub, W. A., Carleton, N. P., Millan-Gabet, R., Monnier, J. D., & Pedretti, E. 2003, in Proc. SPIE, Interferometry for Optical Astronomy, Wesley A. Traub, editor, Vol. 4838, 1099–1106

Bevington, P. R. & Robinson, D. K. 1992, Data reduction and error analysis for the physical sciences (New York : McGraw-Hill, —c1992, 2nd ed.)

Boccaletti, A., Riand, P., Moutou, C., & Labeyrie, A. 2000, Icarus, 145, 628

Borkowski, V., Martinache, F., Peterson, D., & Labeyrie, A. 2002, in Earth-like planets and moons. Proceedings of the 36th ESLAB Symposium, 3 - 8 June 2002, ESTEC, Noordwijk, The Netherlands. Eds. : B. Foing, B. Battrick. ESA SP-514,

Noordwijk : ESA Publications Division, ISBN 92-9092-824-7, 2002, p. 273 - 276, 273–+

Born, M. & Wolf, E., eds. 1999, Principles of optics : electromagnetic theory of propagation, interference and diffraction of light

Brown, R. H. & Twiss, R. Q. 1958, Royal Society of London Proceedings Series A, 248, 199

Buscher, D. F. 1988, Ph.D. Thesis

Buscher, D. F., Baldwin, J. E., Warner, P. J., & Haniff, C. A. 1990, MNRAS, 245, 7P

Cabelli, C. A., Cooper, D. E., Haas, A. K., Kozlowski, L. J., Bostrup, G. L., Chen, A. C., Blackwell, J. D., Montroy, J. T., Vural, K., Kleinhans, W. E., Hodapp, K., & Hall, D. N. 2000, in Proc. SPIE, Infrared Detectors and Focal Plane Arrays VI, Eustace L. Dereniak ; Robert E. Sampson ; Eds., Vol. 4028, 331–342

Chagnon, G., Mennesson, B., Perrin, G., Coudé du Foresto, V., Salomé, P., Bordé, P., Lacasse, M., & Traub, W. 2002, AJ, 124, 2821

Chanan, G. & Troy, M. 1999, Appl. Opt., 38, 6642

Chesneau, O., Roche, M., Boccaletti, A., Abe, L., Moutou, C., Charbonnier, F., Aime, C., Lantéri, H., & Vakili, F. 2000, A&AS, 144, 523

Chin, G. & Gezari, D. 1987, in Infrared astronomy with arrays, 160–+

Cohen, M. 1980, MNRAS, 191, 499

Coldwell, C. M., Papaliolios, C. D., & Traub, W. A. 1998, in Proc. SPIE, Astronomical Interferometry, Robert D. Reasenberg ; Ed., Vol. 3350, 424–431

Danchi, W. C., Tuthill, P. G., & Monnier, J. D. 2001, ApJ, 562, 440

de Batz, B., Granes, P., Gay, J., & Journet, A. 1973, Nature Physical Science, 245, 89

Domiciano, A., Kervella, P., Jankov, S., Abe, L., Vakili, F., di Folco, E., & Paresce, F. 2003, in SF2A-2003 : Semaine de l'Astrophysique Française, meeting held in Bordeaux, France, June 16-20, 2003. Eds. : F. Combes, D. Barret and T. Contini. EdP-Sciences, Conference Series, p. 217.

Dugue, M., Labeyrie, A., & Schumacher, G. 1983, in ESO's Very Large Telescope, 141–154

Fischer, J., Vrba, F. J., Toomey, D. W., Lucke, B. L., Wang, S., Henden, A. A., Robichaud, J. L., Onaka, P. M., Hicks, B., Harris, F. H., Stahlberger, W. E., Kosakowski, K. E., Dudley, C. C., & Johnston, K. J. 2003, in Instrument Design and Performance for Optical/Infrared Ground-based Telescopes. Edited by Iye, Masanori ; Moorwood, Alan F. M. Proceedings of the SPIE, Volume 4841, pp. 564-577 (2003)., 564–577

Fizeau, H. 1868, C. R. Acad. Sci., 66, 932

Freytag, B. 2003, in Interferometry for Optical Astronomy II. Edited by Wesley A. Traub. Proceedings of the SPIE, Volume 4838, pp. 348-357 (2003)., 348–357

Fried, D. L. 1966, Optical Society of America Journal, 56, 1372

Gillet, S., Riaud, P., Lardière, O., Dejonghe, J., Schmitt, J., Arnold, L., Boccaletti, A., Horville, D., & Labeyrie, A. 2003, A&A, 400, 393

Gilmozzi, R., Delabre, B., Dierickx, P., Hubin, N., Koch, F., Monnet, G., Quattri, M., Rigaut, F., & Wilson, R. 1998, in Advanced Technology Optical/IR Telescopes VI, ed. L. M. S. E., Vol. SPIE 3352, 778–791

Hamaker, J. P., Osullivan, J. D., & Noordam, J. E. 1977, Optical Society of America Journal, 67, 1122

Hamblen, J. O. & Furnan, M. D. 2000, Rapid prototyping of digital system (Kluwer Academic Publishers, Boston / Dordrecht / London)

Hanbury Brown, R., Davis, J., & Allen, L. R. 1974, MNRAS, 167, 121

Hecht, E. & Zajac, A. 1974, Optics (Addison-Wesley Series in Physics, Reading, Mass. : Addison-Wesley, 1974)

Hillenbrand, L. A., Strom, S. E., & Vrba, F. J. a. 1992, ApJ, 397, 613

Hofmann, K.-H., Beckmann, U., Blöcker, T., Coudé du Foresto, V., Lacasse, M., Mennesson, B., Millan-Gabet, R., Morel, S., Perrin, G., Pras, B., Ruilier, C., Schertl, D., Schöller, M., Scholz, M., Shenavrin, V., Traub, W., Weigelt, G., Wittkowski, M., & Yudin, B. 2002, New Astronomy, 7, 9

Jennison, R. C. 1958, MNRAS, 118, 276

Joven-Alvarez, E., Rodriguez-Ramos, L. F., Diaz, J. J., Rodriguez-Mora, A., Sosa, N. A., Williams, M. R., Fuentes, F. J., Cadavid, E., Manescau, A., Sanchez, V., Paez, E., Martin, C., Espinosa, J. M., Hammersley, P., & Gonzalez, J. C. 1994, in Proc. SPIE Vol. 2225, p. 193-204, Infrared Detectors and Focal Plane Arrays III, Eustace L. Dereniak ; Robert E. Sampson ; Eds., 193–204

Kervella, P., Coudé du Foresto, V., Perrin, G., Schöller, M., Traub, W. A., & Lacasse, M. G. 2001, A&A, 367, 876

Koechlin, L., Lawson, P. R., Mourard, D., Blazit, A., Bonneau, D., Morand, F., Stee, P., Tallon-Bosc, I., & Vakili, F. 1996, Appl. Opt., 35, 3002

Kozlowski, L. J., Montroy, J. T., Cabelli, C. A., Cooper, D. E., Chen, A. C., Bostrup, G. L., Bai, Y., Vural, K., Hodapp, K., & Hall, D. N. 2000, in Proc. SPIE, Optical and IR Telescope Instrumentation and Detectors, Masanori Iye ; Alan F. Moorwood ; Eds., Vol. 4008, 1240–1253

Labeyrie, A. 1970, A&A, 6, 85

—. 1975, ApJ, 196, L71

Labeyrie, A. 1985, in Kilometric Optical Arrays in Space, 117–119

—. 1996, A&AS, 118, 517

Labeyrie, A. 1998, in Proc. SPIE Vol. 3350, p. 960-972, Astronomical Interferometry, Robert D. Reasenberg ; Ed., 960–972

Labeyrie, A. 1999, in NATO ASIC Proc. 532 : Planets Outside the Solar System : Theory and Observations, 261–+

Labeyrie, A., Koechlin, L., & Lemaitre, G. 1986, in Advanced technology optical telescopes III ; Proceedings of the Meeting, Tucson, AZ, Mar. 3-6, 1986 (A87-35201 15-89). Bellingham, WA, Society of Photo-Optical Instrumentation Engineers, 1986, p. 323-332., 323–332

Lançon, A. & Wood, P. R. 2000, A&AS, 146, 217

Lattanzi, M. G., Munari, U., Whitelock, P. A., & Feast, M. W. 1997, ApJ, 485, 328

Lawson, P. R. 1995, Optical Society of America Journal, 12, 366

Lawson, P. R., ed. 2000, Principles of Long Baseline Stellar Interferometry

Mariotti, J.-M. & Ridgway, S. T. 1988, A&AS, 195, 350

McLean, I. S., Becklin, E. E., Brims, G., Canfield, J., Casement, L. S., Figer, D. F., Henriquez, F., Huang, A., Liu, T., Macintosh, B. A., & Teplitz, H. 1993, in Proc. SPIE Vol. 1946, p. 513-533, Infrared Detectors and Instrumentation, Albert M. Fowler ; Ed., 513–533

McLean, I. S., Macintosh, B. A., Liu, T., Casement, L. S., Figer, D. F., Lacayanga, F., Larson, S., Teplitz, H., Silverstone, M., & Becklin, E. E. 1994, in Proc. SPIE Vol. 2198, p. 457-466, Instrumentation in Astronomy VIII, David L. Crawford ; Eric R. Craine ; Eds., 457–466

Mendoza, V. E. E. 1966, ApJ, 143, 1010

Mennesson, B., Perrin, G., Chagnon, G., Foresto, V. C. d., Ridgway, S., Merand, A., Salome, P., Borde, P., Cotton, W., Morel, S., Kervella, P., Traub, W., & Lacasse, M. 2002, ApJ, 579, 446

Michelson, A. A. 1891, PASP, 3, 274

Michelson, A. A. & Pease, F. G. 1921a, Measurement of the diameter of a Orionis with interferometer ([Chicago, 1921]), 3–+

—. 1921b, "Measurement of the diameter of a Orionis with interferometer" ([Chicago, 1921]), 03...+

—. 1921c, ApJ, 53, 249

—. 1923, Popular Astronomy, 31, 14

Millan-Gabet, R. 1999, Ph.D. Thesis, University of Massachusetts

Millan-Gabet, R., Pedretti, E., Monnier, J. D., Traub, W. A., Schloerb, F. P., Carleton, N. P., Ragland, S., Lacasse, M. G., Danchi, W. C., Tuthill, P., Perrin, G., & Coudé du Foresto, V. 2003, in Proc. SPIE, Interferometry for Optical Astronomy, Wesley A. Traub, editor, Vol. 4838, 202–209

Millan-Gabet, R., Schloerb, F. P., Traub, W. A., & Carleton, N. P. 1999a, PASP., 111, 238

Millan-Gabet, R., Schloerb, F. P., Traub, W. A., Malbet, F., Berger, J. P., & Bregman, J. D. 1999b, ApJ, 513, L131

Miroshnichenko, A., Ivezic, Z., & Elitzur, M. 1997, ApJ, 475, L41+

Monnier, J. D., Berger, J. P., Millan-Gabet, R., Traub, W. A., Carleton, N. P., Pedretti, E., Coldwell, C. M., & Papaliolios, C. D. 2003a, in Proc. SPIE, Interferometry for Optical Astronomy, Wesley A. Traub, editor, Vol. 4838, 1127–1138

Monnier, J. D., Millan-Gabet, R., Tuthill, P. G., Traub, W. A., Carleton, N. P., Coude du Foresto, V., Danchi, W. C., Lacasse, M. G., Morel, S., Perrin, G., & Porro, I. 2003b, in Proc. SPIE, Interferometry for Optical Astronomy, Wesley A. Traub, editor, Vol. 4838, 379–386

Morel, S. & Koechlin, L. 1998, in Proc. SPIE Vol. 3350, p. 1057-1064, Astronomical Interferometry, Robert D. Reasenberg ; Ed., 1057–1064

Muller, R. A. & Buffington, A. 1974, Optical Society of America Journal

Nisenson, P. & Traub, W. 1987, in Interferometric Imaging in Astronomy, 129–+

Ohnaka, K., Beckman, U., Berger, J. P., Brewer, M. K., Hofmann, K., Lacasse, M. G., Malanushenko, V., Millan-Gabet, R., Pedretti, E., Monnier, J. D., Schertl, D., Schloerb, F. P., Shenavrin, V., & Traub, W. A. 2003, in Proc. SPIE, Interferometry for Optical Astronomy, Wesley A. Traub, editor, Vol. 4838, 1068–1071

Pease, F. G. 1931, Ergebnisse der Exacten Naturwissenschaften, 10, 84

Pedretti, E. 1999, in ASP Conf. Ser. 194 : Working on the Fringe : Optical and IR Interferometry from Ground and Space, 271–+

Pedretti, E. & Labeyrie, A. 1999, A&AS, 137, 543

Pedretti, E., Millan-Gabet, R., Monnier, J. D., Morel, S., Traub, W. A., Carleton, N. P., Berger, J. P., Schloerb, F. P., Brewer, M. K., Ragland, S., & Lacasse, M. G. 2002, in Proc. SPIE, Interferometry for Optical Astronomy, Wesley A. Traub editor, Vol. 4838, 943–955

Pedretti, E., Monnier, J. D., & Traub, W. A. 2003, In preparation

Porro, I. L., Traub, W. A., & Carleton, N. P. 1999, Appl. Opt., 38, 6055

Probst, R. G., Ellis, T. A., Fowler, A. M., Gatley, I., Heim, G. B., & Merrill, K. M. 1994, in Proc. SPIE Vol. 2198, p. 695-702, Instrumentation in Astronomy VIII, David L. Crawford ; Eric R. Craine ; Eds., 695–702

Rabbia, Y., Menardi, S., Gay, J., Bourlon, P. M., Antonelli, P., Dugue, M., Marchal, J., Reynaud, F., Faucherre, M., & Hubin, N. 1994, in Proc. SPIE Vol. 2200, p. 204-215, Amplitude and Intensity Spatial Interferometry II, James B. Breckinridge ; Ed., 204–215

Ragland, S., Traub, W. A., Millan-Gabet, R., Carleton, N. P., & Pedretti, E. 2002, in Proc. SPIE, Interferometry for Optical Astronomy, Wesley A. Traub, editor, Vol. 4838, 1225–1233

Riaud, P. 2003, PhD thesis, Université de Paris - Pierre & Marie Curie

Riaud, P., Boccaletti, A., Gillet, S., Schneider, J., Labeyrie, A., Arnold, L., Baudrand, J., Lardiè, O., Dejonghe, J., & Borkowski, V. 2002, A&A, 396, 345

Ribak, E. N., Adler, J., & Lipson, S. G. 1990, in Proc. SPIE Vol. 1237, p. 574-584, Amplitude and Intensity Spatial Interferometry, James B. Breckinridge ; Ed., 574–584

Robbe, S., Sorrente, B., Cassaing, F., Rabbia, Y., Rousset, G., Dame, L., Cruzalebes, P., & Schumacher, G. 1994, in Proc. SPIE Vol. 2200, p. 222-230, Amplitude and Intensity Spatial Interferometry II, James B. Breckinridge ; Ed., 222–230

Roddier, F. 1999, Adaptive optics in astronomy (Adaptive optics in astronomy / edited by Francois Roddier. Cambridge ; New York, NY : Cambridge University Press, 1999, ISBN 052155375X)

Roddier, F. & Roddier, C. 1991, Appl. Opt., 30, 1325

Schwarzschild, M. 1975, ApJ, 195, 137

Shack, R. B. & Platt, B. C. 1971, Optical Society of America Journal

Stéphan, E. 1873, C. R. Acad. Sci., 76, 1008

—. 1874, C. R. Acad. Sci., 78, 1008

Steward, E. G. 1989, Appl. Opt., 28, 1880

Sutton, E. C., Betz, A. L., Townes, C. H., & Spears, D. L. 1976, BAAS, 8, 525

Tallon, M. & Tallon-Bosc, I. 1992, A&A, 253, 641

Thompson, A. R., Moran, J. M., & Swenson, G. W. 2001, Interferometry and synthesis in radio astronomy (Interferometry and synthesis in radio astronomy by A. Richard Thompson, James M. Moran, and George W. Swenson, Jr. 2nd ed. New York : Wiley, c2001.xxiii, 692 p. : ill. ; 25 cm. "A Wiley-Interscience publication." Includes bibliographical references and indexes. ISBN : 0471254924)

Thompson, R. R., Creech-Eakman, M. J., & van Belle, G. T. 2003, in Interferometry for Optical Astronomy II. Edited by Wesley A. Traub. Proceedings of the SPIE, Volume 4838, pp. 221-234 (2003)., 221–234

Thureau, N. D. 2001, PhD thesis, Université de Nice-Sophia Antipolis - Faculté des sciences

Thureau, N. D., Boysen, R. C., Buscher, D. F., Haniff, C. A., Pedretti, E., Warner, P. J., & Young, J. S. 2003, in Interferometry for Optical Astronomy II. Edited by Wesley A. Traub . Proceedings of the SPIE, Volume 4838, pp. 956-963 (2003)., 956–963

Traub, W. A. 1986, Appl. Opt., 25, 528

—. 1990, Optical Society of America Journal, 7, 1779

Traub, W. A. 2000, in Principles of Long Baseline Stellar Interferometry, 31–+

Traub, W. A., Ahearn, A., Carleton, N. P., Berger, J. P., Brewer, M., Hofmann, K. H., Kern, P., Lacasse, M. G., Malbet, F., Millan-Gabet, R., Monnier, J. D., Ohnaka, K., Pedretti, E., Ragland, S., Schloerb, F. P., Souccar, K., & Weigelt, G. 2003, in Proc. SPIE, Interferometry for Optical Astronomy, Wesley A. Traub, editor, Vol. 4838, 45–52

Traub, W. A., Carleton, N. P., Bregman, J. D., Brewer, M. K., Lacasse, M. G., Maymounkov, P., Millan-Gabet, R., Monnier, J. D., Morel, S., Papaliolios, C. D., Pearlman, M. R., Porro, I. L., Schloerb, F. P., & Souccar, K. 2000, in Proc. SPIE, Interferometry in Optical Astronomy, Pierre J. Lena ; Andreas Quirrenbach ; Eds., Vol. 4006, 715–722

Traub, W. A. & Lacasse, M. G. 1988, in NOAO-ESO Conference on High-Resolution Imaging by Interferometry : Ground-Based Interferometry at Visible and Infrared Wavelengths, Garching bei München, Germany, Mar. 15-18, 1988. Edited by F. Merkle, ESO Conference and Workshop Oroceedings No. 29, p.947, 1988, 947–+

Traub, W. A., Lacasse, M. G., & Carleton, N. P. 1990, in Amplitude and intensity spatial interferometry ; Proceedings of the Meeting, Tucson, AZ, Feb. 14-16, 1990 (A91-30676 12-89). Bellingham, WA, Society of Photo-Optical Instrumentation Engineers, 1990, p. 145-152. Research supported by NASA and Smithsonian Institution., 145–152

Tubbs, R. N. 1998, Tracking and Characterising Atmospheric Phase Fluctuations at COAST, Part III undergraduate project report, May 1998, Cavendish Laboratory, Cambridge University

Tuthill, P. G., Monnier, J. D., & Danchi, W. C. 2001a, Nature, 409, 1012

—. 2001b, American Astronomical Society Meeting, 198, 0

Vakili, F. & Koechlin, L. 1989, in New technologies for astronomy ; Proceedings of the Meeting, Paris, France, Apr. 25, 26, 1989 (A90-37976 16-89). Bellingham, WA, Society of Photo-Optical Instrumentation Engineers, 1989, p. 109-116., 109–116

Vakili, F., Mourard, D., Bonneau, D., Morand, F., & Stee, P. 1997, A&A, 323, 183

van Belle, G. T., Ciardi, D. R., Thompson, R. R., Akeson, R. L., & Lada, E. A. 2001, ApJ, 559, 1155

Walkup, J. F. & Goodman, J. W. 1973, Optical Society of America Journal, 63, 399

Weigelt, G., Beckman, U., Berger, J. P., Bloecker, T., Brewer, M. K., Hofmann, K., Lacasse, M. G., Malanushenko, V., Millan-Gabet, R., Monnier, J. D., Ohnaka, K., Pedretti, E., Schertl, D., Schloerb, F. p., Scholz, M., Traub, W. A., & Yudin, B. 2003, in Proc. SPIE, Interferometry for Optical Astronomy, Wesley A. Traub, editor, Vol. 4838, 181–184

Weiner, J., Hale, D. D. S., & Townes, C. H. 2003, ApJ, 588, 1064

Wilson, E. 2003, In preparation

Wilson, R. W., Baldwin, J. E., Buscher, D. F., & Warner, P. J. 1992, MNRAS, 257, 369

Wilson, R. W., Dhillon, V. S., & Haniff, C. A. 1997, MNRAS, 291, 819+

Woillez, J. 2003, personal communication

Woolf, N. J. 1997, Bulletin of the American Astronomical Society, 29, 1311

Young, J. S., Baldwin, J. E., Boysen, R. C., Haniff, C. A., Lawson, P. R., Mackay, C. D., Pearson, D., Rogers, J., St.-Jacques, D., Warner, P. J., Wilson, D. M. A., & Wilson, R. W. 2000, MNRAS, 315, 635

Young, J. S., Baldwin, J. E., Boysen, R. C., Haniff, C. A., Pearson, D., Rogers, J., St-Jacques, D., Warner, P. J., & Wilson, D. M. A. 1999, in IAU Symp. 191 : Asymptotic Giant Branch Stars, 145–+